Neutron-induced damage simulations: Beyond defect production cross-section, displacement per atom and iron-based metrics

J.-Ch Sublet, I P Bondarenko, G Bonny, J L Conlin, M R Gilbert, L R Greenwood, P J Griffin, P Helgesson, Y Iwamoto, V A Khryachkov, et al.

EPJ Plus

EPJ.org
your physics journal

Eur. Phys. J. Plus (2019) **134**: 350 DOI 10.1140/epjp/i2019-12758-y

Neutron-induced damage simulations: Beyond defect production cross-section, displacement per atom and iron-based metrics

J.-Ch. Sublet et al.

Società Italiana di Fisica

Springer

Eur. Phys. J. Plus (2019) **134**: 350
DOI 10.1140/epjp/i2019-12758-y

THE EUROPEAN PHYSICAL JOURNAL PLUS

Review

Neutron-induced damage simulations: Beyond defect production cross-section, displacement per atom and iron-based metrics

J.-Ch. Sublet[1,a], I.P. Bondarenko[2], G. Bonny[3], J.L. Conlin[4], M.R. Gilbert[5], L.R. Greenwood[6], P.J. Griffin[7], P. Helgesson[8], Y. Iwamoto[9], V.A. Khryachkov[2], T.A. Khromyleva[2], A.Yu. Konobeyev[10], N. Lazarev[11], L. Luneville[12], F. Mota[13], C.J. Ortiz[13], D. Rochman[14], S.P. Simakov[10], D. Simeone[12], H. Sjostrand[8], D. Terentyev[3], and R. Vila[13]

[1] International Atomic Energy Agency, Wagramerstrasse 5, 1400 Vienna, Austria
[2] State Atomic Energy Corporation ROSATOM, Institute for Physics and Power Engineering, Obninsk, Russia
[3] Nuclear Materials Science Institute, SCK-CEN, Boeretang 200, B-2400 Mol, Belgium
[4] Los Alamos National Laboratory, Los Alamos, NM, USA
[5] United Kingdom Atomic Energy Authority, Culham Science Centre, Abingdon OX14 3DB, UK
[6] Pacific Northwest National Laboratory, Richland, WA, USA
[7] Sandia National Laboratories, Radiation and Electrical Science Center, Albuquerque, NM, USA
[8] Uppsala University, Department of Physics and Astronomy, 751 20 Uppsala, Sweden
[9] Japan Atomic Energy Agency, Nuclear Science and Engineering Center, Tokai, Ibaraki 319-1195, Japan
[10] Institute for Neutron Physics and Reactor Technology, Karlsruhe Institute of Technology, 76021 Karlsruhe, Germany
[11] NSC Kharkiv Institute of Physics and Technology, 61108 Kharkiv, Ukraine
[12] CEA, Université Paris-Saclay, F-91191, Gif-sur-Yvette, France
[13] Laboratorio Nacional de Fusión por Confinamiento Magnético CIEMAT, 28040 Madrid, Spain
[14] Paul Scherrer Institut (PSI), 5232 Villigen, Switzerland

Received: 30 January 2019 / Revised: 6 May 2019
Published online: 23 July 2019

Abstract. Nuclear interactions can be the source of atomic displacement and post-short-term cascade annealing defects in irradiated structural materials. Such quantities are derived from, or can be correlated to, nuclear kinematic simulations of primary atomic energy distributions spectra and the quantification of the numbers of secondary defects produced per primary as a function of the available recoils, residual and emitted, energies. Recoils kinematics of neutral, residual, charged and multi-particle emissions are now more rigorously treated based on modern, complete and enhanced nuclear data parsed in state of the art processing tools. Defect production metrics are the starting point in this complex problem of correlating and simulating the behaviour of materials under irradiation, as direct measurements are extremely improbable. The multi-scale dimensions (nuclear-atomic-molecular-material) of the simulation process is tackled from the Fermi gradation to provide the atomic- and meso-scale dimensions with better metrics relying upon a deeper understanding and modelling capabilities of the nuclear level. Detailed, segregated primary knock-on-atom metrics are now available as the starting point of further simulation processes of isolated and clustered defects in material lattices. This allows more materials, incident energy ranges and particles, and irradiations conditions to be explored, with sufficient data to adequately cover both standard applications and novel ones, such as advanced-fission, accelerators, nuclear medicine, space and fusion. This paper reviews the theory, describes the latest methodologies and metrics, and provides recommendations for standard and novel approaches.

1 Introduction

An IAEA Coordinated Research Project was aimed at reviewing the theory, methodology and data-streams behind the ubiquitous NRT-dpa [1] material damage-dose-defect cross-section–based metric, including its short-comings. Furthermore, the project aimed to evaluate and explore alternative, modern and enhanced metrics that (theoretically) could be better able to highlight the complex problem of correlating, simulating and predicting the behaviour and evolution of materials properties when under particle irradiation.

[a] e-mail: j.c.sublet@iaea.org (corresponding author)

Outcomes from the CRP, discussed below, include revised, improved, extended numerical databases and metrics useful for the simulation of particle-induced defect production (both isolated, point defects, and defect clusters) as a function of the particle energy and spectra —and not just for the well-trodden thermal-neutron energy range and standard materials of the fission industry. The actual modelling has focussed on methods of determining defect production cross-sections (DPCS) from primary knock-on atoms (PKA) simulations and recoil energy-dependent defect production functions [2] derived from experiments. However, these rarely explore beyond core elements, such as iron and silicon, in low-energy irradiation fields. Emphasis was also put on uncertainty and sensitivity analyses, as well as on nuclear-atomic-molecular–material scaling effects and their even more complex possible interpretations.

In this paper, examples of DPCS simulations are presented, applicable to a large number of elements, irradiation fields, conditions and defect types in the neutron energy range from thermal to tenths of MeV. These simulations include improved treatment of non-elastic multi-particles events while elastic and inelastic scattering events are treated based on much refined cross-sections angular distribution and emitted spectra data. Alternatives and limits to the secular NRT-dpa approaches, including prompt, time-dependent and decay-induced defects, are also discussed.

2 Theory of damage energy

Effects of radiation on the properties of solids are of significant interest in scientific and technological contexts ranging from astrophysics to nuclear industry [3]. Large-scale effects associated with drastic changes of material properties were observed after the development of nuclear fission reactors in the 1940s. Wigner anticipated that intense neutron flux produced in the core of fission reactors could alter the properties of the graphite moderator and the uranium fuel. His estimation of what might happen led to the term "Wigner disease" for radiation damage [4]. The later development of nuclear fission and simulation of fusion devices have made the structural effects of radiation of great technological importance.

The first step in producing radiation effects is the generation of primary recoil atoms (also known as Primary Knock-on Atoms PKAs) by the scattering of incident radiation, nuclear reaction or radioactive decay. Such events take place very rapidly, typically in 1 fs (10^{-15} s). The PKA dissipates its initial kinetic energy in two distinct ways:

- Some energy is lost by exciting the electrons of the medium or those of the PKA itself; such excitation leads to the ionization of some of the particles.
- PKA undergoes elastic collisions with other atoms of the irradiated material. These elastic collisions mean that the total kinetic energy of the atoms involved in the collision is nearly conserved. In such a description, the small momentum carried by electrons can be ignored in the collision dynamics.

This description follows the analyses of Bohr and Lindhard [5,6]. Atoms with which the PKA collides can receive enough kinetic energy to be displaced from their own lattice sites and thence to make similar collisions of their own. A branching tree-like structure exhibiting a fractal like behavior [7,8] is produced which dissipates the PKA energy over a time scale of about 100 fs. This tree-like structure of collisions, called a displacement cascade, produces a large number of atoms moving with near-thermal velocities, accompanied with some degree of electron excitation. The latter only produces heat in metals, but in semi conductors and insulators can produce significant long-term stable defects [3]. The nascent damage produced at the end of a displacement cascade generated by PKAs evolves through complex many-body processes and rearrange rapidly into more stable defects, such as point defects and small clusters, over a space scale of a few nanometers. Complex many body processes can also lead to a branching (splitting) of displacement cascades created by very-high energy PKAs (above few hundreds of keV) and thence to sub-cascade formation [7,9]. After this process, the remaining primary defects combine and agglomerate into clusters or generate micro-structural changes over a large space scale (few microns) and over a diffusion time scale of a few 10^{-6} seconds, leading to patterns of the microstructure unexpected from the thermal equilibrium [10]. These patterns created in the material depend on the initial amount of defects and the temperature, leading to drastic changes in material properties.

2.1 Primary metrics and their phenomenology

The theoretical methods used to study defects production are of several types. Once the PKA spectra associated with neutron-isotopes are properly calculated from nuclear data [11], the number and the spatial distribution of primary damage induced by a PKA of given kinetic energy can be evaluated. This evaluation results from a transport theory [12] related with the time-rate of change of the density of particles in an element of space and velocity (phase space of the problem). Such an approach requires the solution of non-linear integro-differential equations [13]. Within the framework of the Binary Collision Approximation (BCA), such equations can be solved analytically as in the Kinchin Pease damage production model [14], numerically as is done in the DART code [15,16] or via Monte Carlo simulations as it is the case for the SRIM code [17]. Similar calculations within the BCA can be performed, for instance with the

MARLOWE code [18], to take into account channeling induced by the crystalline nature of the target. Comparisons [19] point out that these approaches give similar amount of primary damage at least for polycrystalline samples. The main interest of these approaches, based on the BCA, lies on the fact that primary damage resulting from elastic scattering can be computed from the knowledge of universal repulsive inter-atomic pair potentials derived from the Thomas-Fermi model [17]. From the introduction of the notion of a recombination radius, *i.e.* the minimal distance beyond which two interstitials do not recombine, it is possible to define the notion of the displacement energy threshold E_d as a criterion at which to stop the BCA simulation. Each interstitial with a kinetic energy above E_d varying from few tens of eV to one hundred eV in some ionic insulators [3] leads to the creation of a Frenkel pair, *i.e.* the formation of a pair of stable vacancy and interstitial. As all calculations within the BCA deal with the kinetic energy of atoms, the recombination volume is only a topological criterion independent of the temperature. From this analysis, it becomes possible to compute the number of displacement per atoms (dpa), *i.e.* the number of Frenkel pairs produced by a PKA at the end of a displacement cascade.

Atomistic models based on Molecular Dynamical (MD) simulations can also be used to simulate the nature, the number and the spatial distribution of primary defects produced in a displacement cascade. The difference between MD simulations and BCA partly lies in the fact that the potential energy of the crystal is taken into account in MD simulations. Atoms in equilibrium and at interstitial positions are subjected to forces from all of the other atoms of the crystal in these simulations. Frenkel pairs produced during the ballistic collision phase evolve to create dislocation loops, voids, and more complex defects like stacking faults in metals —a process determined by the relative potential energy of different structures in the crystal. On the other hand, vibration modes, associated with the potential energy of the crystal existing for non-zero temperature, modify the recombination volume. The main limitations of the MD simulation are the difficulty in determining realistic potential energy for crystals and the computational intensive cost which frequently provides only limited statistics and often forbids adequate sampling of the PKA spectrum. As MD simulations are based on classical mechanics, simulation of primary defects under irradiation must only be performed for temperature above the Debye temperature of the target. The last, but not the least, consideration is that the thermodynamic is recovered from MD simulations of conservative systems (the total energy resulting from the sum of the potential and kinetic energies of atoms of the crystal fixed) but no theorem ensures that the notion of temperature or pressure can be derived for non-conservative system, in which energy is injected via the kinetic energy of the PKA.

2.2 Recommended calculation and simulation routes

Based on this analysis, the effect of radiation damage on materials can be defined by the notion of primary damage only resulting from dpa calculations. Under such an approach, the impact of the neutron flux and the isotopic composition for a given target can be estimated once the energy threshold displacement is given. Based on an approximation of the LSS theory [13] developed within the BCA framework, it is possible to define a damage efficiency function selecting only the part of the PKA kinetic energy responsible for the elastic collision. Following the same direction, Norgett Robinson and Torrens (NRT) [1] defined an analytical expression to compute the number of dpa produced at the end of a displacement cascade for pure elements (NRT-dpa). Such a formulation can be extended to multi-component materials like ceramics or alloys. The analytical expression of the number of dpa makes this model very useful to understanding the impact of transmutation and PKA effects on the primary damage production. Different codes (SPECOMP, DART, or SPECTRA-PKA) are now available to compute the primary damage production for polyatomic targets.

The translation from quantities of primary damage to total amounts of extended defect types can be performed introducing an efficiency factor $\xi(E_{PKA})$ where E_{PKA} is the energy of the PKA atoms and this factor can be derived from MD simulations.

2.3 NRT-dpa theory

A macroscopic integral neutron damage metric, ${}^{fac}D_{type}$ can be expressed as the convolution of the neutron source term, characteristic of a facility *fac*, over a given *type* of an energy-dependent microscopic damage response function, $\Re_{type}(E)$, and the incident neutron spectrum, $\phi^{fac}(E)$. The macroscopic damage metric, ${}^{fac}D_{type}$, is given by the expression seen in eq. (1), where ${}^{type}\aleph$ is a response unit conversion factor that varies with the selected *type* of the microscopic damage response, ${}^{fac}\Phi$ is the facility-specific neutron fluence, and $\phi^{fac}(E)$ is the facility-specific unit-normalized energy-dependent neutron spectrum. This notation for the expression of a damage metric applies to a wide range of radiation-induced damage modes ranging from material heating, to the amount of trapped bulk charge due to ionization, to the density of various types of displacement-induced lattice defects,

$$ {}^{fac}D_{type} = {}^{type}\aleph \cdot {}^{fac}\Phi \int_0^\infty \phi^{fac}(E) \cdot \Re_{type}(E) \cdot \mathrm{d}E. \tag{1}$$

The unit conversion factor, ${}^{type}\aleph$, will vary with the units associated with the desired damage metric and the form of the selected microscopic response function. This term can be very simple, as in the case where the damage metric is a material dpa, where it captures the unit conversion due to the cross-section being given in units of barns while the neutron fluence is given relative to area units of cm^{-2}, or it can be more complex, as in the case where the damage metric is deposited dose expressed in units of rad, where the unit conversion factor involves the molecular weight of the material and Avogadro's number.

There are many different material damage modes, and each damage mode may be described by a different form of the microscopic response function. The purpose of this paper is not only to examine the sufficiency of the traditional form of the iron-based damage metric, the NRT-based dpa metric, but to look "beyond" the traditionally used damage model and to look at the advantages and disadvantages of using improved damage response functions that have been reported in the literature —damage models that, informed by more detailed modeling based on molecular dynamics calculations, have the potential to exhibit better correlations between damage metrics calculated from model-based energy-dependent response functions and actual measurements of properties believed to be proportional to various material damage metrics. To support this objective, we start by providing a generic formulation of the microscopic response function. A formulation or notation is adopted that can not only capture the current state-of-the-art NRT damage models, but one that can also shed light on the underlying physics of the damage processes and has the potential to also accommodate other, more advanced, damage models —damage models that might be able to show the desired improved correlation with damage measurements. To this end, the material damage energy-dependent response function is formulated in a general expression of the form,

$$\Re_{type}(E) = \sum_{i,j_i} \sigma_{i,j_i}(E) \int_0^{\infty} \mathrm{d}T_{R,j_i} \int_{-1}^{1} \mathrm{d}\mu f(E,\mu,T_{R,j_i}) \cdot {}^{A}\Lambda(E_d, {}^{ion}T_R) \cdot {}^{B}\zeta(E_d, T_{R,j_i}, {}^{D}T_{dam}) \cdot {}^{C}\xi(T_{R,j_i}). \quad (2)$$

In this expression:

- The summation is over all reaction channels i and all particles, j_i, emitted in that reaction channel.
- the integral is over the recoil particle energy and the recoil emission angle.
- E is the energy for the incident neutron.
- E_d is the angle-averaged displacement threshold energy.
- σ_{i,j_i} is the microscopic cross-section for producing particle j_i, through reaction i.
- T_{R,j_i} is the associated recoil particle/ion energy, identical to the E_{PKA} notation used in the previous section but, here, written with the explicit identification of the reaction channel responsible for the production of the recoil atom, i, and an identifier for the type of recoil particle, j_i.
- $f(E,\mu,T_{R,j_i})$ is the energy/angle distribution for emitted charged recoil particles with an energy T_{R,j_i} at an angle characterized by $\mu = \cos(\theta)$ that result from the j_i particle in the i-th reaction channel and are induced by the incident neutron energy with energy E.
- ${}^{A}\Lambda(E_d, {}^{ion}T_R)$ is a threshold treatment function of *type A*. This term can have a complex shape and contains a functional dependence that corresponds to the effective damage/defect generation component that is addressed in the following term. Example treatments include an A value of KP that refers to the sharp threshold Kinchin-Pease (KP) model; a value of NRT that refers to the NRT modification to the KP model [20]; a value of NS that refers to the Neufeld-Snyder model; and a value of SN that refers to the Snyder-Neufeld model.
- ${}^{B}\zeta(E_d, T_{R,j_i}, {}^{D}T_{dam})$ is the effective damage/defect generation component of *type B*. Example damage components include a B value of *dam* that refers to displacement damage energy; a value of *disp* that refers to displacement kerma; a value of *ion* that refers to ionizing kerma; and a value of *dpa* refers to displacements per atom. Since this effective damage/defect component can be used as an argument in other expressions, we also adopt a shorthand notation for this ion-specific energy component using the expression ${}^{ion}T_R$.
- ${}^{C}\xi(T_{R,j_i})$ is a residual damage/defect efficiency survival term of *type C*. Example efficiency representations include a C value of *unity* that can be used in conjunction with the traditional NRT methodology when a modification is not required; a value of *Bac* refers to the molecular dynamics-informed Bacon model [21,22] which uses a power law to capture the Frenkel pair production term but implements it as a correction term to be applied to the traditional NRT-based Frenkel pair term; a value of *vac_cls* that refers to the fraction of vacancies that appear in a cluster; and a value of *inst_cls* that refers to the fraction of interstitials that appear in clusters. The damage efficiency is typically presented as a function of the recoil ion energy and the recoil energy-dependent shape can depend upon the physical mechanisms that underlay the damage mode being addressed. This efficiency term provides a method of capturing advanced damage models such as those that capture the effects of electron-phonon coupling on the defect production in a thermal spike region that can result from some damage cascades [23] and which, if neglected, may lead to an overestimation of cascade damage in some metals.

– ${}^{D}T_{dam}(T_{R,j_i})$ is the *type D* fractional energy partition function for the emitted ion j_i in the i-th open channel with energy T_{R,j_i} and typically takes on values within the range $\langle 0, 1\rangle$. This partition function can be used to specify the displacement component or the ionizing component of the recoil ion energy. Examples of displacement forms of this energy partition functions include a D value of LSS that refers to the LSS model, which uses the Thomas-Fermi screening function over the Coulomb potential to model the elastic interactions and a non-local free uniform electron gas model for the inelastic electronic scattering; a value of *Rob* that refers to the Robinson fit to the LSS potential; a value of ZBL that refers to use of the Ziegler, Biersack, and Littmark potentials [17]; and a value of *Ack* that refers to the Akkerman fit to the damage partition that has been specified for some materials [24].
– The $\{type\}$ qualifier applies to the general response function and captures the combination of the $\{A, B, C, D\}$ characterizations that apply to the specific formulation of the *type* descriptor for the damage metric under consideration.

Most of the material-specific primary damage metrics used by the radiation effects community can be formulated into an expression in the form shown in eqs. (1) and (2). No new physics is contained in eq. (2). This formulation only provides a notation that can be used to compare a wide range of the damage models that have been reported in the literature. It also provides a grouping of physics-related terms in a way that supports an investigation of the uncertainty associated with the modeling of the microscopic response function and its energy-dependent correlation, as is discussed in sect. 4.2 of this paper. The complexity of the $\{type\}$ qualifier of the response function is required in order to provide a general expression that can be tailored to the range of damage models that can be found in the literature.

As an example of the formulation of this notation for a primary damage metric, consider its formulation for the case where it captures the most commonly used displacement damage metric, the traditional Norgett-Robinson-Torrens (NRT)-based damage energy [1]. This is a community-accepted fundamental displacement damage metric, it provides the foundation for the definition of the commonly quoted 1 MeV-equivalent damage metric in various materials, and it forms the foundation for the definition of the dpa metric. The NRT-based damage energy is defined in a manner similar to that for the displacement kerma, but it also has a special treatment for the effective damage component in the region where its value is near the displacement threshold energy of a crystalline material. When an NRT-threshold treatment is applied to the Robinson-based displacement energy, $\Re_{type}(E)$ can be defined, in the form of eq. (2), using the qualifiers $\{type = NRT\_dam\_eng\} = \{A = NRT\_DE,\ B = dam,\ C = unity,\ D = Rob\}$. In this formulation the terms in the expression take the form

$$ {}^{NRT\_DE}\Lambda(E_d, {}^{ion}T_R) = \begin{cases} 0.0, & 0 \le {}^{ion}T_R < E_d \\ \dfrac{2E_d}{\beta\, {}^{ion}T_R}, & E_d \le {}^{ion}T_R < (2E_d/\beta) \\ 1.0, & (2E_d/\beta) \le {}^{ion}T_R < \infty, \end{cases} \tag{3} $$

$$ {}^{dam}\zeta(E_d, T_{R,j_i}, {}^{Rob}T_{dam}) = {}^{Rob}T_{dam}(T_{R,j_i}) \cdot T_{R,j_i} = \frac{T_{R,j_i}}{[1 + F_L \cdot g(\frac{T_{R,j_i}}{E_L})]}, \tag{4} $$

$$ {}^{unity}\xi(T_{R,j_i}) = 1, \tag{5} $$

where

– $\{type = NRT\_dam\_eng\} = \{A = NRT, B = dam, C = unity, D = Rob\}$ has the following characteristics:
$A = NRT$ refers to the use of the Kinchin-Pease threshold treatment as modified in the NRT formulation;
$B = dam$ refers to the use of the damage energy as the relevant damage metric;
$C = unity$ refers to use of a unit damage efficiency, an efficiency that does not depend upon the recoil atom energy and corresponds to no correction being applied to the baseline NRT model; and
$D = Rob$ refers to the use of the Robinson functional fit to the LSS displacement damage partition function.
– β is an atomic scattering correction and is generally taken to be 0.8.
– The F_L, E_L, and $g(E)$ terms are defined within the formalism of the Robinson fit to the LSS partition function [20], and addressed in sect. 3.3.1 of this paper.

This expression of the NRT-based damage energy is the foundation for one of the most commonly used primary damage metrics, the displacements per atom, or dpa. Dpa is a macroscopic metric, as expressed in the ${}^{fac}D_{type}$ term seen in eq. (1), and it corresponds to the number of times that an atom in a lattice is displaced for a given incident particle fluence. In the formulation of this damage metric, a reference damage energy, α, is defined, *i.e.* the energy required to form one Frenkel pair in the material with a displacement threshold energy of E_d. The NRT-based reference energy is given by

$$ {}^{NRT}_{E_d}\alpha_\beta = \frac{(2E_d)}{\beta}. \tag{6} $$

The number of primary Frenkel pairs in a cascade is then defined by dividing the damage energy, given in eq. (3), by this reference damage energy. The dpa metric is formed by taking this number of Fenkel pairs in a damage cascade, multiplying by the microscopic cross-section in units of barns per atom, and applying a conversion factor to account for the difference in area units used in the cross-section expression (barns) and in the neutron fluence term (typically neutrons per cm^2 or m^2). When the Robinson energy partition function is used with the NRT threshold treatment, the dpa damage metric is designated as $\{type = NRT\_dpa\}$, and the type-qualifiers are denoted as $\{A = NRT\_FP, B = dam, C = unity, D = Rob\}$. In this expression for the primary Frenkel pair metric, the effective damage/defect generation component is the same as eq. (4), the residual damage/defect efficiency survival term is the same as eq. (5), and the threshold treatment function is given as

$$ {}^{NRT\_FP}\Lambda(E_d, {}^{ion}T_R) = \begin{cases} 0.0, & 0 \leq {}^{ion}T_R < E_d, \\ \dfrac{1.0}{{}^{ion}T_R}, & E_d \leq {}^{ion}T_R < (2E_d/\beta), \\ \dfrac{\beta}{2E_d}, & (2E_d/\beta) \leq {}^{ion}T_R < \infty. \end{cases} \tag{7} $$

In this formulation, the product of the damage production term and the threshold treatment term reduce to the commonly seen NRT Frenkel pair generation expression

$$ {}^{NRT}\nu_d(E_d, {}^{ion}T_R) = {}^{NRT\_FP}\Lambda(E_d, {}^{ion}T_R) \cdot {}^{dam}\zeta(E_d, T_{R,j_i}, {}^{Rob}T_{dam}) $$

$$ {}^{NRT\_FP}\Lambda(E_d, {}^{ion}T_R) \cdot {}^{ion}T_R = \begin{cases} 0.0, & 0 \leq {}^{ion}T_R < E_d \\ 1.0, & E_d \leq {}^{ion}T_R < \dfrac{2E_d}{\beta} \\ \dfrac{\beta\, {}^{ion}T_R}{2E_d}, & \dfrac{2E_d}{\beta} \leq {}^{ion}T_R < \infty. \end{cases} \tag{8} $$

As the ability to do high-fidelity molecular dynamics calculations has matured and there is a better understanding of the dependence of the number and type of defects upon the energy of the recoil particle, and not just on the magnitude of the damage energy component, new damage metrics are being proposed and correlated with specific damage processes, *e.g.*, the vacancy fraction within a cluster and the interstitial fraction within a cluster that are addressed in sect. 5.1 of this paper.

The damage production, threshold treatment, and damage efficiency terms that are broken out in eq. (2) can depend upon the value of the displacement threshold energy. It is important to note that there is not a single threshold displacement energy, but that each crystal direction has its own characteristic value due to the crystal anisotropy. Thus, it is important that this user-defined quantity, whether derived through calculation or experimental approaches, be treated in a consistent manner in each of the various terms that appear in the integral damage metric depicted in eq. (1).

3 Review of recent theory and advances in nuclear interactions

In this section we consider some of the recent and specific examples of new approaches and developments presented within the collaborative project.

3.1 PKA spectra: Transmutation effects

Neutrons produced in nuclear reactors are not only able to produce elastic collisions with stable nuclei forming the target but they are also involved in many inelastic collisions leading to the formation of metastable nuclei. These metastable nuclei decay emitting light particles such as electrons and neutrons but also recoils with important kinetic energies. The existence of such recoils can modify the PKA spectra, and they are furthermore the only creators of damage after irradiation (*i.e.* damage will continue to be created in a structural reactor steel even after the reactor has shutdown). An example of such inelastic reaction is given by the decay of ^{238}U which leads to the emission of an α particle with a kinetic energy of 4.2 MeV and a ^{234}Th recoil with a kinetic energy of 72 keV. The α particle expends most of its kinetic energy in electronic excitation over a large path whereas the major part of the kinetic energy of the ^{234}Th (around 60 keV) induces elastic collisions along a few hundreds of nanometers. From this example, it clearly appears that most damage is mainly produced by the recoil. Emission of electrons in a β-decay is always associated with a neutrino emission. As a result, β particles are emitted with a broad range of kinetic energies. However, the energy transmitted to recoils can be given by

$$ T = \frac{E_\beta[E_\beta + 2mc^2]}{2Mc^2}, \tag{9} $$

where E_β is the maximum kinetic energy of the β spectrum, M the mass of the recoil and $mc^2 = 0.511\,\mathrm{MeV}$ in the center-of-mass frame. The ^{234}Th decays leading to the emission of a β spectrum ($E_\beta = 0.191\,\mathrm{MeV}$). The maximum energy T of the ^{234}Pa daughter recoil then reduces to 0.53 keV. This recoil energy is very low and produces little damage. The slowing down of the β particle leads to the production of few dpa (the dpa cross-section is roughly equal to few barns [16]) to the recoil spectra (few tens of barns). From this illustration, it appears that β decay can be neglected in the damage production under irradiation. The kinetic energy of a recoil in a γ-decay is equal to

$$T = \frac{E_\gamma^2}{2Mc^2}\,. \tag{10}$$

in the center-of-mass frame, where M is the mass of the recoil and E_γ the kinetic energy of the photon. In radioactive decay events, γ-ray energies rarely exceed 2 MeV and mostly are below 1 MeV. Application of the formula clearly points out that only light recoils ($M < 10$) can be produced with a kinetic energy of 50 eV for 1 MeV γ-rays.

As an example highlighting drastic modifications of PKA spectra induced by transmutation effects, the impact of transmutation in Ni-based materials for different nuclear reactors is discussed in detail pointing out the role of the neutron spectrum, the decay and the recoils on the computation of the PKA spectrum. Five isotopes are present in the natural nickel: ^{58}Ni (68.07%); ^{60}Ni (26.22%); ^{61}(1.13%); ^{62}Ni (3.63%) and ^{64}(0.92%). The most abundant isotope ^{58}Ni produces a long-lived radioactive (^{59}Ni) according to the capture reaction

$$^{58}\mathrm{Ni} + n \rightarrow {}^{59}\mathrm{Ni}. \tag{11}$$

This ^{58}Ni capture cross-section is significant only for thermal neutrons. Moreover, the long-lived residual ^{59}Ni isotope can also transmute leading to the formation of different residuals, ^{56}Fe, ^{59}Co and ^{60}Ni according to the following reactions [25,26]:

$$^{59}\mathrm{Ni} + n \rightarrow {}^{56}\mathrm{Fe} + \alpha, \tag{12}$$

$$^{59}\mathrm{Ni} + n \rightarrow {}^{59}\mathrm{Co} + H, \tag{13}$$

$$^{59}\mathrm{Ni} + n \rightarrow {}^{60}\mathrm{Ni} + \gamma. \tag{14}$$

Computing the atomic fractions of the different isotopes is thus possible using the cross-sections associated with these reactions. In the following, the cross-sections were extracted from the JENDL-4.0 evaluation. The nickel isotopes as well as ^{59}Co and ^{56}Fe atomic fractions are plotted *versus* the fluence for thermal neutrons in fig. 1. The evolution of ^{59}Ni is highly non-linear with the fluence. ^{59}Ni atomic fraction in pure Ni is negligible for non-irradiated Ni, reaches a maximum of 3% for a fluence of about $2 \times 10^{22}\,\mathrm{cm}^{-2}$ and vanishes at high fluence.

Figure 2 displays the comparison between elastic and the inelastic cross-sections associated with eq. (12), eq. (13), eq. (14) *versus* the impinging neutron kinetic energy for ^{59}Ni. Moreover, the (n,α) reaction releases 4.8 MeV α particles and 340 keV Fe recoils. Also, the (n,p) reaction generates 1.85 MeV protons and 31 keV Co recoils for thermal neutrons. For ^{59}Ni, inelastic cross-sections are of the same order of magnitude as the elastic one and cannot be neglected. This figure highlights the highly non-linear dependence of the different neutron-nucleus cross-sections as a function of the neutron kinetic energy. This simple example illustrates the need of accurate non-elastic cross-sections which are a function of the kinetic energy of neutrons.

To compute PKA and displacement cross-sections, the angular distribution of emitted particles $T(\mu, E)$ associated with inelastic nuclear reactions need to be weighted by the angular distribution probability of emitted particles extracted from cross-section data libraries. Figure 3 displays the PKA spectra associated with elastic and inelastic cross-sections for neutron ^{59}Ni interactions. As expected, the elastic cross-section is the dominant process at low energy (red line). The recoil of Fe and Co atoms induced by (n,α) and (n,p) reactions are responsible for two important narrow peaks at 0.1 MeV and 1 MeV. This example clearly shows the importance of non-elastic processes in primary damage production.

Figure 3 displays the partial displacement cross-sections, computed within the BCA framework, due to the different reactions occurring in ^{59}Ni. The important contribution of the (n,α) and the (n,p) reactions to the total displacement cross-section show the impact of Fe and Co recoil atoms on the primary damage. This figure thus highlights the role of recoil atoms in the primary damage production.

The dpa production rates can thus be obtained when weighting the displacement cross-sections by the neutron flux with the DART code [27]. These dpa rates have been calculated in different nuclear reactors for two materials containing different isotopes of nickel: $\mathrm{Fe}_{0.9}{}^{58}\mathrm{Ni}_{0.1}$ and $\mathrm{Fe}_{0.9}{}^{59}\mathrm{Ni}_{0.1}$. To show the impact of the transmutation of ^{58}Ni to ^{59}Ni on the dpa rate, the ratio between these two dpa rates $R = \frac{dpa(\mathrm{Fe}_{0.9}{}^{59}\mathrm{Ni}_{0.1})}{dpa(\mathrm{Fe}_{0.9}{}^{58}\mathrm{Ni}_{0.1})}$ have been plotted in fig. 4. The increase of dpa rate due to the transmutation of ^{58}Ni to ^{59}Ni is important in the HFIR nuclear reactor due to the high thermal neutron flux.

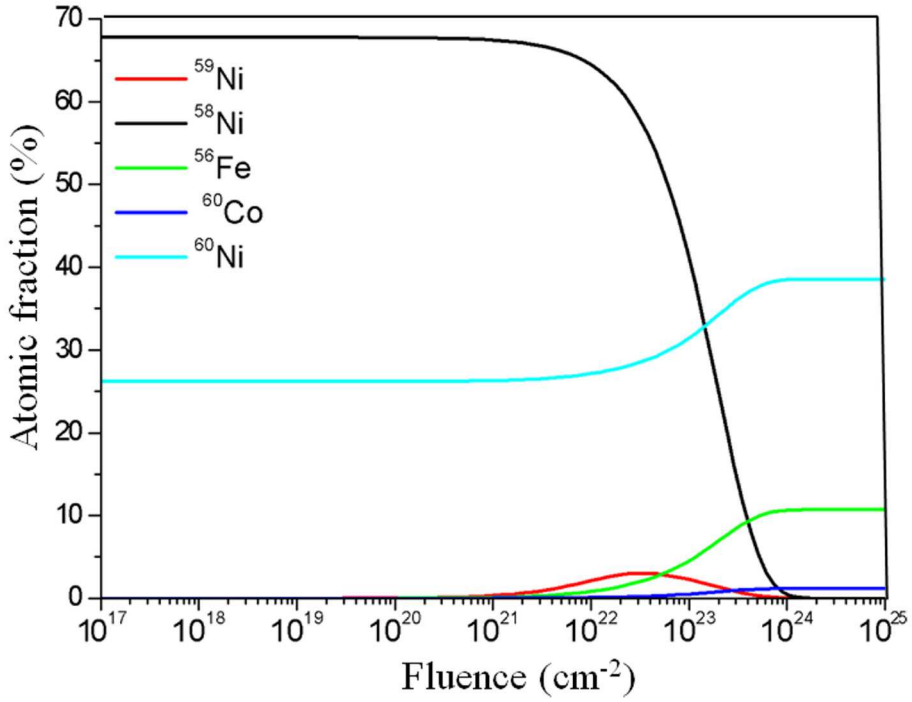

Fig. 1. Atomic fraction of ^{58}Ni (black), ^{59}Ni (red), ^{56}Fe (green), ^{59}Co (blue), and ^{60}Ni (cyan) *versus* the fluence F, were evaluated for thermal neutrons. As the abundance of ^{59}Ni is low for small and high fluences, it reaches a maximum at $2 \times 10^{22}\,\mathrm{cm}^{-2}$, corresponding to the middle life of a nuclear cycle.

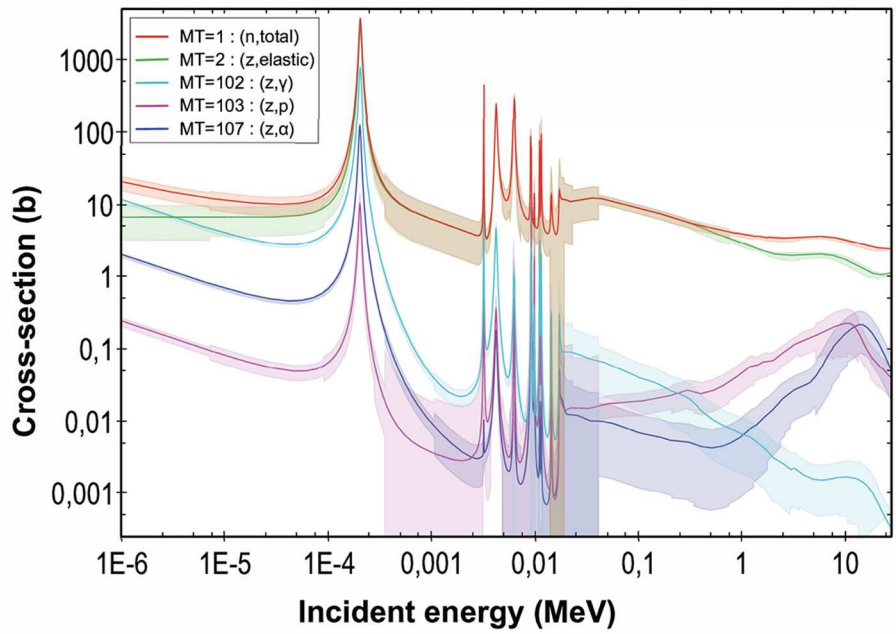

Fig. 2. Cross-sections including uncertainty bands *versus* neutron incident energy for ^{59}Ni. Cross-sections taken from JEFF 3.3. Figure created with JANIS tool.

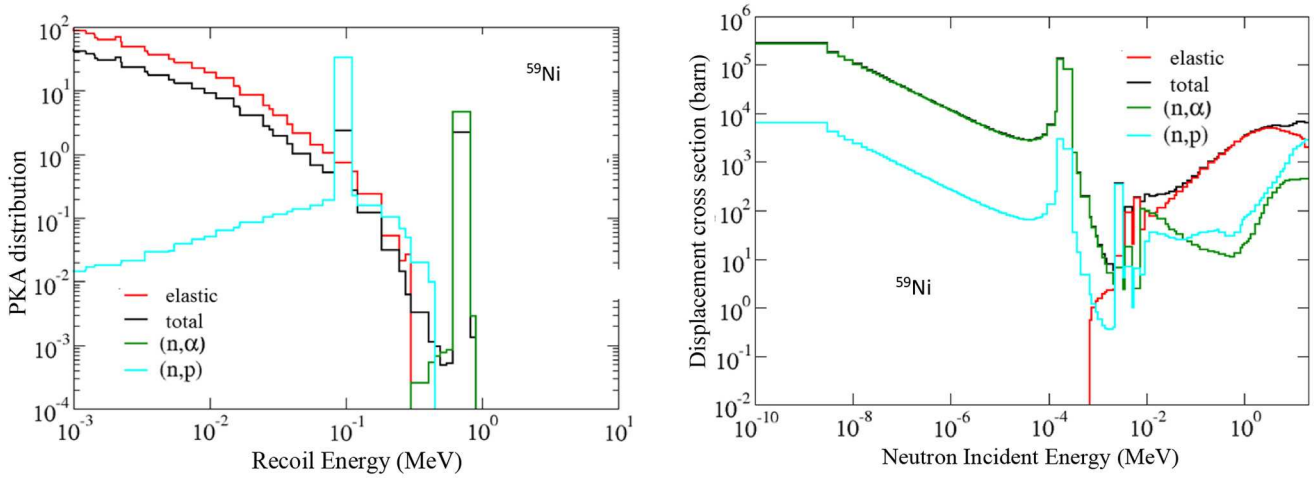

Fig. 3. Left: comparison of PKA spectra as a function of the recoil energy T for elastic and non-elastic nuclear interactions occurring in ^{59}Ni (green line: (n,α); blue line: (n,p); red line: elastic; black line: all processes). All these calculations were performed for the HFIR reactor with the JENDL-4.0 library on pure ^{59}Ni isotope. Right: displacement cross-sections (obtained with the DART code [11]) as a function of the kinetic energy of the incident neutron for all different reactions existing in pure ^{59}Ni isotope (green line: (n,α); blue line: (n,p); red line: elastic; black line: all processes). Data taken from [27].

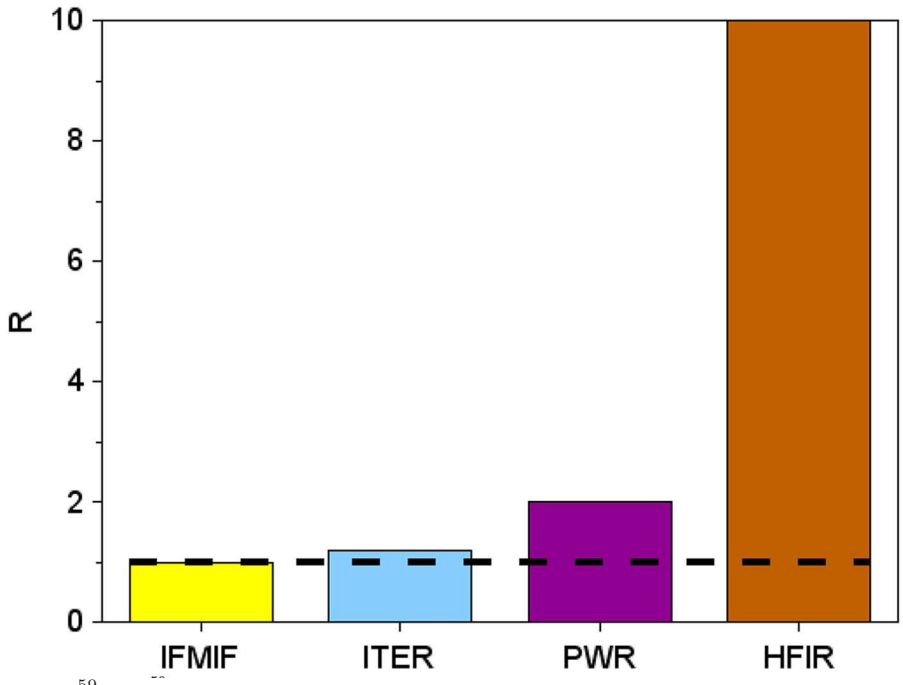

Fig. 4. Ratio $R = \frac{dpa(\mathrm{Fe_{0.9}{}^{59}Ni_{0.1}})}{dpa(\mathrm{Fe_{0.9}{}^{58}Ni_{0.1}})}$ of dpa production rates calculated for different reactors. The dotted line corresponds to a value of one for the ratio, when there is no increase of the dpa rate due to the transmutation of ^{58}Ni to ^{59}Ni.

3.2 The importance of transmutation and gas production reactions on radiation damage

Primary radiation damage in most materials irradiated in fission reactors is mainly due to recoils produced by elastic and inelastic scattering, which do not cause any transmutation. Transmutation from nuclear reactions typically occurs at a low rate in fission reactors due to the higher neutron energy thresholds and lower neutron flux for reactions, such as (n,p), (n,α) and $(n,2n)$. Most transmutation in fission reactors thus comes from thermal neutron capture (n,γ) reactions and high transmutation rates can be produced when thermal neutron cross-sections are large. Thermal neutron charged particle reactions, such as the well-known ^{59}Ni(n,α) and (n,p) reactions, can also produce significant transmutation and additional radiation damage; however, only after an incubation period required to produce significant levels of ^{59}Ni at higher neutron fluence. Transmutation also significantly increases with neutron energy since 14 MeV neutron sources, fusion reactors, and accelerator-based neutron sources produce higher energy neutron fluxes above the threshold for charged particle reactions.

Table 1. Principal thermal neutron gas production reactions of interest for selected elements.

Reaction	Sig. (b)	He(appm)/dpa	Materials
^{59}Ni(n, α)^{56}Fe	14	548	SS, Inconel
^{10}B(n, α)^{7}Li	3840	4953	Impurity in steels
^{6}Li(n, α)^{3}H	941	11682	Fusion TBR
^{55}Fe(n, α)^{52}Cr	0.027	731	Steels
^{65}Zn(n, α)^{62}Ni	2	493	Copper

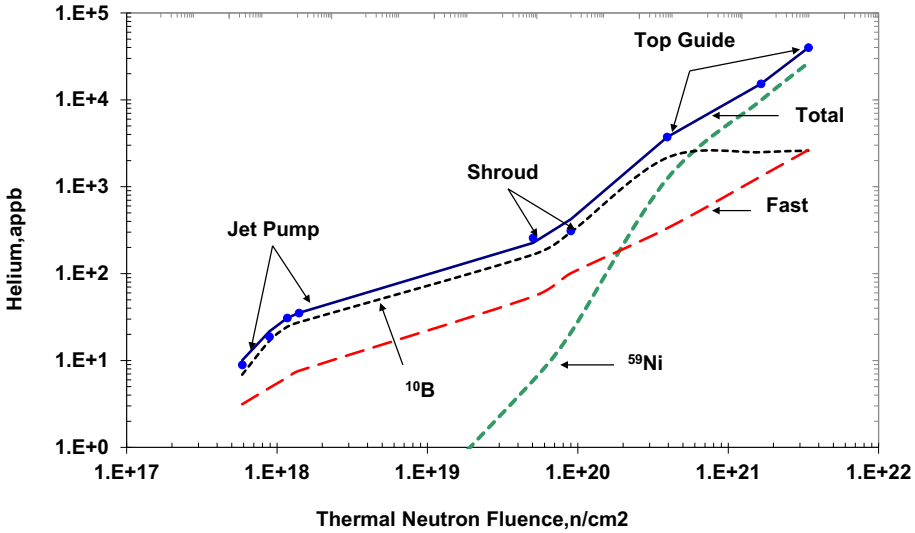

Fig. 5. Measured and calculated helium production is shown for steel samples removed from BWR commercial reactors. At low fluence, helium is produced overwhelmingly by boron impurities in reactor steel. However, at higher neutron fluence, ^{59}Ni grows in and overwhelms all other sources of helium [29].

3.2.1 Thermal neutron gas production reactions

Some gas production reactions are of special interest since they can lead to significant increases in transmutation as well as additional radiation damage. Some reactions of interest are listed in table 1 while the most up to date experimental information are available in [28].

At low neutron fluence in fission reactors, gas production is relatively small since it is produced by fast neutron (n, p) and (n, α) reactions which have higher neutron thresholds where the flux is relatively low. ^{10}B and ^{6}Li reactions are the only ones that can produce significant transmutation and additional radiation damage since the other nuclides such as ^{59}Ni are not present and take time to grow in. Boron is frequently found in reactor steels and will thus be the main source of helium production at low neutron fluence. Helium production from boron impurities in reactor steel frequently produce more helium than the fast neutron (n, α) reaction, as shown in fig. 5. However, at higher neutron fluence, ^{59}Ni starts to grow in and eventually becomes the major source of helium production, as illustrated in fig. 5.

The impact of neutron damage from ^{59}Ni can be seen by looking at the atomic recoil distribution caused by neutron irradiation of Ni. Figure 6 shows that for an irradiation in the High Flux Isotope Reactor (HFIR) at Oak Ridge National Laboratory, most of the atomic recoils have very low energies since they are caused by elastic and inelastic scattering. Note the high-energy recoil spike due to the ^{59}Ni reaction caused by the very energetic ^{56}Fe recoil at 340 keV. This leads to high hydrogen and helium production as well as a significant increase in displacement damage, as shown in table 2.

Note that the high helium production and the significant increase in dpa is caused by ^{59}Ni.

The impact of the ^{59}Ni reaction on reactor steels is shown in figs. 6 and 7. Figure 6 shows the significant increase in helium in 316 stainless steel at higher fluence. However, it should be noted that the concentration of ^{59}Ni peaks at a thermal neutron fluence of about 3×10^{22} n/cm^2 due to the high burnout of ^{59}Ni from the total absorption cross-section of about 94 barns, as shown in fig. 7.

The impact of ^{59}Ni was dramatically demonstrated in the study of stress relaxation in Inconel X-750 springs irradiated in CANDU reactors, as shown in [30].

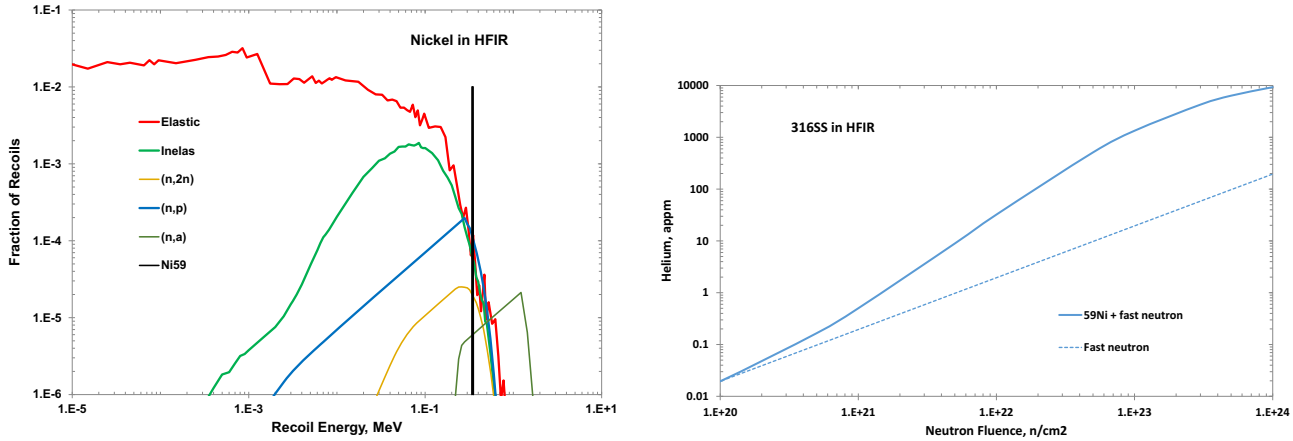

Fig. 6. Left: atomic recoil fractions are shown by nuclear reactions for an irradiation in the HFIR. Right: significant increase in ^{59}Ni-induced helium for 316 stainless steel irradiated, also in HFIR.

Table 2. Comparison of radiation damage in Fe and Ni for an irradiation in HFIR to 4.78×10^{22} n/cm^2.

	Iron		Nickel	
Reaction	% dpa	He, appm	% dpa	He, appm
Elastic	67.8%		45.3%	
Inelastic	29.8%		11.7%	
(n, px)	0.35%		1.82%	
(n, ax)	0.05%	3.34	0.44%	43.9
(n, 2n)	0.04%		0.29%	
(n, g)	1.90%		2.35%	
^{59}Ni			38.1%	3318.8
Total He		3.34		3362.7

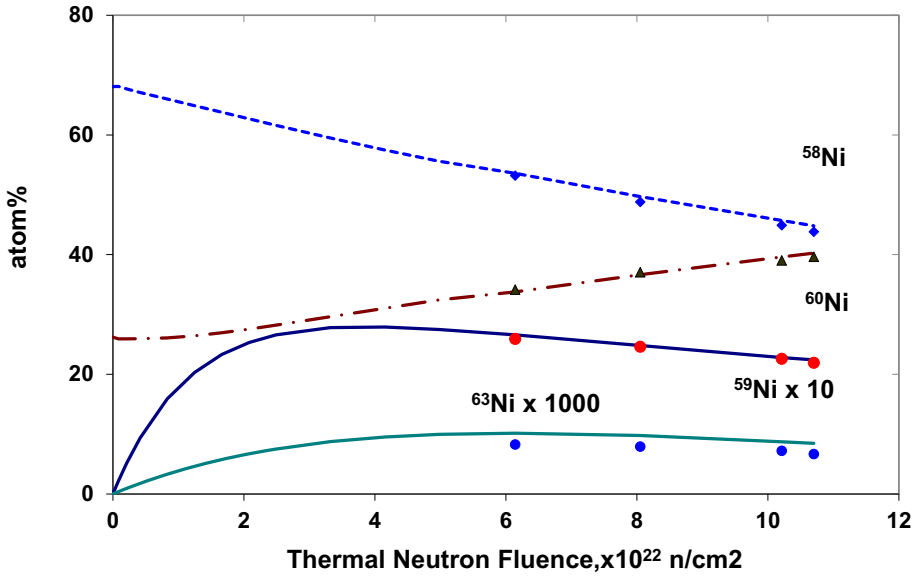

Fig. 7. Comparison of measured and calculated Ni isotopes *versus* thermal neutron fluence.

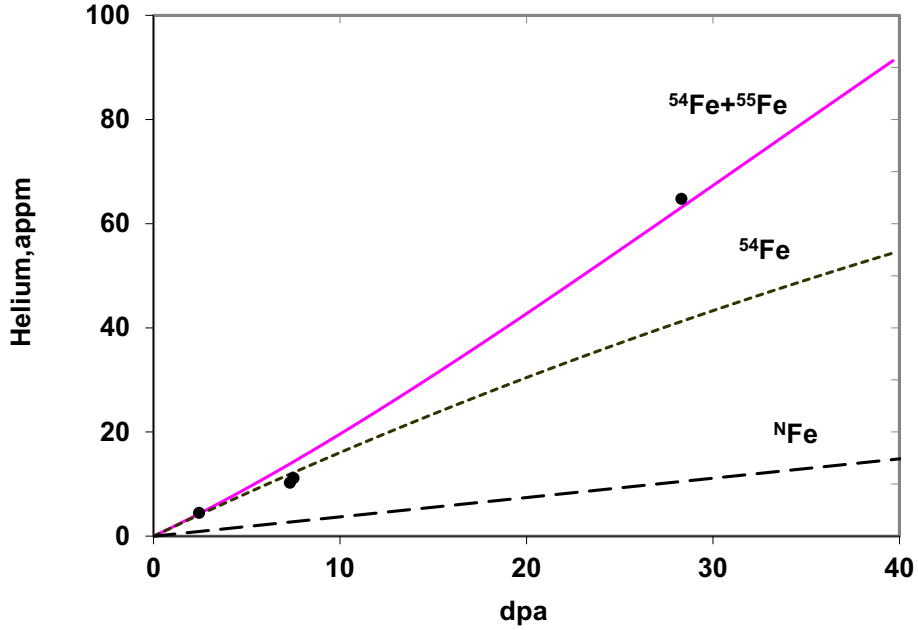

Fig. 8. Measured helium (solid circles) compared with calculated helium production (lines) from natural iron and iron enriched to 96% with ^{54}Fe. The non-linear curve (top) is characteristic of two-step reactions that require time for build-up of ^{55}Fe.

3.2.2 Enhanced hydrogen production from ^{59}Ni

Hydrogen production from (n, p) reactions in fission reactors exceeds that of helium production from (n, α) reactions in most materials since the energy threshold is much lower and the neutron flux is higher. However, hydrogen is generally not of concern due to the high hydrogen mobility at the operating temperature in reactors and there are also large amounts of environmental hydrogen found in water-cooled reactors as well as un-irradiated materials. Experiments have shown that in some cases, the measured hydrogen in irradiated samples exceeds the calculated values [31]. This is surprising given the high mobility of hydrogen at elevated temperatures. The explanation is thought to be that hydrogen can be trapped in helium bubbles and indeed the high hydrogen measurements are for samples that also have high concentrations of helium bubbles. The ^{59}Ni(n, p) and (n, γ) reactions also contribute to displacement damage and the He(appm/dpa) ratio in table 1 takes all three ^{59}Ni reactions into account.

3.2.3 Enhanced gas production in Fe and Cu

Experimental measurements of Fe samples irradiated in HFIR showed a lot more helium than can be explained by the fast neutron reactions (n, He) [31]. Subsequent investigations led to the conclusion that ^{55}Fe must have a small thermal neutron cross-section for helium production. This was later confirmed by preparing F82H (7.1Cr-1.8W-0.55Si-0.40Mn-0.17V-0.1C-0.04Ta) samples with ^{54}Fe (96%) and co-irradiating with natural Fe samples in the FIST experiment in HFIR [32]. Calculations to fit the measured helium production showed that the higher rate of helium production in the ^{54}Fe-doped samples could be explained by the combination of the higher fast neutron (n, α) cross-section of ^{54}Fe as well as a predicted thermal neutron (n, α) reaction in ^{55}Fe of about 0.009 b, as shown in fig. 8. More recent calculations using ^{55}Fe energy-dependent cross-sections in TENDL are best fit with a larger thermal neutron cross-section of 0.027 b for ^{55}Fe [33,34]. Calculations show that the helium production in alloys containing iron can be greatly enhanced by doping with ^{55}Fe and ^{54}Fe, although the short-lived nature of the former —a radioactive unstable isotope— would make such an approach in that case challenging.

Irradiations of copper samples in HFIR showed a significant non-linear increase in helium production with increasing neutron fluence [35]. Such a non-linear effect is characteristic of the in-growth on a reaction product that has a thermal neutron (n, α) cross-section such as ^{59}Ni. Calculation showed that the additional helium is produced by the ^{65}Zn(n, α) reaction and that the thermal cross-section is about 2 barns. The enhancement of helium production in copper is much smaller than seen for ^{59}Ni since three reactions are required rather than 2. The Cu effect would be more comparable to the ^{59}Ni case if zinc was irradiated rather than copper. The Cu reactions are ^{63}Cu(n, γ)^{64}Cu(β^-)^{64}Zn(n, γ)^{65}Zn(n, α). ^{64}Cu also partly decays to ^{64}Ni, further reducing the impact of this reaction. Figure 9 compares helium production in Cu calculated for the Fast Test Flux Facility (FFTF), HFIR, and a fusion first wall spectrum.

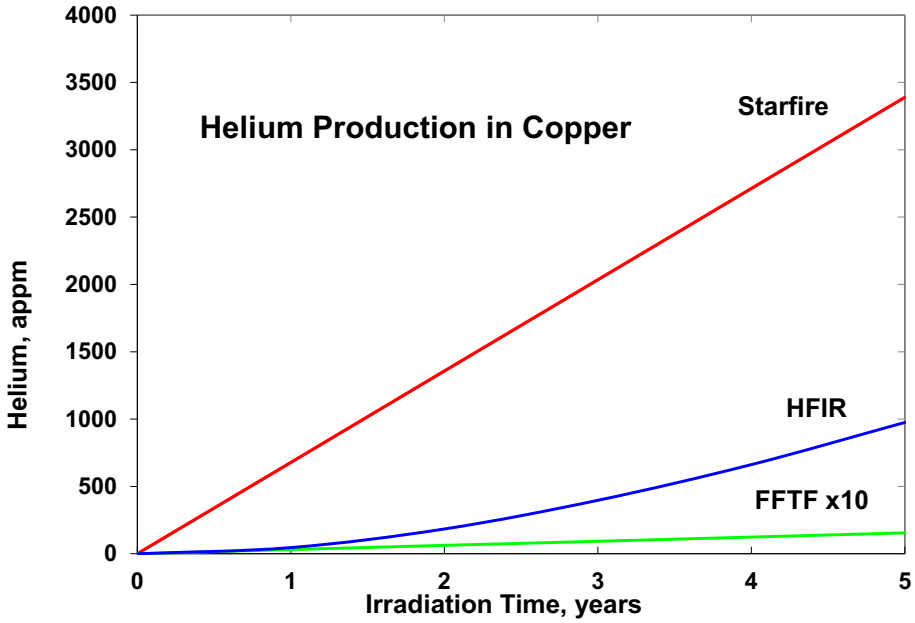

Fig. 9. Enhanced helium production in HFIR compared to FFTF and a fusion first wall spectrum.

Table 3. Transmutation by thermal neutron capture.

Reaction	Sig. barns	Significance
$^{50}\mathrm{Cr}(\mathrm{n},\gamma)^{51}\mathrm{Cr}(\beta^-)^{51}\mathrm{V}$	15.5	Loss of Cr in alloys
$^{55}\mathrm{Mn}(\mathrm{n},\gamma)^{56}\mathrm{Mn}(\beta^-)^{56}\mathrm{Fe}$	13.3	Loss of ductility in SS
$^{63}\mathrm{Cu}(\mathrm{n},\gamma)^{64}\mathrm{Zn} + {}^{64}\mathrm{Ni}$	4.5	Non-linear He prod.
$^{186}\mathrm{W}(\mathrm{n},\gamma)^{187}\mathrm{W}(\beta^-)^{187}\mathrm{Re}$	40	W loss to Re and Os
$^{181}\mathrm{Ta}(\mathrm{n},\gamma)^{182}\mathrm{Ta}(\beta^-)^{182}\mathrm{W}$	20	Transmutation to W
$^{191}\mathrm{Ir}(\mathrm{n},\gamma)^{192}\mathrm{Ir}(\beta^-)^{192}\mathrm{Pt}$	920	Rapid growth of Pt
$^{193}\mathrm{Ir}(\mathrm{n},\gamma)^{194}\mathrm{Ir}(\beta^-)^{194}\mathrm{Pt}$	1500	Rapid growth of Pt

3.2.4 Transmutation from thermal neutron capture reactions

Enhanced transmutation occurs in nuclides having significant thermal (n,γ) cross-sections. Several reactions of interest for radiation damage in materials are listed in table 3. Since these reactions are caused by thermal/epithermal neutrons, the impact compared to fast neutron dpa is very dependent on the neutron spectrum in a given facility as well as the location in the facility. Consequently, thermal neutron transmutation may not correlate with fast neutron damage effects. The importance of thermal neutron transmutation is that it immediately changes the composition of a pure material or alloy and may eventually profoundly change the material properties as the loss or introduction of elements becomes significant. Such effects may be more important than displacement damage in determining the lifetime of materials under irradiation. For example, the loss of Mn in stainless steel has been associated with loss of ductility.

3.2.5 New evaluation with uncertainties for ^{59}Ni

As stated in the previous sections, ^{59}Ni and its gas producing reactions are important for material damage in steel. In particular, neutron-induced helium production causes embrittlement in stainless steel [36].

Before this work, existing evaluated ^{59}Ni data had no uncertainty information for neither the (n,α) nor for the (n,p) reaction in the thermal region.

Consequently, a new evaluation covering all the ^{59}Ni channels has been developed, which was included in the JEFF 3.3 release. The method also produced 300 random files including all the information to describe the full PDF of

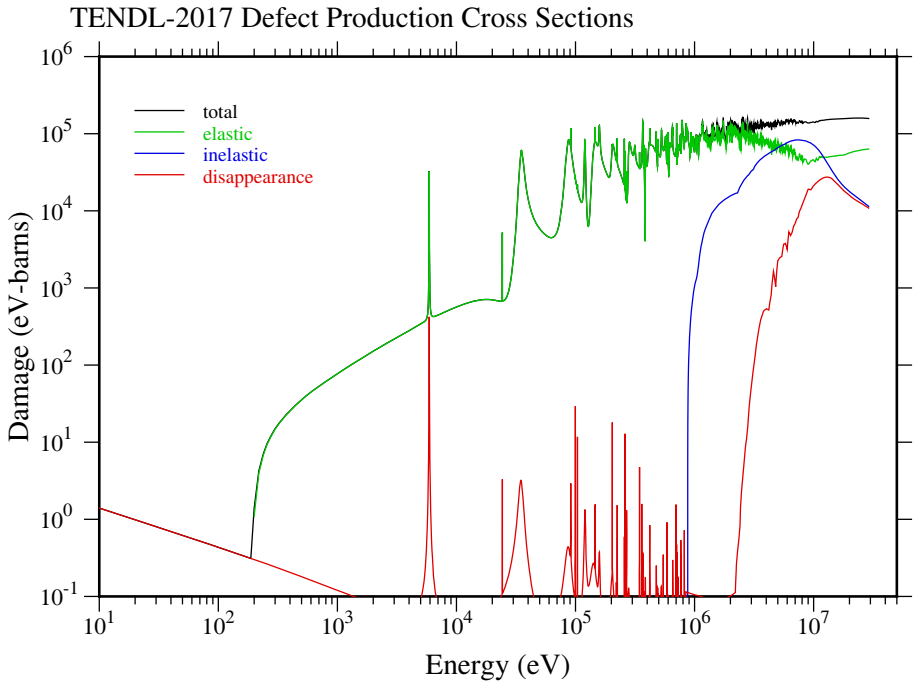

Fig. 10. Example of radiation damage energy productions for ^{27}Al from ENDF/B-VIII, TENDL-2017, note the different components and their dominance over energies.

the ^{59}Ni data for all cross-sections (see fig. 2, which is a result of this work), angular distributions, etc. 300 random files are what is typically used in Total Monte Carlo (TMC) uncertainty propagation [37] and are deemed enough to converge at least the two first moments of the PDF [38] to a sufficient degree. The evaluation is based on three main components:

1) An analysis of available thermal cross-section experiments and the forward sampling of correlated error components.
2) Resonance parameters (including alpha and proton widths) provided by J.A. Harvey (EXFOR entry 10680), supplemented by adding error components to the gamma, alpha and proton widths that approximate the systematic errors for underlying (n,γ), (n,α) and (n,p) cross-section measurements.
3) TALYS [39] results using the parameter distribution of TENDL-2015 [38,37,40], including average level spacings and resonance widths.

The resonance widths of bound resonances are sampled based on the TALYS average parameters and adjusted such that the distribution of resonance parameters match the distribution of thermal cross-sections. Full details of the methodology are found in ref. [41]. The main aim was to provide justified co-variance data for ^{59}Ni in general and in particular for the alpha reaction. The full energy-energy covariance for all the important reaction channels is illustrated in fig. 6 of [41]. As can be seen, co-variance information is provided for all the channels, including cross-channel correlations.

To summarize, more justified complete gas-production cross-sections with uncertainties for ^{59}Ni has been produced, as part of the CRP. We propose that the presented method, which includes justified covariance data for all important channels, including cross-channel correlations, as well as for angular distributions in the high energy range, can serve as an example for the continued nuclear data evaluation work for the damage community.

3.3 Primary damage metrics: DPCSs, PKAs and DPAs

3.3.1 Damage energy production cross-section and displacement per atom

When a material is irradiated with neutrons, the induced nuclear reaction in the material produces Primary Knock on Atoms (PKAs) recoils. Lattice defects can be induced by the primary recoil target, residual or emitted particles of a nuclear reaction as it slows down, de-excites in the lattice. It has been shown that an empirical correlation exist between displacement per atom and various properties of metal alloys [42]. The HEATR module in NJOY [43–45] is used to calculate a Defect Production Cross-Section (DPCS) for displacement per atoms based on damage energy see fig. 10, or E_{dam} and is conveniently outputs in units of (eV barns). This is the metric outputted by NJOY and

Table 4. Typical values for elemental atomic displacement energy needed to compute DPAs [47,46], 25 eV otherwise.

Element	E_d (eV)	Element	E_d (eV)
Be	31	Co	40
C	31	Ni	40
Mg	25	Cu	40
Al	27	Zr	40
Si	25	Nb	40
Ca	40	Mo	60
Ti	40	Ag	60
V	40	Ta	90
Cr	40	W	55
Mn	40	Au	30
Fe	40	Pb	25

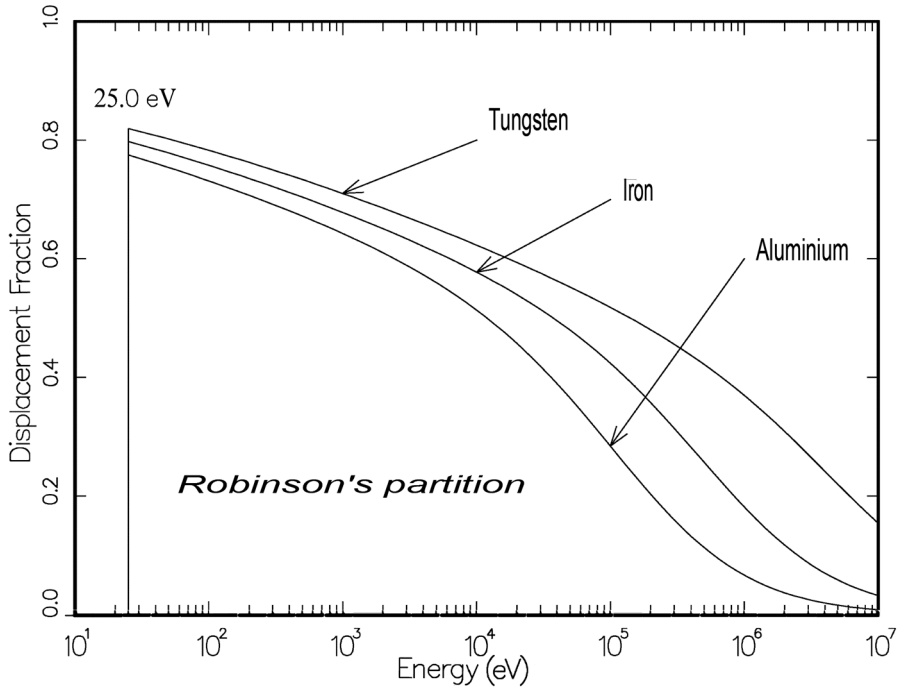

Fig. 11. $P(E)$ from eq. (16) divided by E, 25 eV cutoff discussed in table 4. Data from [44].

multiplying by the atomic density N and flux ϕ gives (eV s^{-1}). Finally, dividing by the minimum energy required to displace an atom from its lattice position E_d it lead to DPA per second. Therefore the number of Displacements per Atom (DPA) per second produced can be deduced from the NJOY output as

$$\mathrm{DPA/s} = \frac{E_{dam}}{2E_d} N\phi. \tag{15}$$

Those latter steps are usually part of the post-processing although in modern simulation platform such as FISPACT-II [46] this can be performed for all libraries, for all element/material in every irradiation condition. NJOY's HEATR module calculates E_{dam} from the data contained in the evaluated files, which will be described below. The energy displacement parameters that need to be used afterwards are given in table 4. The result from eq. (15) is often reduced by an efficiency factor (say 80%) derived from primitive atomistic simulation to improve the fit to the empirical correlations.

Figure 11 shows examples of the fraction of the primary recoil energy that is available to cause lattice displacement in W, Fe or Al metallic lattices while the remaining energy leads to electronic excitation.

In the ENDF format, the secondary angular distribution is given in File 4 and the secondary energy distribution is given in File 5. Some newer evaluations give coupled energy-angle secondary distributions in File 6. The process for calculating the damage cross-section E_{dam} differs slightly depending on the data that is available. Each format, however, uses the damage partition function,

$$P(E) = \frac{E_R}{1 + F_L(3.4008\epsilon^{1/6} + 0.40244\epsilon^{3/4} + \epsilon)}\,. \tag{16}$$

Note the sharp drop at 25 eV in fig. 11. This is due to a cutoff built-in to NJOY; if $E_R < 25\,\text{eV}$ then $P(E) = 0$. In eq. (16), E_R is the primary recoil energy which will be given later. The remaining parameters are defined as follows:

$$\epsilon = \frac{E_R}{E_L}\,, \tag{17}$$

$$E_L = 30.724 Z_R Z_L \left(Z_R^{2/3} + Z_L^{2/3}\right)^{1/2} (A_R + A_L)/A_L \tag{18}$$

and

$$F_L = \frac{0.0793 Z_R^{2/3} Z_L^{1/2} (A_R + A_L)^{3/2}}{(Z_R^{2/3} + Z_L^{2/3})^{3/4} A_R^{3/2} A_L^{1/2}}\,. \tag{19}$$

Here, Z_i and A_i refer to the charge and atomic number of the lattice nuclei (L) and the recoil nuclei (R).

For elastic and two-body discrete-level inelastic scattering, the primary recoil energy is

$$E_R(E, \mu) = \frac{AE}{(A+1)^2}\left(1 - 2R\mu + R^2\right), \tag{20}$$

where the "effective mass" is given by

$$R = \sqrt{1 - \frac{(A+1)(-Q)}{AE}} \tag{21}$$

and μ is the center-of-mass scattering cosine. For evaluations that have data given in File 6, the primary recoil energy is given by

$$E_R = \frac{A'E}{A+1}\left(1 + 2R\mu + R^2\right), \tag{22}$$

where

$$R = \sqrt{\frac{A(A+1-A')}{A'}} \tag{23}$$

and A' is the ratio of the mass of the outgoing particle to that of the incident particle. Note the subtle change in the sign of the second term in the parentheses in E_R as compared to eq. (21). The DPCS is then obtained from

$$E_{dam}(E) = \sigma(E) \int_{-1}^{1} f(E, \mu)\, P(E_R[E, \mu])\, \mathrm{d}\mu. \tag{24}$$

Here, f is the angular distribution from File 4 of the ENDF evaluation. Continuum reactions, like (n, n′) give a recoil spectrum,

$$E_R = \frac{E}{A+1} - 2\sqrt{\frac{E}{A+1}}\sqrt{\frac{E_\gamma^2}{2(A+1)mc^2}}\cos\phi + \frac{\overline{E_\gamma^2}}{2(A+1)mc^2}\,, \tag{25}$$

where E' is the secondary neutron energy and μ is the laboratory cosine. In this case, the DPCS is defined as

$$E_{dam}(E) = \sigma(E) \int_0^\infty \mathrm{d}E' \int_{-1}^{1} \mathrm{d}\mu\, f(E, \mu)\, g(E, E')\, P(E_R[E, E', \mu]), \tag{26}$$

where g is the secondary energy distribution from File 5.

Numerical values for 83 naturally occurring elements (assembled from their isotopic parts) total and partial neutron defect production, gas production cross-section and kerma factors systematically and uniquely derived from ENDF/B-VIII.0, JENDL-4.0 and TENDL-2017 files using the latest NJOY's HEATR protocol are accessible through [48].

Another module of NJOY, GROUPR is also used to calculate residual nucleus ($A > 4$) and emitted particle matrices: energy-angle distribution, see fig. 12. This is also of prime importance to provide better, more detailed metrics, energy-dependent recoil atom and emitted particle spectra, to material science applications. SPECTRA-PKA applications library files covering 287 stable targets, derived from TENDL-2017 are available from [46].

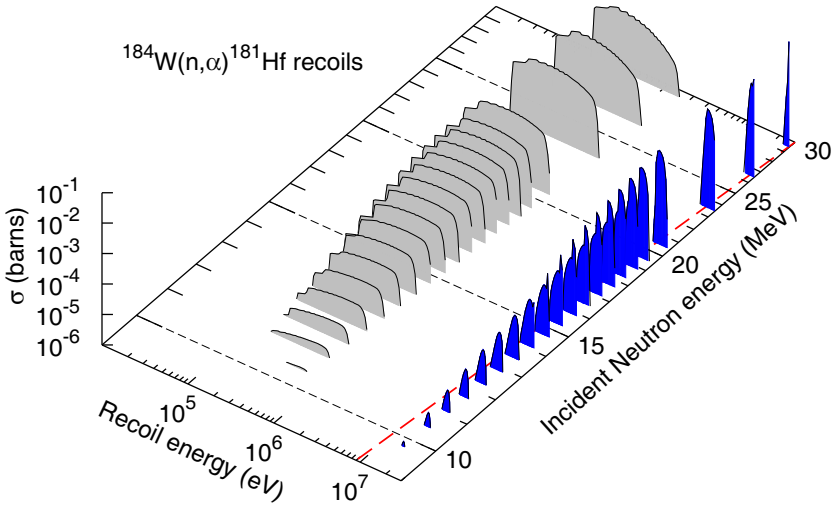

Fig. 12. Positive Q (+7.3 MeV) (n,α) on ^{184}W recoil distributions, separated for the residual ^{181}Hf (grey), and emitted ^{4}He (blue). The red line represents the energy at which the recoil energy is equal to the incident neutron energy, demonstrating that the emitted particle energies are higher than the incoming neutron because of the positive Q value.

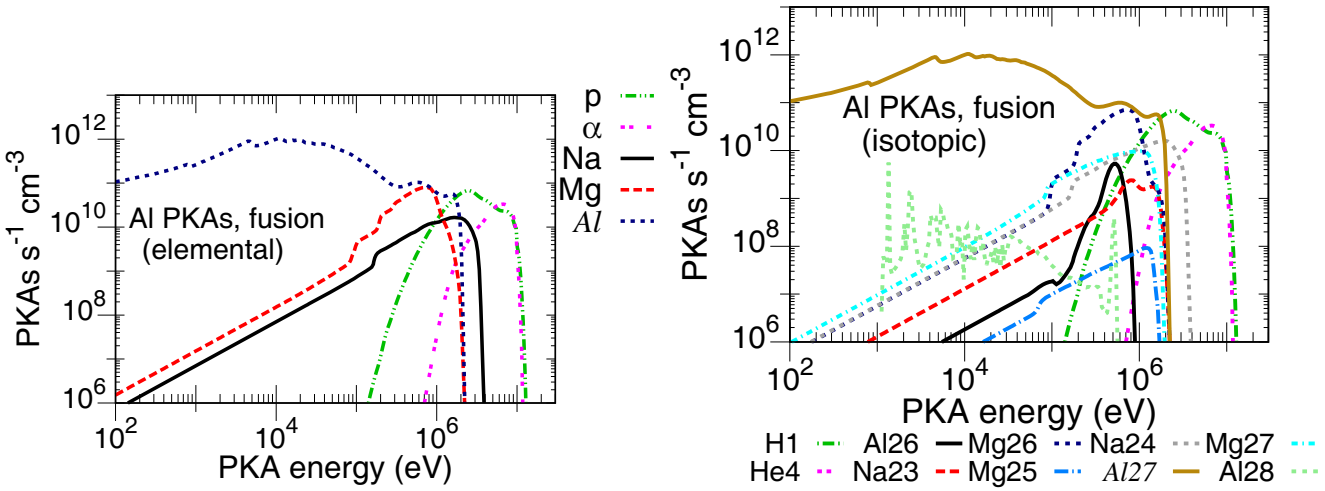

Fig. 13. Pure aluminium (100% ^{27}Al) transmuted residual elements and isotopes with emitted particle PKA distributions under fusion neutron conditions.

3.3.2 Damage energy spectra

The recently developed SPECTRA-PKA [49–51] code reads-in the aforementioned recoil matrices and combines these with an incident neutron energy spectrum to define PKA event and energy distributions. The code follows a similar methodology to previous programs, such as SPECTER [30], but has the advantage of being fully compatible with the latest modern nuclear data libraries, for both neutron and charge particles, and can handle fine group structures. The code can also consider any complex material composition containing an arbitrary distribution of target nuclide species. Even more significantly, it treats every nuclear reaction channel (on every target nuclide considered), and its associated recoil matrix, separately, which allows a deeper interrogation of the underlying nuclear data.

Figures 13 show two examples of the detailed output afforded by the approach taken by SPECTRA-PKA. The first, shows the elemental (and emitted secondary light gas particle) contributions to the PKAs produced in pure aluminium under a fusion neutron irradiation field. As would be predicted, recoils of Al dominate and are mainly caused by simple scattering events on the host ^{27}Al atoms. However, there are significant PKA distributions of Mg and Na, as well as from light alpha (^{4}He) particles and protons (^{1}H), which originate from more exotic reactions, such as (n,α) and (n,p). This capability (to separate contributions due to different reaction types) is a powerful unique feature of SPECTRA-PKA and offers future compatibility with advanced materials modelling efforts, where the impact of damage cascades initiated by foreign atomic species introduced into a host lattice can be accounted for.

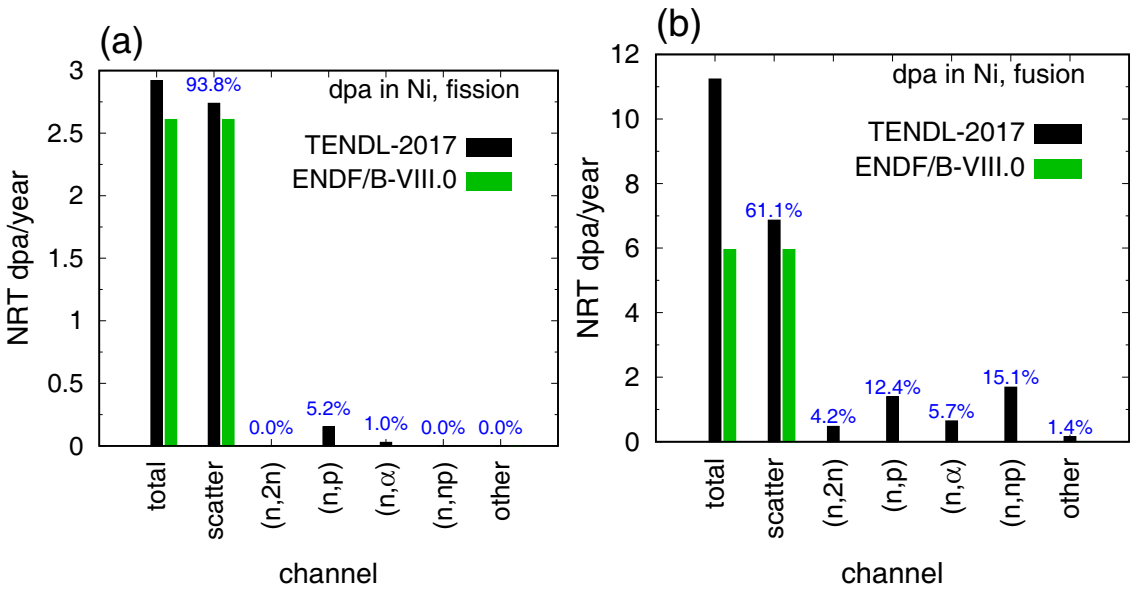

Fig. 14. dpa contributions to the total damage rate in pure Ni under (a) typical PWR (fuel assembly average) and (b) typical fusion power plant first wall conditions. Results are given for evaluations using two different nuclear data libraries. The % contributions from each reaction channel (summed over all target nuclides in pure Ni) for the TENDL-2017 [53] library evaluations are given above each bar.

The second picture shows the additional complexity even further, by separating out the contributions to the elemental PKA distributions of Al from the different nuclides, showing, for example, that the Al distribution in fig. 13 is actually the sum of PKA distributions of ^{27}Al, ^{26}Al, and ^{28}Al.

More recently [52], the per-channel capabilities of SPECTRA-PKA have been exploited to analyze the relative significance of different nuclide channels to dpa damage production rates.

For example, fig. 14 shows the dpa-rate contributions in pure nickel under two different neutron irradiation scenarios. The plot includes results from recoil matrices extracted by NJOY2016 from the recently released TENDL-2017 [53, 40] and ENDF/B-VIII.0 [54] nuclear data libraries. Figure 14(a) shows results under typical pressurized water fission reactor (PWR) conditions —in this case the fuel assembly-averaged spectrum for the type P4 pressurized-water reactor at the Paluel site in France— and fig. 14(b) shows the dpa breakdown under the predicted conditions in the plasma-exposed first wall of a conceptual design for a fusion power plant.

The first noteworthy point in the figure is the absence of dpa contributions in either plot from non-elastic reactions when using the ENDF/B-VIII.0 library, leading to an underestimation in the total dpa rates relative to TENDL-2017. For example, the ENDF/B-VIII.0 library predicts only 6 dpa/year under fusion DEMO conditions, while TENDL-2017 predicts more than 11. This is due to the absence of the appropriate nuclear data forms (recoils, and particle spectra-angular distributions) in the data-blocks of the ENDF6 [55] formatted files used to represent the nuclear data in this library. This highlights an important aspect of nuclear library data preparation and testing —namely that a file may not be truly general purpose if it does not cater for all possible aspects of the nuclear physics and application forms. In this particular case the ENDF/B-VIII.0 files has a handicap when used to evaluate PKA distributions or derive dpa rates for high energy applications.

Considering only the TENDL-2017 results, fig. 14 shows several key differences between the dpa rates in the two nuclear environments. Firstly, under PWR fuel assembly conditions the total dpa per year is nearly a factor of four lower than the rate predicted under fusion first-wall conditions due to the preponderance of highly damaging, high energy above 2 MeV neutrons generated from the deuterium-deuterium-tritium fusion reaction in the latter case, although there is also a lower total neutron flux in the PWR case (only 65% of the fusion case). This is a well-known prediction, demonstrating the additional challenges for material survival in future fusion power plants compared to those encountered in fission systems.

Another interesting difference between the two sets of results, and one that the advanced features of SPECTRA-PKA are able to highlight, is the change in the proportion of the dpa coming from different reaction channels. In the fission case (fig. 14(a)) scattering (elastic and inelastic scattering have been combined in the plots) makes up more than 90% of the total dpa rate and there are only minor contributions from non-elastic reactions such as (n, p) and (n, α). Under fusion conditions, on the other hand, scattering only accounts for around 61% of the dpa (the % contributions to the total in the TENDL-2017 case are given above each bar) —note that ENDF/B-VIII.0 and TENDL-2017 agree

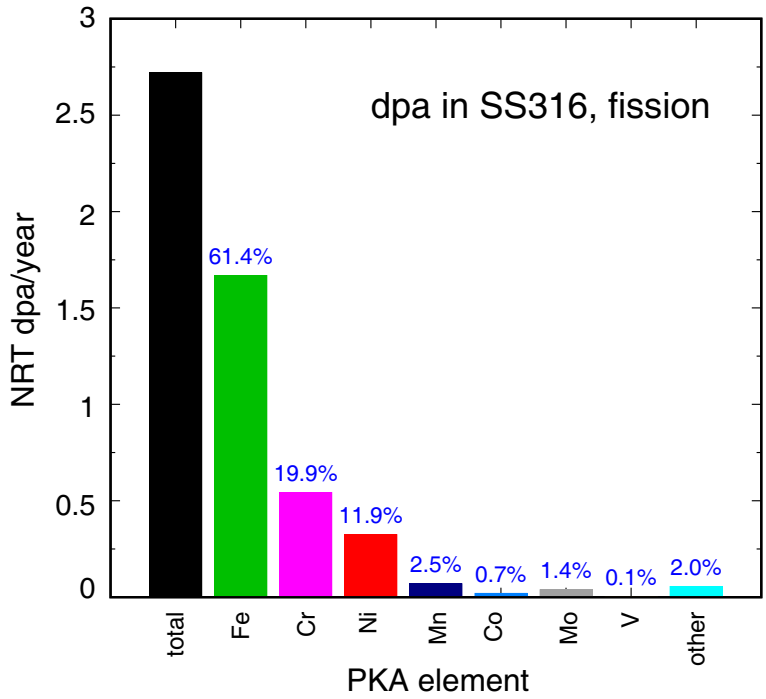

Fig. 15. dpa contributions to the total damage rate in SS316 steel under PWR conditions. Results computed using TENDL-2017 data have been separated according to the recoil element produced during nuclear reaction —*i.e.* the result for "Fe" is the total dpa produced from all reaction on the nuclides of SS316 that have Fe as the recoil daughter. The % contributions from each recoil element are given above each bar.

well in their predictions of the dpa contribution from scattering, but ENDF/B-VIII.0 misses the remainder. The rest of the dpa comes from other threshold reactions, in particular from proton (hydrogen)-producing (n, p) and (n, np) reactions (27.5% of the dpa total), which have relatively high reaction rate in a fusion energies range (around 300 mb in the (n, p) case and around twice that for (n, np) on the main ^{58}Ni isotope). Thus these, more exotic, reactions and their proper evaluation, are more critical for nickel (and for many other materials) under fusion conditions.

Figure 15 demonstrates another important capability of PKA evaluation, namely the ability to consider complex material compositions. Of course, this is standard in many nuclear analysis codes for inventory, burn-up or transport calculations, but SPECTRA-PKA can consider damage contributions (PKAs and dpa) for any distribution of nuclides in the same per-reaction-channel framework. The figure shows the dpa contributions to 316 stainless steel under PWR conditions. In this case the complexity is illustrated by considering the dpa contributions as a function of reaction-daughters under the hypothesis that the way damage will be created will vary according to the elemental species forming the PKA. The results (only for TENDL-2017) show the expected dominance of the main elements in SS316, which are mainly produced as PKAs via scattering reactions —in fact the % contributions from Fe, Ni, and Cr, match well with their respective atomic concentrations in SS316 (see [52]). This result contrasts to that reported earlier [52] for 316 under fusion conditions, where there were more significant contributions from transmuted elements such as Co.

An additional highlight from the SPECTRA-PKA framework is the consideration of the contribution to displacement events from decay events. Under irradiation it was shown in [50] that the extra recoils from the decaying residuals generated by transmutation were not a significant contributor to the overall PKA rates. However, these "decay-recoils" will continue to be present even after the irradiation has terminated, and will then be the only source of displacement damage events (potentially for many years). Figure 16 compares the approximate decay-recoil contributions to the PKA rates in irradiated tungsten after 1 year of irradiation. Note that the elemental picture of the PKAs from the neutron irradiation field at $t = 1$ year (as shown) is quite different to the picture at $t = 0$ because of the growth of transmutation elements. These transmutant PKA contributions are additionally joined by the set of point PKA-rate approximations from the various decay-species in the composition at this time.

3.3.3 Primary Knock on atoms spectra using the PHITS code

The usual method to calculate PKA energy spectra from low-energy neutron events ($E_n < 20$ MeV) is to use an evaluation code such as the SPECTRA-PKA program described in the previous sub-section. However, prior to this the data themselves need to be processed (for example, by NJOY-2012). Such derived data have yet to be validated,

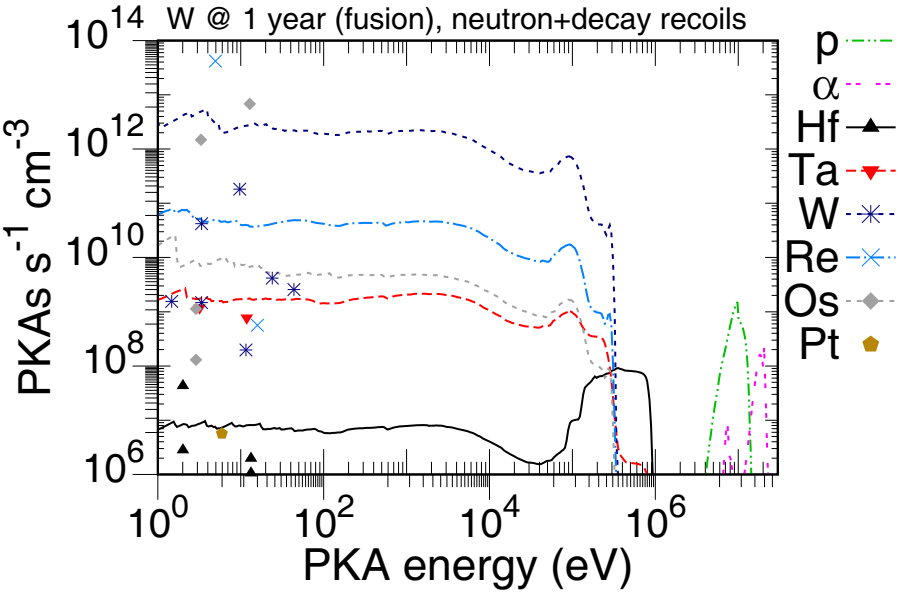

Fig. 16. PKA contributions from both transmutant/descendant elements (curves) and decaying species (points) to the PKA distributions in pure tungsten after a 1 year irradiation in a typical fusion neutron field —see [50] for more details.

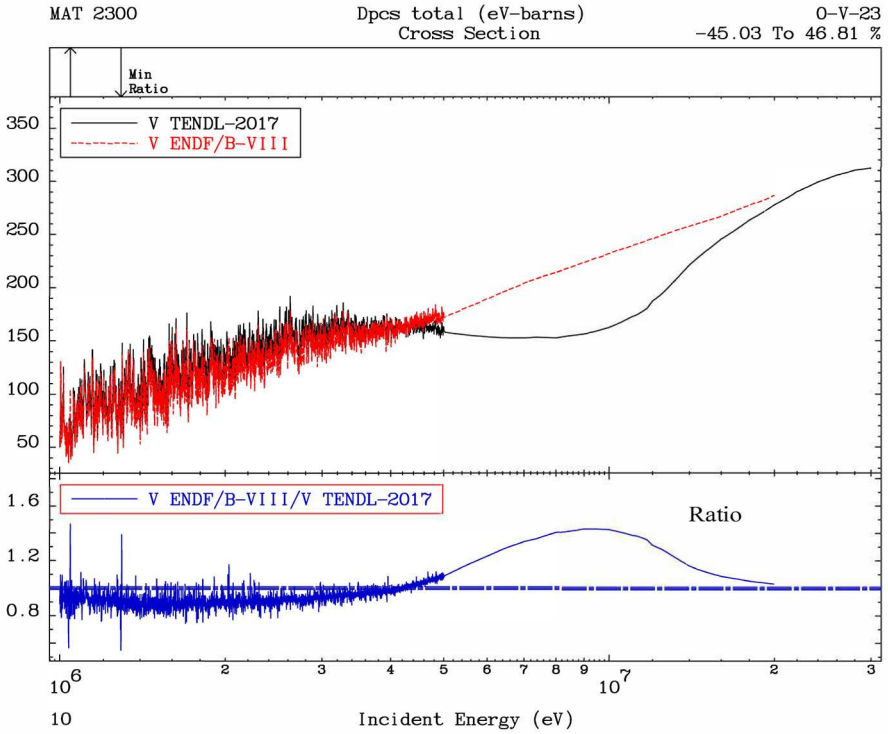

Fig. 17. Damage energy cross-sections for natural vanadium, derived from TENDL-2017 and ENDF/B-VIII.

but differences can already seen when qualitatively comparing the output from different nuclear data libraries; for example in fig. 17, a comparison of total dpa cross-sections reveal significant differences at higher incident neutron energies. This is a remark of importance for fusion as the higher energy ($\sim 14.5\,\mathrm{MeV}$) of incident neutrons in fusion systems (compared to that of fission $\sim 2.0\,\mathrm{MeV}$) trigger many more reaction channels, which in turn produce more complex energy distributions and PKA's types. The Particle and Heavy Ion Transport code System (PHITS) [56, 57] has recently been enhanced with an event generator mode (EGM) [58,59] mainly developed for incident neutron reactions of energies below 20 MeV.

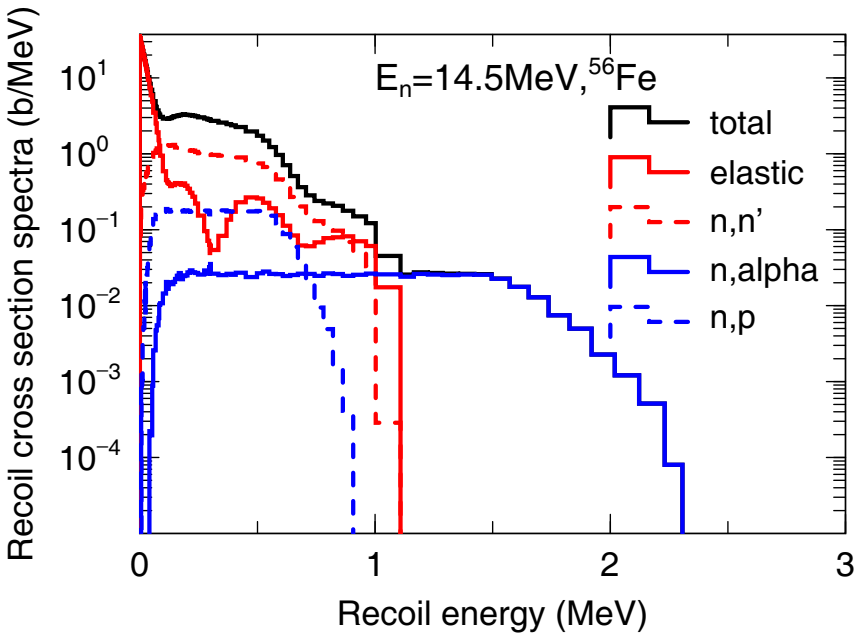

Fig. 18. Partial recoil cross-section spectra for total, elastic, (n,n'), (n,p), and (n,α); interactions on ^{56}Fe at incident neutron energies of 14.5 MeV calculated using PHITS-EGM based on JENDL-4.0.

EGM is capable of outputting PKAs while conserving the energy and momentum of every event or reaction. Its main usage is to be capable of analysing event by event for applications such as response function simulation of detectors, soft error analysis in semiconductors, microdosimetry in the human body, and, in the present context, PKA and DPA estimation in irradiated structural materials [60].

The PHITS-EGM combination simulates particle energies and emission angles while conserving energy and momentum on an event-by-event basis under low-energy (< 20 MeV) neutron irradiation conditions. In the first instance, the Monte Carlo method is used to sample reactions from reaction-channel cross-sections, such as elastic (n,γ), inelastic (n,Xn), (n,p), (n,d), (n,t), (n,α), $(\mathrm{n},\mathrm{n}'\mathrm{p})$, $(\mathrm{n},\mathrm{n}'\mathrm{d})$, $(\mathrm{n},\mathrm{n}'\mathrm{t})$, and $(\mathrm{n},\mathrm{n}'\alpha)$, from the evaluated nuclear data libraries that have been written in ACE format. When the above channels lead to a neutron emission, the double differential cross-sections of the outgoing neutrons in the evaluated nuclear data library are used to determine the energy, momentum, and scattering angle of the emitted neutrons; the momentum of the recoils is then determined accordingly.

When a radiative capture or single charged particle emission reaction is sampled, the excitation energy and momentum of the compound nucleus is derived from the incident energy and the momentum of the neutron and mass of target nucleus. To handle the decay processes of the resulting excited nuclei, a particular mode of the Generalized Evaporation Model (GEM) [61], which produces specific particles and handles gamma de-excitation, the ENSDF-Based Isomeric Transition and isomer production Model (EBITEM) [62] is used to emit the charge particle appropriately. At this point, all information about the ejectiles: charged particles, photons and the residual nuclei; have been determined. Following such methodology, the system is able to handle any low-energy neutron collision as events in which energy and momentum are conserved. This is not always the case when only processed library are available. Figure 18 exemplifies the findings for a neutron incident energy of 14.5 MeV on ^{56}Fe as produced using PHITS-EGM based on JENDL-4.0 [63].

Total recoil cross-section spectra for neutron interactions on ^{56}Fe at incident neutron energies of 14.5 MeV as calculated using PHITS-EGM with TENDL-2015 [38,37], ENDF/B-VII.1 [64], and JENDL-4.0 are shown in fig. 19. A linear energy scale is used in the figure to clearly show the total (sum of the channels in fig. 18) that arise from different libraries. In that particular case the differences are minimum (as ^{56}Fe is the target) simply because the reaction-channel cross-sections in each library are essentially the same. This is far from being the case for every other target. However, with this knowledge, in the following, we adopt PHITS-TENDL-2015 results as a basis for comparison with the results processed by NJOY-2012 with various other nuclear data libraries.

PHITS-TENDL-2015 results alongside identical information extracted from the TENDL-2015, ENDF/B-VII.1, and JEFF-3.2 libraries using protocols from the processing code NJOY-2012 are displayed for an incident energy of 14.5 MeV on an ^{56}Fe target in fig. 20. JENDL-4.0 results could not be used when processed by NJOY-2012 simply because the original file lacked the information (energy and angular distributions) for many of the reactions channels of importance at that energy. There is a good agreement between the PKA energy spectra results derived either from

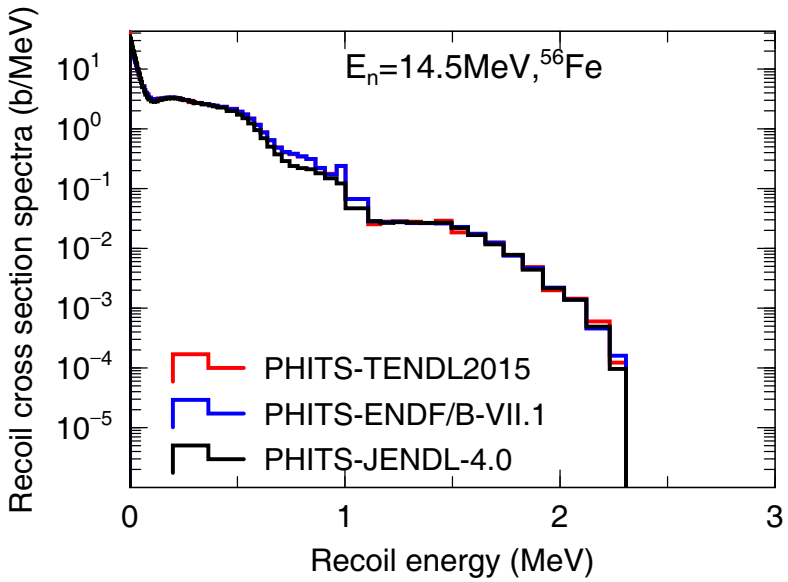

Fig. 19. Recoil cross-section spectra for interactions of neutrons with ^{56}Fe at incident neutron energies of 14.5 MeV calculated using PHITS-EGM with different libraries.

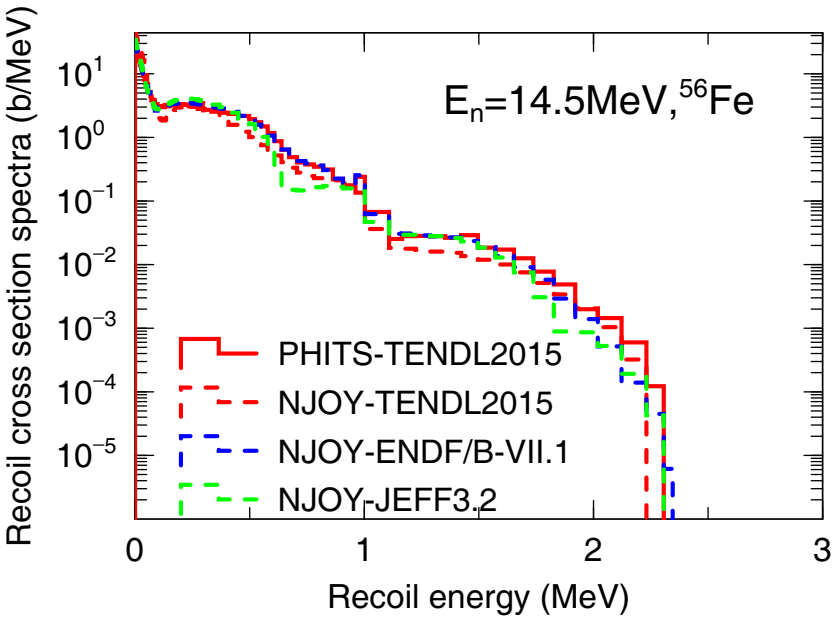

Fig. 20. Recoil cross-section spectra for interactions of neutrons with ^{56}Fe at incident neutron energies of 14.5 MeV calculated using PHITS-TENDL-2015 and NJOY-2012 with different libraries.

PHITS-TENDL-2015 (red solid line) or from NJOY-2012 protocols on the different libraries used (dashed lines). This gives confidence in the processes implemented in PHITS-EGM to simulate the PKA spectra when based on the same evaluated libraries, assuming that all the necessary energy and angular distributions are present in the file.

Figure 21 depicts total recoil cross-section spectra still using PHITS-TENDL-2015, but this time for interactions of neutrons with ^{90}Zr at an incident neutron energy of 14.5 MeV and also extracted from the TENDL2015, ENDF/B-VII.1, and JEFF-3.2 libraries using NJOY-2012 protocols. The agreement between PHITS-TENDL-2015 (red solid line) and NJOY-TENDL-2015 (red dashed line) is acceptable for ^{90}Zr. However, when the same PKA spectra is extracted from JEFF3.2 by NJOY it is noticeably higher than any others in the energy region where the (n, n') and (n, α) reactions dominate. The same tendency has also been noticed when ^{75}As, ^{89}Y, and ^{109}Ag are targets with NJOY-ENDF/B-VII.1 and for ^{55}Mn from NJOY-JEFF3.2 [65]. When ^{90}Zr PKA are extracted from ENDF/B-VII.1 by

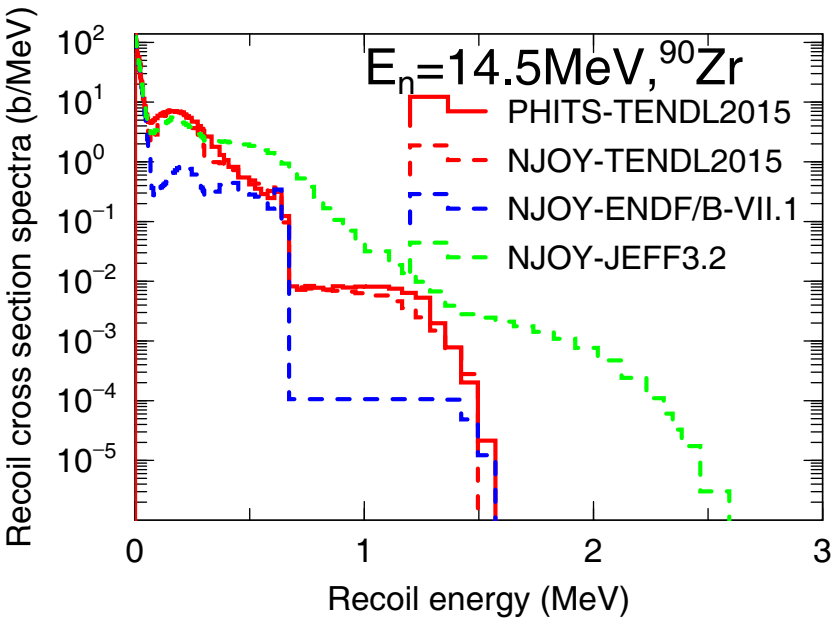

Fig. 21. Recoil cross-section spectra for interactions of neutrons with ^{90}Zr at incident neutron energies of 14.5 MeV calculated using PHITS-EGM-TENDL-2015 and NJOY-2012 with different libraries.

NJOY-2012 (blue dashed line), the spectra is lower than any others. In the present work, the recoiling atoms detailed angular distributions, which can also be outputted by NJOY, are not explicitly retained, although their angular dependence are implicitly considered in as far as their impact on the recoil energy distribution [49] is concerned. Such delicate format frame interpretation issues could partly explain some of the discrepancy seen. One would notice that the same difficulties are seen [65] when ^{7}Li, ^{9}Be, $^{\text{nat}}$C, ^{48}Ti, ^{55}Mn, ^{69}Ga, and ^{184}W are concerned when from ENDF/B-VII.1; but for ^{7}Li, ^{9}Be, $^{\text{nat}}$C, and ^{184}W when from JEFF3.2; and for ^{7}Li and ^{9}Be when from TENDL-2015 also. In this latter case note that TENDL-2015 copied ENDF/B-VII.1.

From the above it can be said that probing the nuclear data landscape, in search for complex derived data such as a PKA's spectra (recoil and secondary particles alike) with different methodologies can highlight certain data deficiencies not previously seen to be of importance for non-material science simulations.

4 Uncertainty propagation and quantification in nuclear data

4.1 How isotopic, element and oxide nuclear data influence the DPCSs and their covariance matrices

Solid (as opposed to liquid, gaseous or plasma state) materials comes with different appellations: metallic, ceramic, composite (oxide, carbonate, etc.), glass, semiconductor, concrete, polymers. Some belong mainly to a world of experiments, but need to be properly assessed since it is from here where most of the material irradiation data arises. With the innovative development of ceramics fuel cladding, vitrification techniques, materials optimisation for space, novel physics experiments and accelerator driven usages there is a need to develop rapid but reliable methods of uncertainty quantification and propagation.

As an example of compound materials the impact of elemental and oxide cross-sections measurements on calculated damage energy cross-sections is illustrated in the case of silicon and oxygen. A Bayesian method is used, showing the existence of cross-isotopes correlations and the changes in the defect production cross-sections and their uncertainties. This is of importance for the calculation of the uncertainties on primary radiation damage produced by displacement events due to nuclear data events.

4.1.1 Motivation

Defect production cross-sections (dpcs figs. 10, 22) can be used to correlate radiation damage induced by neutrons and charged particles in a crystalline materials. Different quantities relating to displacement events can be derived from these dpcs such as Primary Knockout Atoms (PKA) spectra, and lattice defect related Displacement per Atom (or dpa) [66,67].

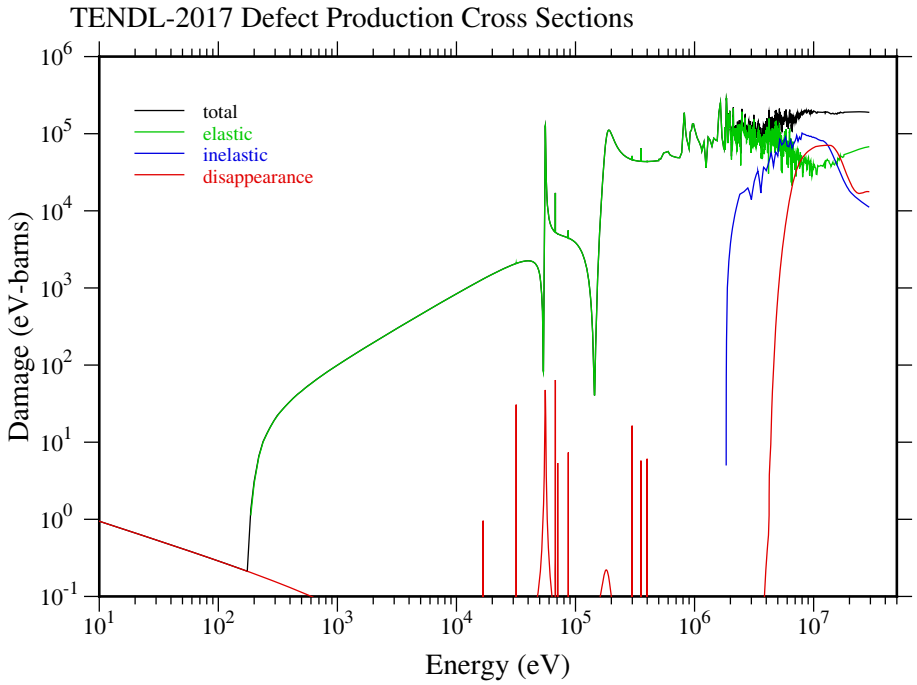

Fig. 22. Example of the damage energy cross-sections for ^{28}Si from the TENDL-2017 library.

Such dpcs are obtained from nuclear data libraries [43], which include evaluations (or recommendations) for single isotopes and their different cross-sections (elastic, inelastic and others).

In this work, an attempt is presented to quantify the impact of using natural (element) and oxide data in the nuclear data evaluation process on the dpcs, their uncertainties and cross-correlations. It will be shown that the elemental and oxide data experimental cross-sections (total and elastic) strongly influence the correlation matrix between isotopes, and reduce the dpcs uncertainties. This is of importance in the global characterization of uncertainties due to nuclear data and on their impact on simulation of damage metrics.

4.1.2 Methodology

In the following the proposed method is presented to include each type of experimental cross-sections (isotopic, natural and oxide) in the calculation of the defect production cross-sections (dpcs). Such cross-sections can be integrated in the evaluation process at different steps, each step leading to different dpcs and dpcs covariance matrices. Defect produced in particle-induced displacements events can include both isolated and clusters of vacancies and interstitials.

4.1.3 Defect production cross-section

From the nuclear data point of view, there are a few possibilities to calculate the defect production cross-sections starting from nuclear data libraries, as it was outlined during the IAEA Coordinated Research Project on Primary Radiation Damage Cross-Sections [68]. In the present work, the NRT method from the NJOY processing code is used [43]. It should be noted that the present method is independent of the definition of the dpcs, or of the quantity calculated for radiation damage. A similar approach can be followed in the case of the calculation of "primary knock-on atom" recoil spectra, as long as such calculation is based on so-called nuclear data as included in nuclear data libraries.

The dpcs are then derived from the nuclear data evaluation using NJOY, as presented in fig. 22 in the case of ^{28}Si. More specifically, the HEATR module of NJOY is used to extract the quantity referred as 444, being the total damage energy cross-section (eV barns). In the following, any dpcs values for different isotopes are obtained as explained.

4.1.4 Isotopic nuclear data

In the process of creating a general-purpose nuclear data library, only a selection of experimental data are considered. Such data naturally include isotopic cross-sections, such as the total, elastic, capture cross-sections (and other partial cross-sections) if they are considered of good quality. The isotopic cross-sections are in principle exempted of the effects

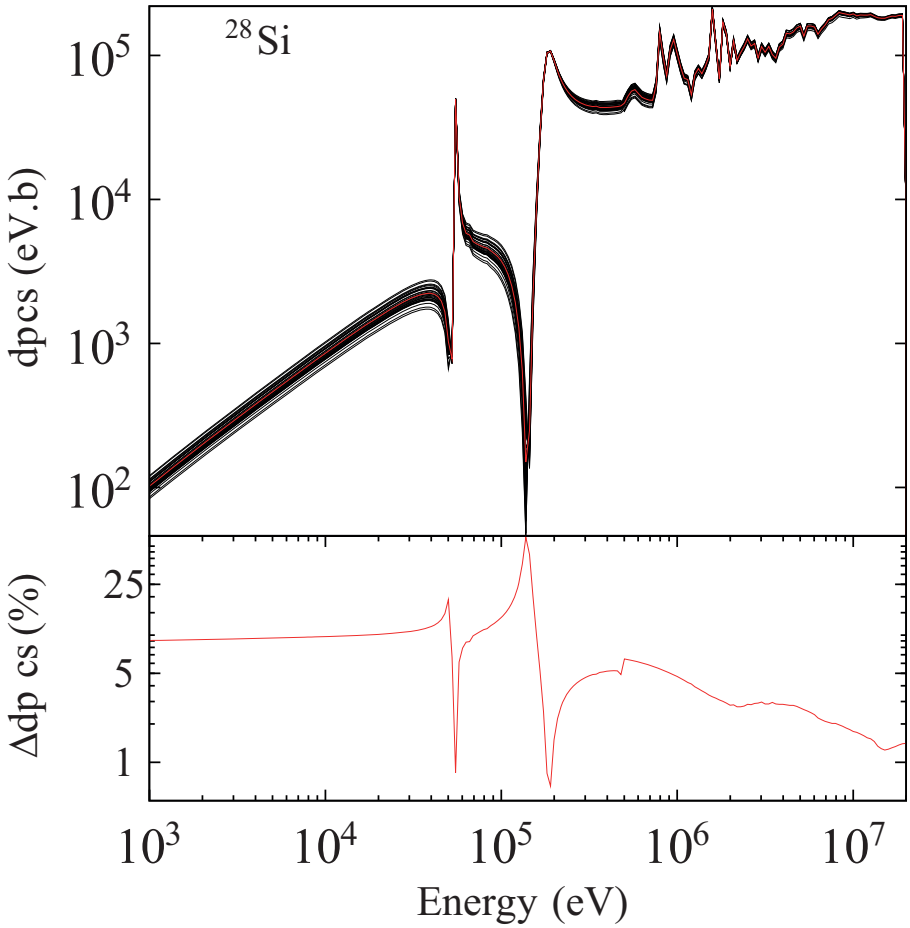

Fig. 23. Example of the random damage energy cross-sections for ^{28}Si from the TENDL-2017 library and their uncertainties. Only a subset of 30 random dpcs are plotted.

of other isotopes, as the targets used during the measurements are as pure as possible. Other experimental data, such as on natural targets are in general not considered during the isotopic evaluations, but can be used afterwards for checking purposes. The main reason is to avoid compensation between different isotopes of the same element, and the same reason applies for oxide data which also involves the oxygen cross-sections. This way, only isotopic cross-sections explicitly enter in the evaluation process.

Based on these isotopic cross-sections as presented in the EXFOR database [69], nuclear data evaluators adjust model calculations in order to obtain reasonable C/E ratios (C: calculation; E: experiment), ensuring a good reproduction of the measurements, as well as sound estimations for the quantities without experimental data. Once this time-consuming effort is achieved, the calculated cross-sections (or more generally nuclear data) are stored in an evaluated file. The most common format for such file is the ENDF-6 format, which can for instance be processed by NJOY to calculate derived quantities such as the dpcs. It is nevertheless important to notice that this process produces adjusted model parameters, which depend on the considered experimental data and also on the considered models. Such cross-sections, evaluated file and model parameters can be seen as best estimate values, or also nominal values.

In some cases, an additional step is performed and consists in calculating so-called "random evaluations" based on the variations of the nominal model parameters. This is for instance the case for the TENDL evaluations [38]. Model parameters can be randomly varied to produce random cross-sections, which in turn can be formatted in random ENDF files, and in covariance matrices. Different methods allow to vary model parameters, such as the Total Monte Carlo method [70], or the Bayesian Monte Carlo (also called Backward-Forward Monte Carlo) method, as described in refs. [71,72,37]. In the Bayesian Monte Carlo (BMC) method, each random cross-section is compared to the experimental data and a weight is assigned to the specific set of model parameters: if the agreement is good, the weight is high, if not the weight is low. Such approach allows to calculate posterior parameter distributions which take into account a specific set of experimental data for isotopic targets. Once this posterior distributions are calculated, one can sample again from them and obtain posterior random cross-sections and covariance information. This is the way the TENDL evaluations are performed. As an illustration, the dpcs for ^{28}Si from the TENDL-2017 library are presented in fig. 23. Two quantities are presented: the random dpcs and their uncertainties, using a set of 1000 random files.

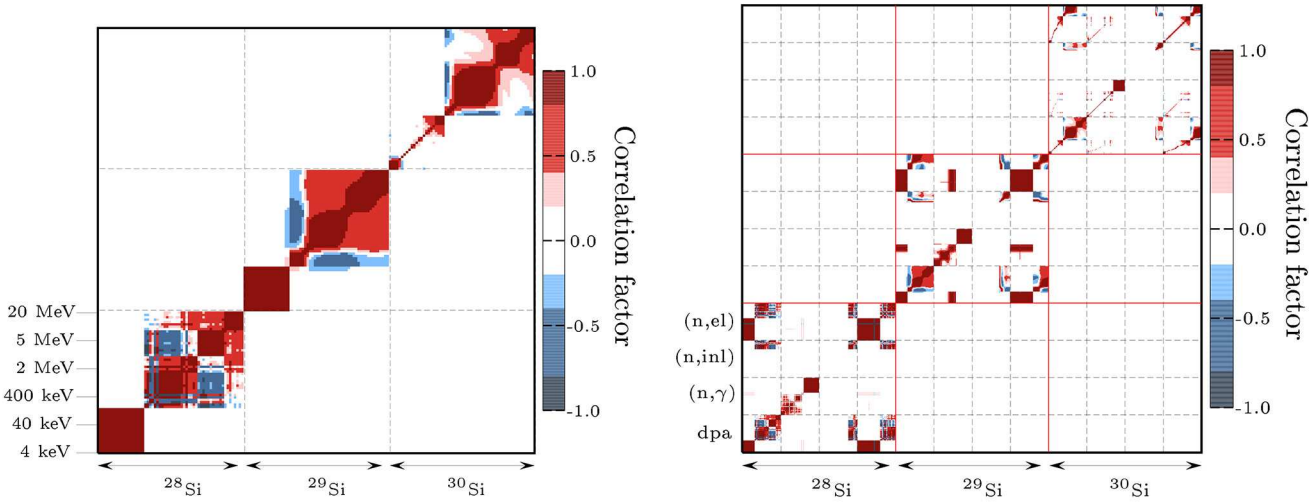

Fig. 24. Example of correlations for the dpcs for the three silicon stable isotopes (left) and for different cross-sections for the same isotopes (right). No correlations between isotopes appear as indicated in the text.

From the described method, it can be stated that the calculated uncertainties are mathematically derived from the comparison with isotopic data. Of course these values also reflect the assumptions used in these calculations: the NRT method, the nuclear reaction models (not always able to reproduce well enough the experimental data), and the weight definition. As an example of approximation, the definition of the weight is taken as

$$\chi_i^2 = \left(\frac{\sigma_i - \sigma_{\text{exp}}}{\Delta\sigma_{\text{exp}}}\right)^2, \tag{27}$$

$$w_i = \exp\left(-\frac{\chi_i^2}{2}\right), \tag{28}$$

for a comparison between the calculated cross-section σ_i (from the run i) and the experimental cross-section σ_{exp} (with an uncertainty of $\Delta\sigma_{\text{exp}}$). In the case of many experimental data, eq. (27) is replaced by a simple sum of partial χ_i^2 for each experimental value. This is the definition of a simplified χ^2, without considering correlation terms between experimental points.

As a consequence of choosing isotopic experimental data for the evaluation work, there is no correlation between isotopes coming from experimental observations. There are nevertheless theoretical correlations between isotopes because of the use of the same reaction models. Such correlations can be observed when generating random nuclear data between two isotopes only if the same random numbers are used for similar iteration cases. If the seed of the random number generator is changed from one isotope to the other, such model-based correlations will not appear. On the contrary, model-based correlations from one incident neutron energy to the other are easily observed for a specific isotopes, using random nuclear data generated with the TMC or BMC methods.

As an example, the correlation matrices for the dpcs of the three isotopes of silicon are presented in fig. 24, generated using 1000 random files from the TENDL-2017 library (from the BMC method). As observed in the case of the dpcs (fig. 24 left) only energy-energy correlations for a single isotope exist, due to the structure of the diffusion and capture cross-sections used with the NRT method. In the example of different cross-sections (fig. 24 right), still no correlations between isotopes are observed, but the cross-reaction correlations for a single isotope are observed. This example for silicon isotopes is representative of the content of existing libraries, if they are accompanied with random cases. In the cases of the presence of covariance matrices in libraries (instead of random files), the same observation can be done.

From a nuclear data evaluation point of view, such situation might not be satisfactory. As mentioned, other quantities are experimentally known and can bring specific constraints to cross-sections, models and their parameters. An example of such constraints can be found in refs. [73,74] where integral experiments are used to obtain posterior distributions for cross-sections and covariance matrices. Following the same approach, one can update in a Bayesian definition the isotopic evaluations with experimental data related to natural element and oxide compound. In the following, selected measured total cross-section for $^{\text{nat}}$Si and SiO_2 will be used in that purpose.

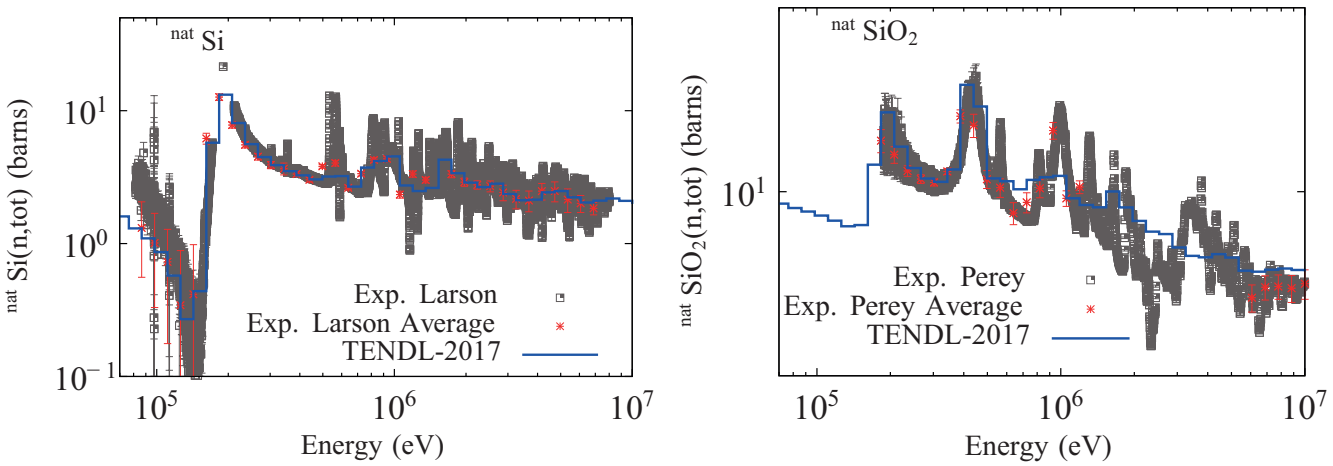

Fig. 25. Example of additional experimental data for the natural (left) and oxide (right) compound of Si.

4.1.5 Natural and oxide nuclear data

As mentioned, experimental measurements involving more than one isotope are usually not directly considered in the evaluation work. As a consequence, derived quantities (such as dpcs) calculated based on the nuclear data library might not represent the best state of the current knowledge. A convenient solution to this dilemma is to include such multi-isotope measurements in a second step, the first step being described in the previous section. To succeed, the same preliminary in-depth evaluation work is necessary: an appropriate selection of measurements and analysis of uncertainties. In the following, only a limited set of measured total cross-sections for $^{\mathrm{nat}}$Si and SiO_2 above the 4 keV will be used, extracted from the EXFOR database. Such experimental data will then be compared to the calculated natural and compound cross-sections (being simply the weighted sum based on the natural abundance) by the means of eqs. (27) and (28). Three different experimental data set are considered for the total and elastic cross-sections: the measurements from Larson for $^{\mathrm{nat}}\mathrm{Si}(\mathrm{n},\mathrm{tot})$ [75], from Kinney for $^{\mathrm{nat}}\mathrm{Si}(\mathrm{n},\mathrm{el})$ [76], and from Perey for $SiO_2(\mathrm{n},\mathrm{tot})$ [77], see fig. 25 for a selection of these experimental data. In this figure, the calculated cross-sections are also compared with the measurements, showing partial agreement, one because of the limit of the evaluation, and two because of the fine energy structure of the measurements compared to the coarse grid of the calculations. Therefore the experimental data are first average on the same energy grid as the calculations. A simple average for the cross-section is performed, as well as for the uncertainties, implying full experimental correlation within the energy groups. This is a simplified approach, having no consequences on the presented method, but results will certainly differ if a correct averaging, taking into account the experimental details, is performed. Such average experimental data are also presented in fig. 25 and will be used in eqs. (27) and (28).

Starting from the 1000 random files mentioned in the previous section for each of the silicon isotopes, a thousand weights w_i are calculated for each triplets of random files $(0_{\mathrm{Si28}}, 0_{\mathrm{Si29}}, 0_{\mathrm{Si30}}), \ldots, (i_{\mathrm{Si28}}, i_{\mathrm{Si29}}, i_{\mathrm{Si30}})$. For the time being, a unique ^{16}O total cross-section is used. If the combination i of the random files is in good agreement with the experimental data, the weight w_i will be relatively high, on the contrary, a low weight indicates a limited agreement. As presented in ref. [74], the number of weights having high values needs to be enough to ensure convergence of the posterior quantities (for updated cross-sections, uncertainties and correlations, see the definitions of weighted average and weighted covariances are presented in ref. [73]). In the present case, about 40% of the weights are higher than 10^{-5}, which is more than compared to ref. [74] and is enough to reach an acceptable convergence.

Using such new weights which reflect the natural and oxide experimental data, it is possible to update the dpcs (and other cross-sections) and their covariances, see fig. 26. As in the case of refs. [73,74], weak to relatively strong correlations arise from the use of experimental data involving many isotopes. For the dpcs, the correlations between isotopes come from the correlations between the elastic, inelastic and capture cross-sections for the three considered isotopes. Together with the correlations, the dpcs and dpcs uncertainties also changed, as presented in fig. 27 for ^{29}Si. As observed, the changes for the dpcs are moderate, although they are stronger for ^{28}Si. It can be observed that the addition of information does not automatically result in a decrease of uncertainties for all isotopes, as seen for ^{29}Si above 1 MeV have increased.

4.1.6 Discussion

All together, considering the posterior cross-sections and covariances, the calculations of DPCS, DPA, PKA, or any other quantities based on nuclear data will be modified, most likely with a global uncertainty reduction, based on

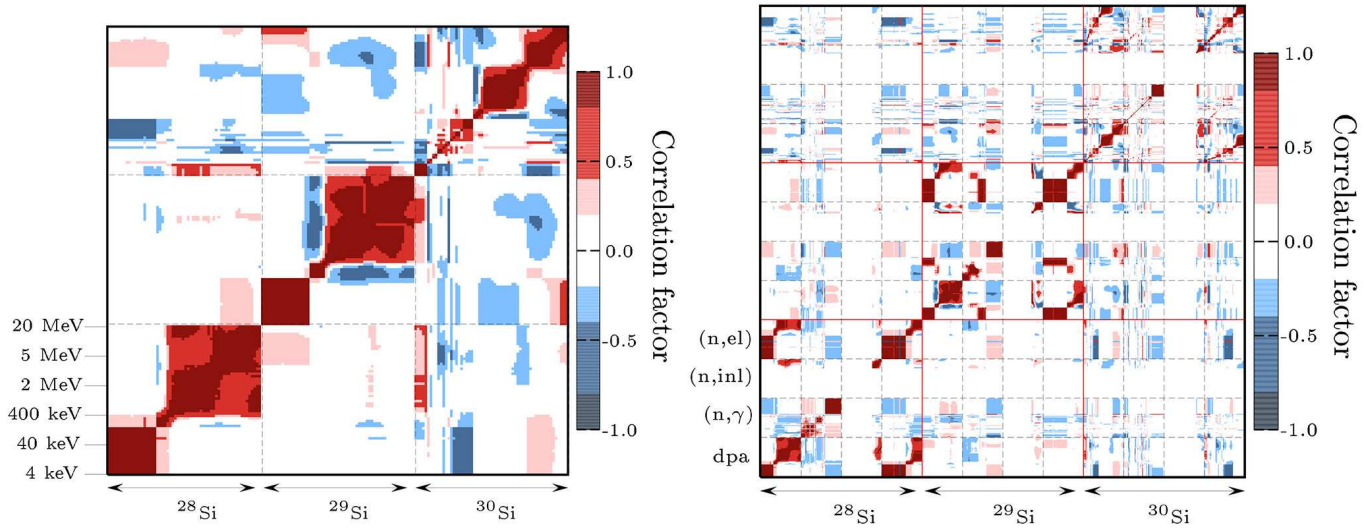

Fig. 26. As fig. 24, but taking into account the natural and oxide experimental data.

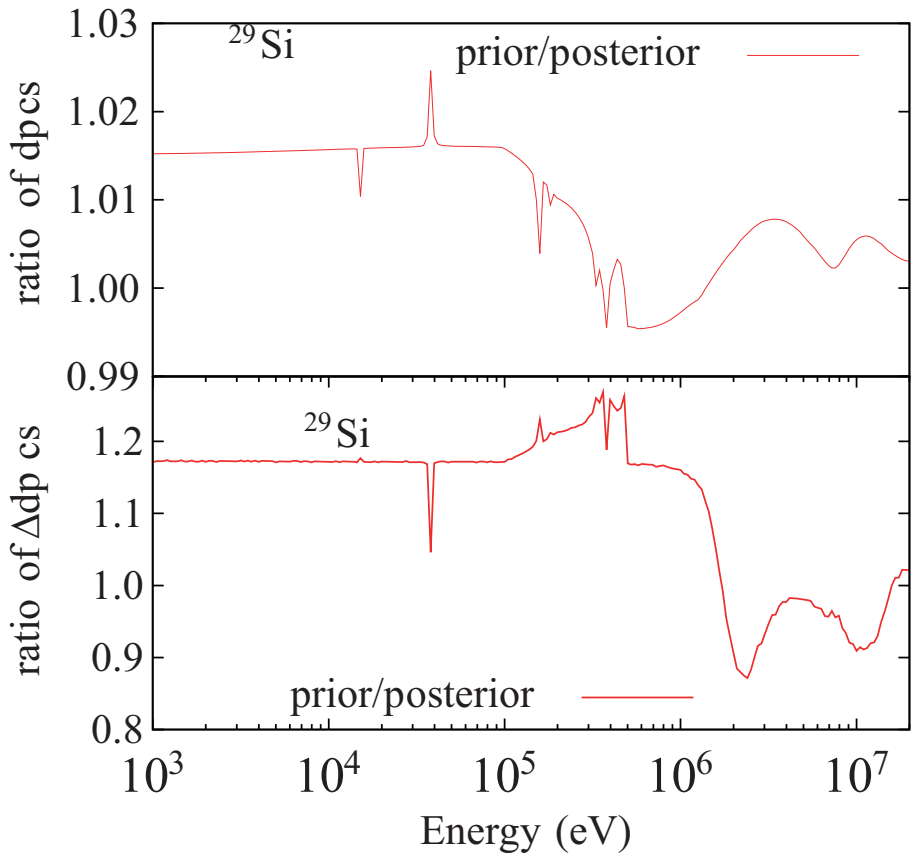

Fig. 27. Ratios of prior over posterior dpcs and dpcs uncertainties for ^{29}Si, taking into account the ^{nat}Si and SiO_2 experimental data.

well-explained mathematical procedures and explicitly included experimental data. Ultimately, such approach can be applied to all isotopes of interest for a material of importance in a specific application, or simply to all the isotopes of a given library, considering an external set of experimental data exits for those. Such data can be differential, as presented here, but also integral (such as shielding benchmarks) as long as a it is possible to compare calculated and measured quantities.

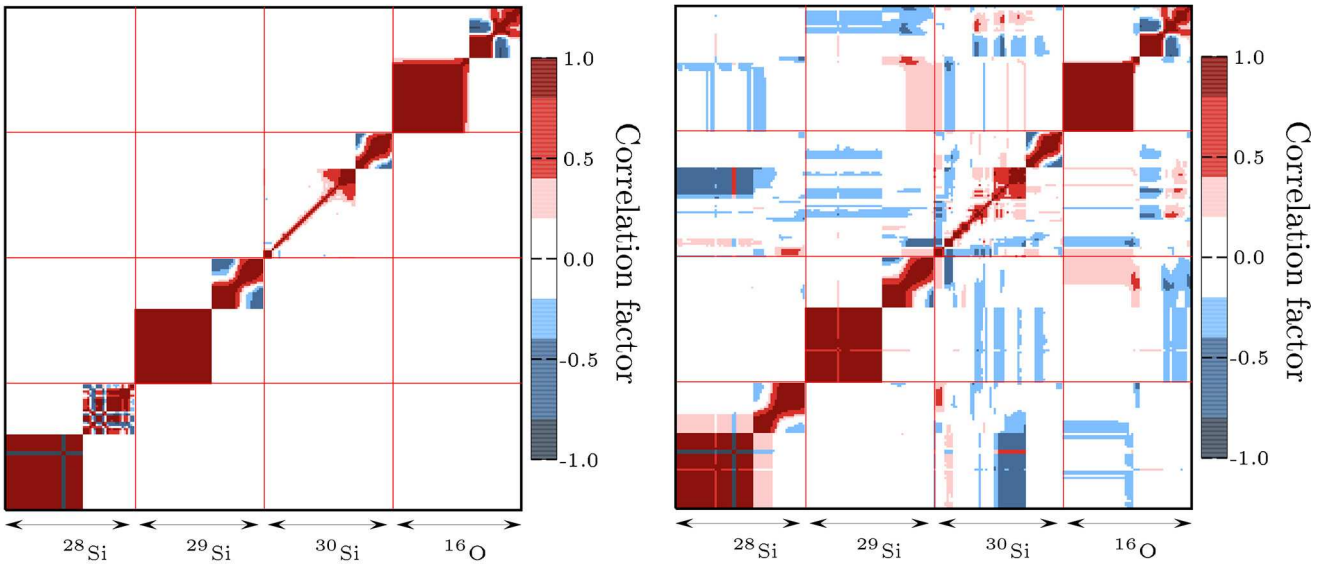

Fig. 28. Example of correlations between the silicon isotopes and ^{16}O for the total cross-section. Left: without the SiO_2(n, tot) cross-sections. Right: with SiO_2(n, tot) cross-sections.

It can be argued that such posterior evaluations do not belong to a general purpose library and should therefore be separated from it. This depends on the type of additional data used: if only differential cross-sections for natural targets are used, then they are as relevant as isotopic data and should not be excluded. If differential cross-sections from a compound target is used, such as oxide, it is clear that the posterior evaluations are dependent on other nuclear data such as from oxygen. But this is not a justification for not including such posterior in a general purpose library. The final discussion point concerns the use of integral data. In this case, no general rule can be established, as such data can involve a single isotope, more isotopes, or complicated simulation procedures. A selection will have to be made on the types of measurements, and if they are considered clean of potential compensation sources, then posterior cross-sections and covariance matrices can be included in a general purpose library.

Finally, it was mentioned earlier that the comparison between the Si isotopic calculated cross-sections and the measured SiO_2 data requires the use of the oxygen cross-section (as presented in fig. 25). Such cross-section can be considered fixed as performed above, but it can also be considered varying with the use of random files, as for the silicon evaluations. In this case, the Bayesian procedure will allow to access correlations between silicon and oxygen, as well as to update the cross-sections themselves. By using a set of 1000 random oxygen evaluations, correlations for the total cross-sections between the silicon isotopes and ^{16}O are presented in fig. 28. If generalized, it can be observed that a large number of isotopic evaluations can be correlated with each other, due to specific experimental data, or due to normalization factors through flux monitors. Therefore, not including such correlations can limit the range of applicability of a general purpose library as such nuclear data evaluations only partially represent considered measurements.

The impact of considering elemental and oxide model and experimental constrains in the evaluation of the isotopic silicon defect metrics is of interest. It was observed that by using such experimental information, non-negligible cross-isotope correlations are obtained, leading to a reduction of uncertainties. Additionally, correlations between the silicon isotopes and oxygen-16 are obtained. These observations are of importance in the context of uncertainty quantifications on crystalline defect metrics, due to nuclear reaction quantities such as differential cross-sections. It is therefore recommended to include such experimental information in the nuclear data evaluation process, and to consider the cross-isotope correlations for the uncertainty propagation.

4.2 Uncertainty quantification in damage metrics

This section describes an evaluation of the covariance matrices for damage metrics *NRT*- and *arc*-dpa cross-sections, *i.e.* the uncertainties and associated energy-energy correlations resulting from the involved nuclear data and material physics modelling. This is illustrated for the naturally occurring isotopes and elemental iron based on the latest evaluated neutron cross-section data files up to 30 MeV [78,79].

At the end the comparison of *NRT*-dpa with ASTM standard and of *arc*-dpa with known measurements are given. Previously the comparative studies of the *NRT*- and *arc*-dpa cross-sections and spectrum averaged values for fission, fusion and material testing facilities were carried out [80,81], but for neutron energies below 20 MeV and using the neutron data available at that time.

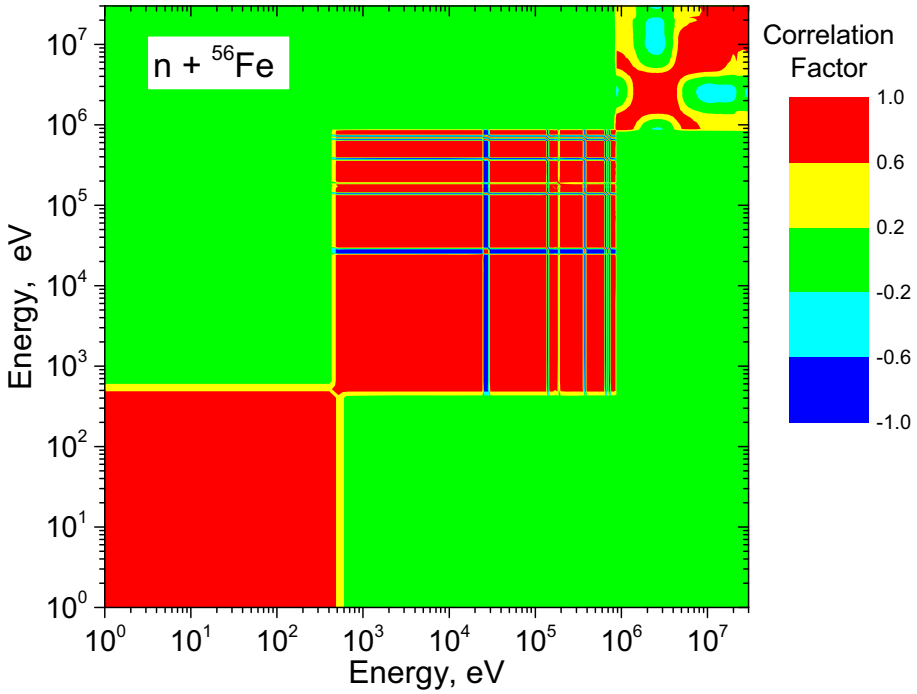

Fig. 29. The energy-energy correlation matrix for the *NRT* damage energy derived from TENDL-2017 random files for iron isotope ^{56}Fe.

4.2.1 Damage cross-section covariances due to nuclear data

The radiation damage quantities for each stable iron isotope ^{54,56,57,58}Fe were processed by code NJOY-2012 [43] from the modern nuclear data evaluations ENDF/B-VIII.0 [54] and TENDL-2017 [53]. The HEATR module of NJOY was modified to implement the *NRT* model following eqs. (1) and (2) and the *arc* formulation presented in sect. 5. The displacement damage energy E_{dam} and *dpa* cross-sections for natural iron were then computed from isotopic cross-sections by the MIXR module of NJOY regarding the isotope abundances.

The covariance matrix for the damage quantities were computed from TENDL-2017 random files generated by the Bayesian Monte Carlo method [38]. The procedure first includes the NJOY processing of 500 TENDL-2017 random files for each isotope and computing of the energy-energy covariance matrices. Then the covariance matrix for natural iron was obtained by summing up the variances of the individual isotopes with the iron isotope abundances supposing no cross-isotope correlations between them. The cross-sections and covariances were additionally grouped to reduce the rank of matrices but still keeping detailed energy representation.

As an example the energy-energy correlation matrix for the *NRT* damage displacement energy for isotope ^{56}Fe is displayed in fig. 29. Two energy domains of high correlations inside are seen however without correlation between them.

4.2.2 Covariances due to materials physics modelling

Besides the nuclear reaction cross-section several other input data which reflect the material physics phenomena have impact on the calculation of the damage quantities.

Partitioning of the primary recoil atom energy between the energy delivered to the lattice knock-on atoms and lost in interaction with electrons was formulated by Robinson [18]. The uncertainties of the Robinson formula parameters, eqs. (14)–(17), were found from the comparison with the *NRT* defects spread computed by the IOTA code [82]. For this the different approximations of the ion-ion scattering cross-section were used. Then we varied the partition function parameters within found ±12% during processing of the non-perturbed TENDL-2017 files by NJOY. Finally the statistical analysis of generated random damage energy cross-sections produced the covariance matrices for each Fe isotope. Their mixing yields the damage energy correlation matrix caused by the damage energy partitioning for natural iron, fig. 30. One may observe the strong correlations between all neutron energies.

The athermal recombination-corrected displacement cross-section *arc*-dpa [83,84] predicts the total number of Frenkel pairs (FP) left after relaxation of the energetically dense recoil cascades. The proper defect survival efficiency,

$$\nu(T) = FP/NRT, \tag{29}$$

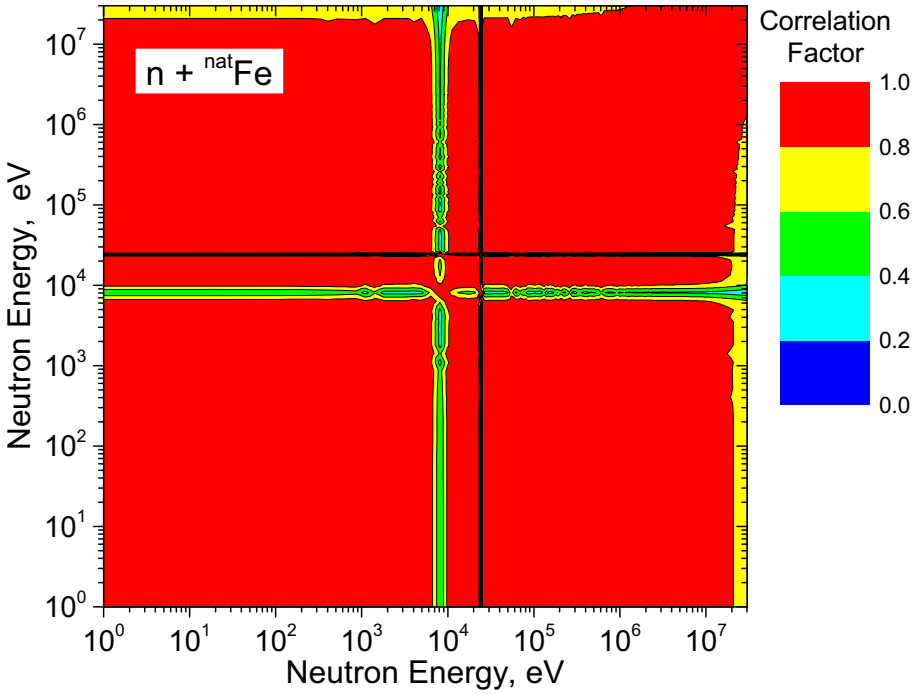

Fig. 30. The energy-energy correlation matrix for the NRT damage energy resulting from the variation of parameters of the ions energy partition function for natural Fe.

depends on the energy of primary recoil and affects only *arc*-dpa, but not *NRT*-dpa. As discussed in sect. 5, the number of FP defects is computed by molecular dynamics (MD) or binary collision approximation (BCA) which depend on the interatomic potential and other parameters. The choice of potential and insufficient statistical uncertainty caused by a limited number of simulated tracks result in the variation of the predicted defect survival efficiency.

The known MD simulations for iron, see overviews [84] and [79], provide defect survival efficincy for the PKA energy up to $\approx$ 200 keV. To cover the energy range of recoils produced in fusion and accelerator driven facilities (*e.g.*, International Fusion Material Irradiation Facility), the survival efficiency has to be defined up to 1000 keV and 3800 keV, correspondingly. For the computing the number of FP at such high recoil energies, the binary collision approach (BCA) or its combination with MD simulations [82,85] could be used.

Figure 31 shows the known MD and BCA results. In the present calculations we used the defect survival efficiency from fit [84] up to 200 keV and at higher energies the SRIM-based MD-BCA results from [82] scaled by the factor 0.8 to match the fit. The uncertainties assessed in [84] amount only to $\pm$(2–4)% that do not reflect the spread of the MD simulations as seen in fig. 31. To capture real scattering we assumed $\pm$20% uncertainty for the defect survival efficiency.

The recoil energy-energy correlations for the damage efficiency is a result of the underlaying MD and BCA models and the statistical uncertainty of numerical simulations. The statistical uncertainties, if they are reported, are within (10–20)% for PKA energies below $\approx$ 40 keV [83,86]. These values are comparable with spread of individual results as seen in fig. 31. Such dominance of the statistical uncertainty means an absence of the energy-energy correlation. Since no more information is available we supposed non-correlation for the defect survival efficiency in the whole energy range of PKA.

The energy-energy correlation matrix for the *arc* damage energy for elemental iron resulting from the uncertainties of the FP survival efficiency is plotted in fig. 32. As expected we observe no correlation except the neutron energies below $\approx$ 0.5 keV, where the dominant (n,γ) reaction produce recoils with energy independent of the incident neutron energy that results to 100% correlation.

Regarding the uncertainty of the lattice threshold energy E_d. For iron the average value and uncertainty was estimated as (40 ± 2) eV in [87]. The new simulations predict the average value about 20% lower than the accepted standard value 40 eV [88]. Such (5–20)% uncertainty will directly propagate to the *NRT*- and *arc*-dpa and will imply a 100% correlation for all considered neutron energies. Additionally the E_d uncertainty will affect the damage energy via the lowest energy integration limit of PKA, see eq. (3). However this lattice threshold effect will reveal itself only at the neutron energies from 0.5 to 1.0 keV.

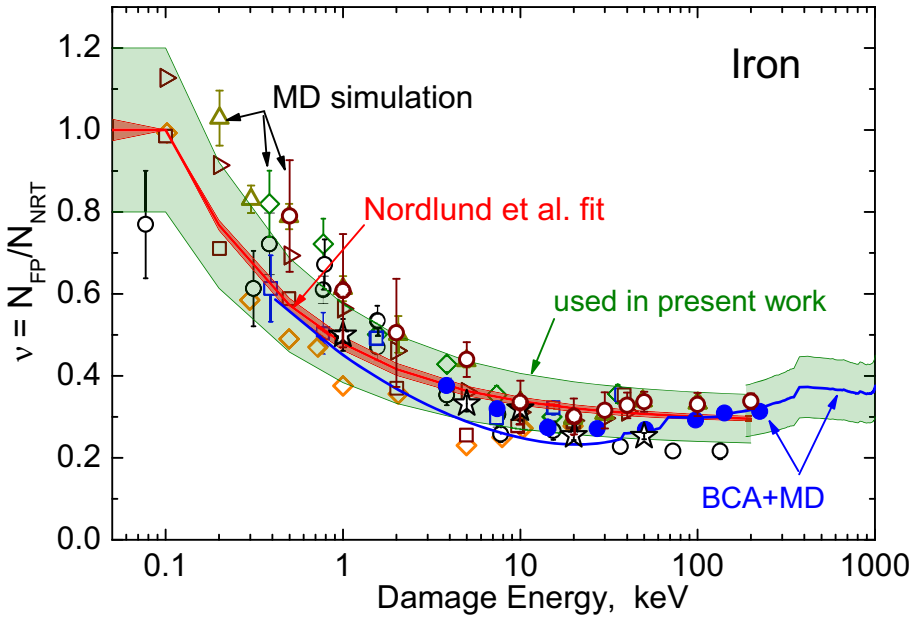

Fig. 31. Dependence of the primary defects survival efficiency on recoil damage energy in pure iron. Open symbols: known MD simulations (for details see ref. [79]); closed and blue curve: combination of BCA and MD from [82,85]; red curve: fit [84]; green curve with ±20% uncertainty: used in the present arc-dpa calculations.

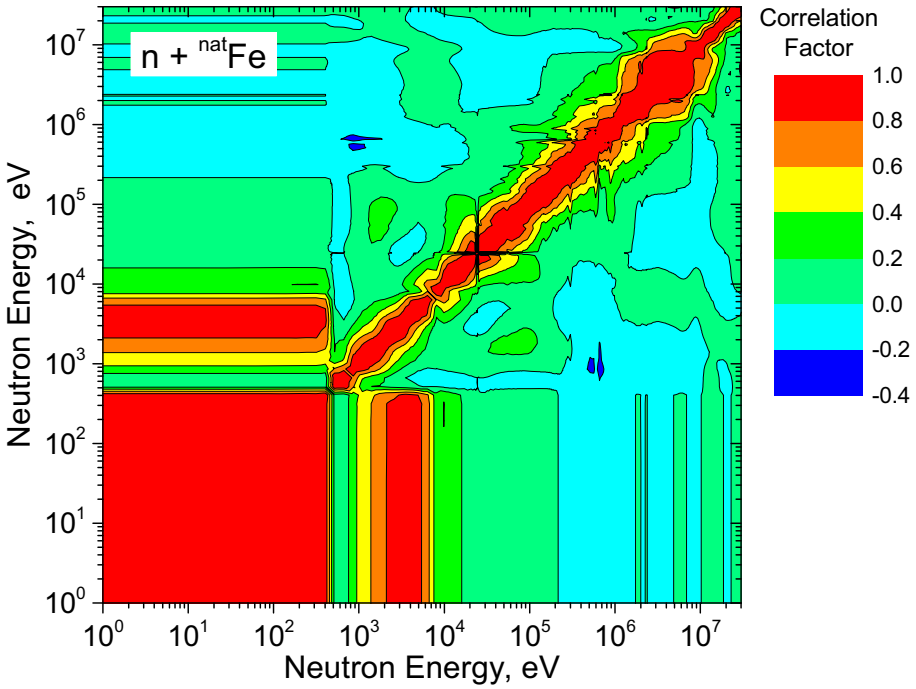

Fig. 32. The energy-energy correlation matrix for *arc* damage energy in Fe due to the uncertainties of the FP survival efficiency.

4.2.3 Comparison with Fe ASTM standard and measurements

The *NRT*-dpa cross-section for natural iron up to 30 MeV, derived from the latest version of ENDF/B-VIII.0, and the *arc*-dpa cross-section, which takes into account the Frenkel pair survival efficiency, are shown in fig. 33. As can be seen, the *arc*-dpa cross-section is less than the *NRT*-dpa by factor 2–3 except for the neutron energies from 0.6 keV to 2–3 keV. The latter interval corresponds to PKA recoils where the FP survival efficiency is close to unity, fig. 31.

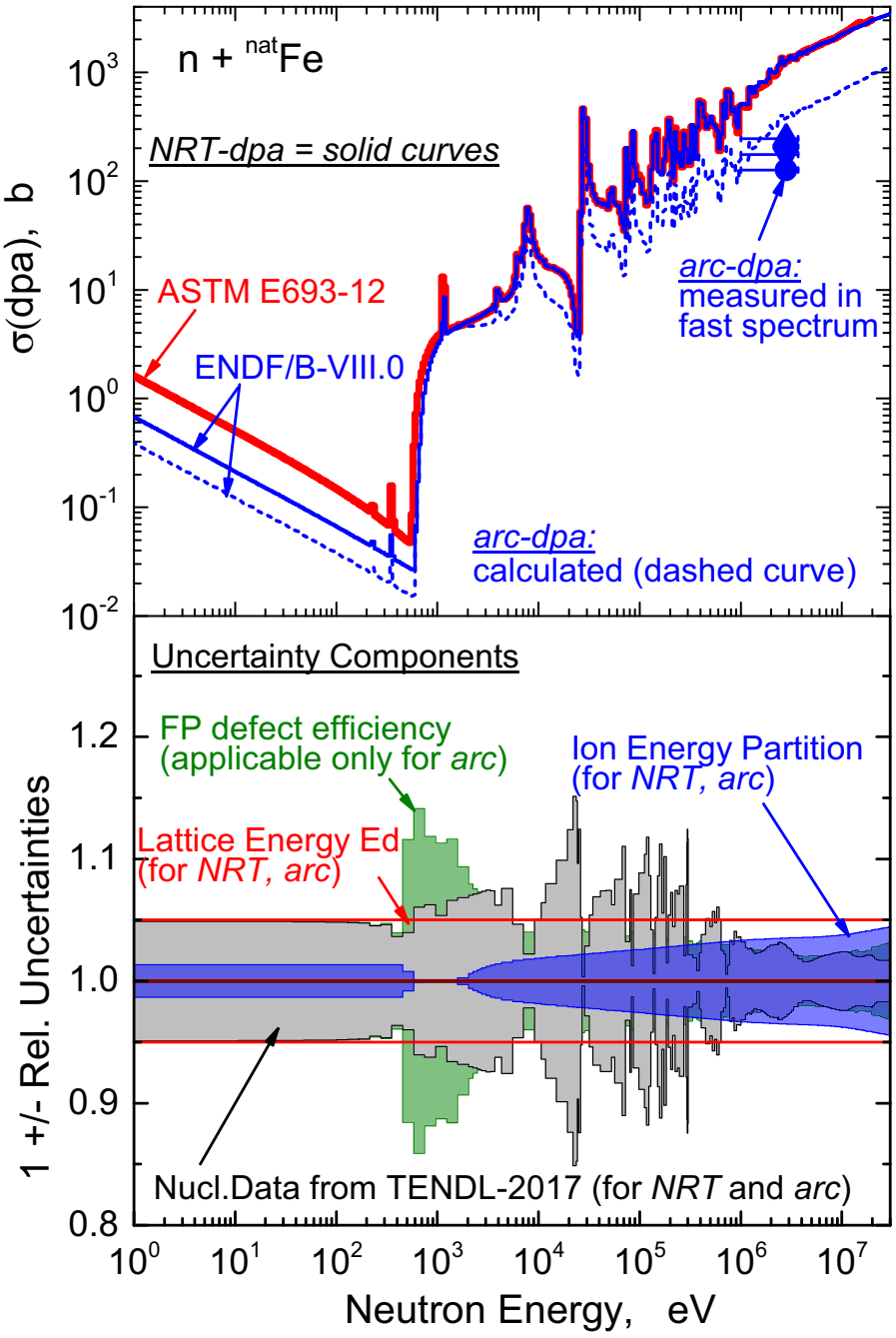

Fig. 33. The *NRT*- and *arc*-dpa cross-sections (top) and uncertainty (bottom) with contribution from nuclear data, ion energy partition, FP defect surviving efficiency and lattice threshold for natural iron. The actual ASTM E693 *NRT*-dpa standard for iron is plotted for comparison.

The bottom of fig. 33 shows the uncertainty components: the nuclear data lead to (5–10)% uncertainties; ion energy partition function to (2–5)%; defect survival efficiency to (5–15)%; lattice threshold to 5% or larger uncertainty. The corresponding energy-energy correlation matrices are shown in figs. 29, 30 and 32. The total covariances for *NRT*- and *arc*-dpa could be obtained by summing the partial components.

The actual *NRT-dpa* reference for iron up to 20 MeV neutron energy, the ASTM E693-12 standard [89] derived from the evaluated neutron cross-sections library ENDF/B-VI.1-5, is also shown in fig. 33. It is seen that ASTM standard is 2 times higher below neutron energy 0.5 keV and deviates up to 8% at higher energies. The rather large difference at lowest energies is not a result of the change of the Fe(n,γ) cross-section, but comes from the damage energy computed by NJOY. However the neutrons with energies less than 100 keV is known do not significantly contribute to the total dpa fluence in various application.

The *NRT*-dpa cross-section, as practically a non-observable physical quantity, cannot be compared with experimental data and thus be validated. However the *arc*-dpa can be obtained from the measurements if the samples are irradiated at temperature below 10°K that prevents the diffusion and annealing of primarily created Frenkel pairs. Such experiments were carried in fast fission neutron spectra [90–92]. The number of created primary defects was derived from the change of electrical resistivity. To perform a comparison we have folded our computed *arc*-dpa cross-section with the prompt fission neutron spectrum from the thermal neutron fission of ^{235}U [93]. The comparison in fig. 33 and of numerical data show reasonable agreement of *arc*-dpa with two of three existing experiments. The spectrum weighted *NRT*-dpa is approximately 3 times larger than *arc*-dpa. For more details relevant to results presented in this subsection see [79].

5 Alternatives to DPA

5.1 Molecular dynamics

5.1.1 Background and computational details

Generally, there are three distinct stages in cascade development [86]. During the first stage of about 0.1–0.5 ps, the PKA transfers the kinetic energy to surrounding atoms by multiple collisions. The excited atoms leave their lattice sites and move away from the cascade origin; as a result a depleted zone is created and a fraction of atoms is ejected outwards. It is particularly remarkable that the subsequent formation of vacancy loops is often initiated by the hypersonic recoil process in less than 0.1 ps from the onset of primary recoil [94]. The following thermal-spike stage is characterized by some local equilibrium in the exited area, which appears extremely spatially inhomogeneous in terms of temperature, density and pressure. During several picoseconds, most of the excited atoms return to the regular lattice sites; the temperature peak spreads. By this time the formation of stable vacancies, self-interstitial atoms (SIAs) and their clusters takes place. The central part of the cascade region appears to be enriched by vacancies while SIAs reside mainly at the periphery. It is precisely due to the spatial separation of point defects, that their full annihilation does not occur afterward. The two initial short-term stages comprise primary damage formation. The third kinetic stage includes diffusional redistribution and recombination of the formed defects.

The NRT approximation [1] estimates the number of formed primary defects. To describe the kinetic stage, it is necessary to know the number of surviving point defects after they have dispersed over sufficiently large distances. If we assume that initially the primary single vacancies and SIAs were uniformly distributed in a certain spherical region of the crystal, they would fully recombine with time. Therefore, the initial distribution of primary defects is essential to describe the complete evolution of radiation damage. Primary damage occurs on the length and time scales that are well suited for the application of the molecular dynamics (MD) simulation technique.

Below we present several examples of the simulation of primary damage in pure defect-free crystals to demonstrate material phenomena beyond the NRT approximation. Significantly more distinct phenomena are observed near extended defects, such as grain boundaries [95], external surface [96,97], voids [98], gas bubbles [99], etc. In addition, some new results on cascade development in alloys and in the vicinity of dislocation loops and various precipitates are presented in the following section.

We shall provide information on the impact of collision cascades in the bcc Fe-Ni-Cu-Mn, Fe-Cr and W-Re systems. The latter represent, respectively, a model alloy for reactor pressure vessel (RPV) steels, ferritic martensitic (FM) steels and first wall fusion material, which due to the transmutation establishes a considerable concentration of Re under expected fusion operating conditions. The following four types of pre-existing defects were considered in the MD simulations: i) dislocation loops in pure Fe [100]; ii) solute-rich Ni-Mn-Cu clusters in RPV model alloys, mimicking so-called "late blooming phases" [101]; iii) coherent Cr precipitates, aka α' particles, in FM model alloys [102–104]; and iv) non-coherent Re precipitates in tungsten [105,106].

The cascade pre-existing defects were created, relaxed and thermalized following the knowledge available on their structure based on both experimental and computational studies. Interstitial dislocation loops were created in pure Fe, as these are the most typical defects appearing under irradiation already at an early stage, when the dose does not exceed 1 dpa (*e.g.*, [107]). The information on the Cr α' and Ni-Cu-Mn precipitates was obtained from the available experimental observations (*e.g.*, atom probe, transmission electron microscopy, ...) in the neutron irradiated steels [102–104]. Those precipitates are coherent with the bcc Fe matrix, and their typical size ranges from 0.5 nm to few nano-meters, while the density is within 20^{23}–20^{24} m^{-3}. Hence, the spacing between those particles is about 10–30 nm. The structure of Re precipitates observed under neutron irradiation has been reported in [105,106], following transmission electron microscopy studies of neutron irradiated pure tungsten. Since the actual crystallographic structure of Re precipitates eventually depends on the irradiation conditions, we modelled the interaction of cascades with the three most expected types: σ phase (W-50Re), χ (W-75Re) and pure hcp Re precipitates.

Besides the influence of features of the microstructure on cascade damage, the different swelling behavior of fcc, bcc, and hcp alloys under irradiation is still the issue to be resolved. The fcc alloys generally have the swelling rate

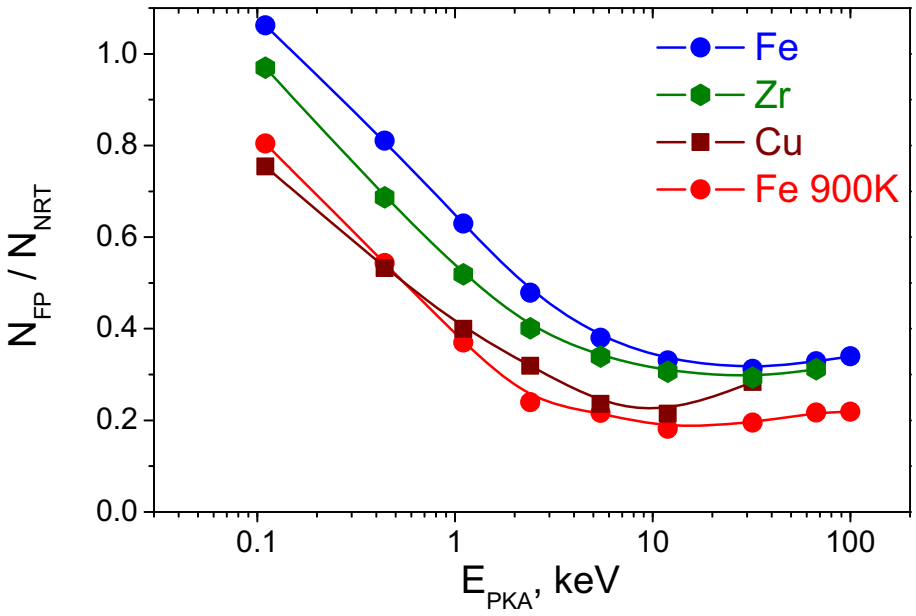

Fig. 34. Defect formation efficiencies as a function of PKA energy in Fe, Cu and Zr, at $T = 100\,\mathrm{K}$ (the upper three curves) and $T = 900\,\mathrm{K}$ (the lower curve). The lines are drawn to guide the eye only.

of about 1%/dpa in the steady state after an incubation dose. The bcc alloys are more swelling-resistant having a typical swelling rate of about 0.1–0.2%/dpa [108,109]. Alloys with the hcp lattice are found to be weakly susceptible to swelling. Most likely, differences in macroscopic behavior of crystals with different symmetries under irradiation can be attributed to the nature of defect recombination and the features of the microstructure evolution intrinsic to the crystal symmetry. The correlation properties of the formed radiation defects show that the distinctions are already observed during the primary defects formation. A possible reason for such behavior is the in-cascade point defect clustering. The comparison of cluster size distributions in metals possessing different symmetries has shown that the susceptibility of lattices to swelling correlates with the increase of the fraction of clustered SIAs [99]. Here we also consider the effect of the lattice symmetry for Zr which undergoes martensitic transformation in the appropriate temperature range.

Classical MD in NVE ensemble was employed with varying PKA energy in the range of 10–100 keV and simulation temperature in the range 300–600 K for the iron-based alloys and 873–1073 K for tungsten. Empirical potentials for Fe [110], Cu [111], Zr [112], Fe-Cr [113,114], Fe-Ni-Cu-Mn [115–117] and W-Re [118] were used for the simulations. All the potentials were smoothly fitted to the universal ZBL potential [119] at short distances in such a way [120, 121] as to get recommended threshold displacement energies. The electronic stopping obtained from SRIM [119] was included as a frictional force with a low-energy cutoff limit equal to twice cohesive energy [122]. An appropriate computational technique was employed to get sufficient accuracy and to speed up simulations [123]. Intermediate and final configurations of the formed vacancies and SIAs were analyzed by the Wigner-Seitz cell method, see details, *e.g.*, in [124]. A simple definition of a cluster is used. If two point defects are in the adjacent Wigner-Seitz cells, they are considered to be connected. A continuous chain of connected point defects forms a cluster.

5.1.2 Results and discussion

Figure 34 shows the ratio of the average number of Frenkel pairs to the NRT metric *vs* the PKA energy for simulated Fe (bcc), Cu (fcc), and α-Zr (hcp) lattices. At low energies, $E_{\mathrm{PKA}} < 0.1\,\mathrm{eV}$, the ratio $N_{\mathrm{FP}}/N_{\mathrm{NRT}}$ is close to unity. Then the efficiency of defect formation decreases logarithmically with increasing E_{PKA}, and reaches the minimum at the PKA energy about 10 keV. Subsequently it either remains unchanged or grows very slowly. A recent review of this behavior is presented in ref. [84]. The plots for Fe and α-Zr resemble each other closely, while for Cu the ratio $N_{\mathrm{FP}}/N_{\mathrm{NRT}}$ turned out to be somewhat smaller due to the fact that we used the value $E_d = 30\,\mathrm{eV}$ recommended for Cu, while the applied potential shows a higher value of this parameter. We can conclude that the lattice type has a weak effect on the total number of point defects generated in cascades.

The three upper curves in fig. 34 correspond to low-temperature data, $T = 100\,\mathrm{K}$. The lower curve for Fe shows the behavior at an elevated temperature, $T = 900\,\mathrm{K}$. The number of surviving defects is smaller by the factor of 1.6 in that case. This is due to in-cascade annealing during the first 100 ps. At high temperatures, the mobility of point defects is so high that not only nearby defects but more distant ones annihilate. As demonstrated by results of the

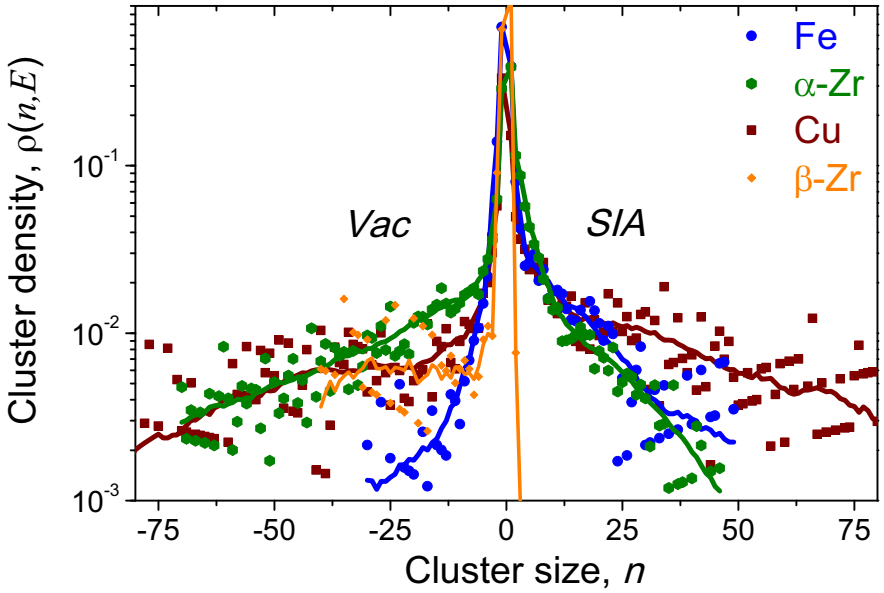

Fig. 35. Cluster size distributions in different lattices at elevated temperatures: Fe (900 K), Cu (600 K), α-Zr (1000 K), β-Zr (1100 K). The positive n are assigned to SIAs and negative n correspond to vacancies. The lines depict smoothed data calculated by the simple moving average method.

MC simulation [125], only about a half of the formed defects survive during the kinetic stage of cascade evolution. This should be taken into account when using the low-temperature results of MD simulation for the rate theory [126].

According to the conventional point of view, the point defects initially generated during the collision stage of the cascade are likely to be partitioned into three portions during the cooling down stage: those that recombine; those that cluster; and those that escape the cascade region and undergo long-range migration [127]. Clustered defects can significantly change the character of radiation damage accumulation. Generally, vacancy clusters appear in the form of immobile 3D voids, while small self-interstitial clusters are highly mobile and they migrate in an anisotropic, one-dimensional manner [128].

Let us denote by $P(n, E)$ the average number of clusters containing n point defects created in a cascade of energy E. The positive n are assigned to SIAs and negative n correspond to vacancies. We define the cluster size distribution as

$$\rho(n, E) = \frac{1}{N_{\mathrm{FP}}(E)} |n| P(n, E), \tag{30}$$

where N_{FP} is the average number of formed Frenkel pairs.

The distribution $\rho(n, E)$ is normalized so that the sum over all positive or negative n is equal to 1. In other words, $\rho(n, E)$ is the fraction of vacancies or SIAs found to be in clusters of size n. For instance, $\rho(-1, E)$ is the fraction of freely migrating single vacancies, whereas $1 - \rho(-1, E)$ is the fraction of clustered vacancies.

Figure 35 shows the simulated cluster size distributions. The data for high-temperature cascades with energies of 67 keV for Fe, 44 keV for Zr and 32 keV for Cu were used to demonstrate the scaling of size distributions. At lower energies, the shape of the distributions varies slightly. Within the limits of statistical errors, only the length of the tail of the distribution depends on the cascade energy, *i.e.* the approximate invariance of cluster size distributions with respect to the cascade damage energy is observed. As can be seen, the majority vacancies are clustered, and the fraction of single vacancies is only about 0.3 of the total number for Cu and α-Zr. The long distribution tails have power-law dependencies and extend to sizes greater than $n = 100$. Alternatively in iron, the fraction of single vacancies is somewhat higher, and the distribution of $\rho(n)$ decreases faster with increasing vacancy cluster size. The size distributions of SIA clusters are of the greatest interest. With the exception of β-Zr, all lattices exhibit wide size distributions of SIA clusters. The widest one is observed in Cu. As well as in W lattice [122], these distributions have power-law type of scaling. The existence of a large fraction of mobile SIA loops in the fcc lattice supports the idea of the effective separation of vacancy and SIA fluxes through the so-called production bias [127], which may explain the greater susceptibility to swelling of the fcc lattice as compared to the bcc lattice.

Focussing on the cases with different pre-existing microstructures, the main parameters of the primary damage, such as total number of Frenkel pairs, NRT efficiency and clustered fraction of point defects are summarized in fig. 36 for the Fe-based matrix. The figure caption explains the particular type of pre-existing microstructure.

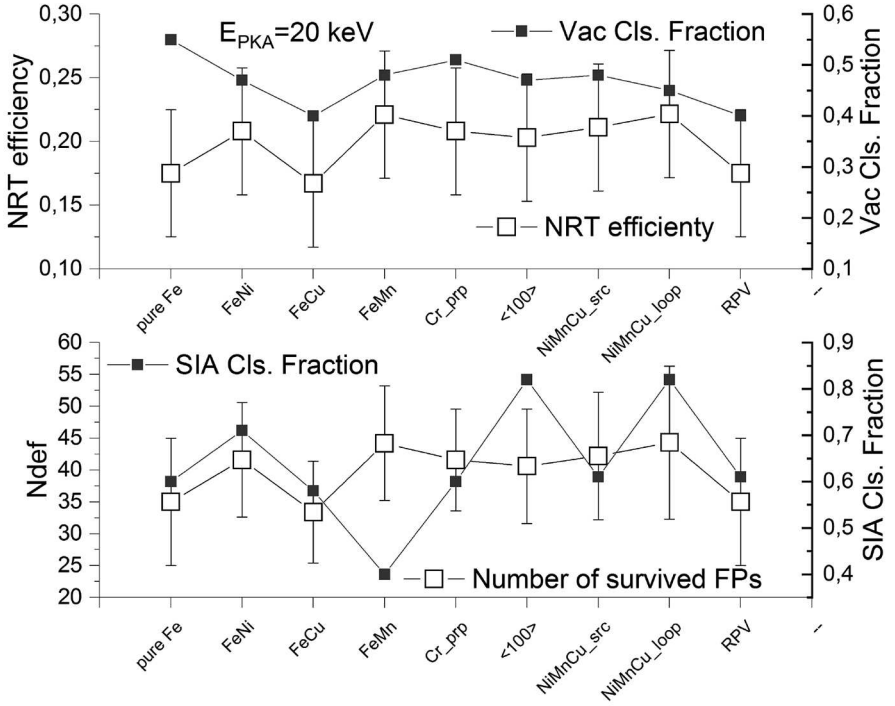

Fig. 36. Open symbols: NRT efficiency and total number of Frenkel pairs produced by 20 keV PKA cascades at 600 K depending on the type of the-existing microstructural defect. Filled symbols: Vacancy and SIA clustered fractions. The notations on the x-axis indicate the following. "pure Fe": bcc defect-free crystal of Fe. "Fe-Ni/Cu/Mn": Fe alloyed randomly by 1% of the respective element. "Cr_prp": α' precipitate of 2 nm. "$\langle 100\rangle$": 2 nm SIA loop. "NiMnCu_src": Mn-Ni-Cu solute rich cluster. "NiMnCu_loop": Mn-Ni-Cu decorated loop of 2 nm with $a_0\langle 100\rangle$ Burgers vector. "RPV": model alloy representing the composition of a typical RPV steel Fe-1.3Mn-0.7Ni-0.05Cu.

Let us first report the observations done for pure Fe with a pre-existing pattern of dislocation loops. Eight loops with Burgers vector $a_0\langle 100\rangle$ of 2 nm were placed in a $28\times 28\times 28\,\mathrm{nm}^3$ bcc simulation crystal. These loops are thermally stable and have a large migration energy (>1 eV), hence their thermal diffusion is not expected on MD time scale. As a result of the simulations of 20 and 100 keV cascades producing in total 100 cascades, it was revealed that the total number of newly created defects remains the same as in pure Fe, while the clustered fraction of vacancies is reduced to 0.3 (compared to 0.5 ± 0.1 measured in the defect free crystal). In addition, the fraction of the isolated SIAs was reduced to 0.15 (compared to 0.3 ± 0.05 measured in the defect free crystal), because many of the cascade-produced SIAs migrate to join the pre-existing loops. The impact of the cascade on the pre-existing loops has been noted in some cases but in 75% of the simulation runs, the pattern of loops remained the same as before the cascade. In 15% of the cases, some of the loops were seen to change their Burgers vector to $a_0/2\langle 111\rangle$; in 5% of the cases, the loops were seen to be split into smaller ones (apparently the cascade core and loop position coincided, so the initial loop was destroyed); and finally, in 5% of the cases, the coalescence of the pre-existing loops was observed (the loop Burgers vector was changed to $a_0/2\langle 111\rangle$ and then the loop migrated to join the neighboring one driven by elastic interactions).

The second batch of the results concerns the impact of the α' precipitates on the primary damage state in Fe-10Cr, *i.e.*, a model alloy for FM steels. The comparative study of Fe-10Cr matrix with and without Cr precipitates involved 20 cascades with a PKA energy of 20 keV for each precipitate size, ranging from 0.5 to 4 nm. It was found that the number of surviving defects and clustered fractions are not changed by the presence of the precipitate, irrespective of its size. Precipitates of size 1 nm and 0.5 nm were regularly seen to dissolve (1 nm partially, 0.5 nm totally) during the collisional stage. In turn, pre-existing 2 and 4 nm precipitates are not dissolved or modified in any significant way. SIAs and SIA clusters initially formed inside the stable precipitates are observed to migrate from the precipitate core towards the precipitate matrix interface, which is dictated by the fast diffusion and defect energy minimization (the formation energy of the Cr-Cr dumbbell in Cr is higher than the Fe-Cr one in Fe). Cascades evolving near the core of the large precipitates are observed to split more easily because of the presence of the precipitates. It can therefore be concluded that the main effect of the Cr precipitate on the primary damage is the formation of a zone enriched with SIA defects near the precipitate-matrix interface, while for 20 keV (and higher) PKAs, the cascade itself dissolves precipitates of size smaller than 1 nm [129,130].

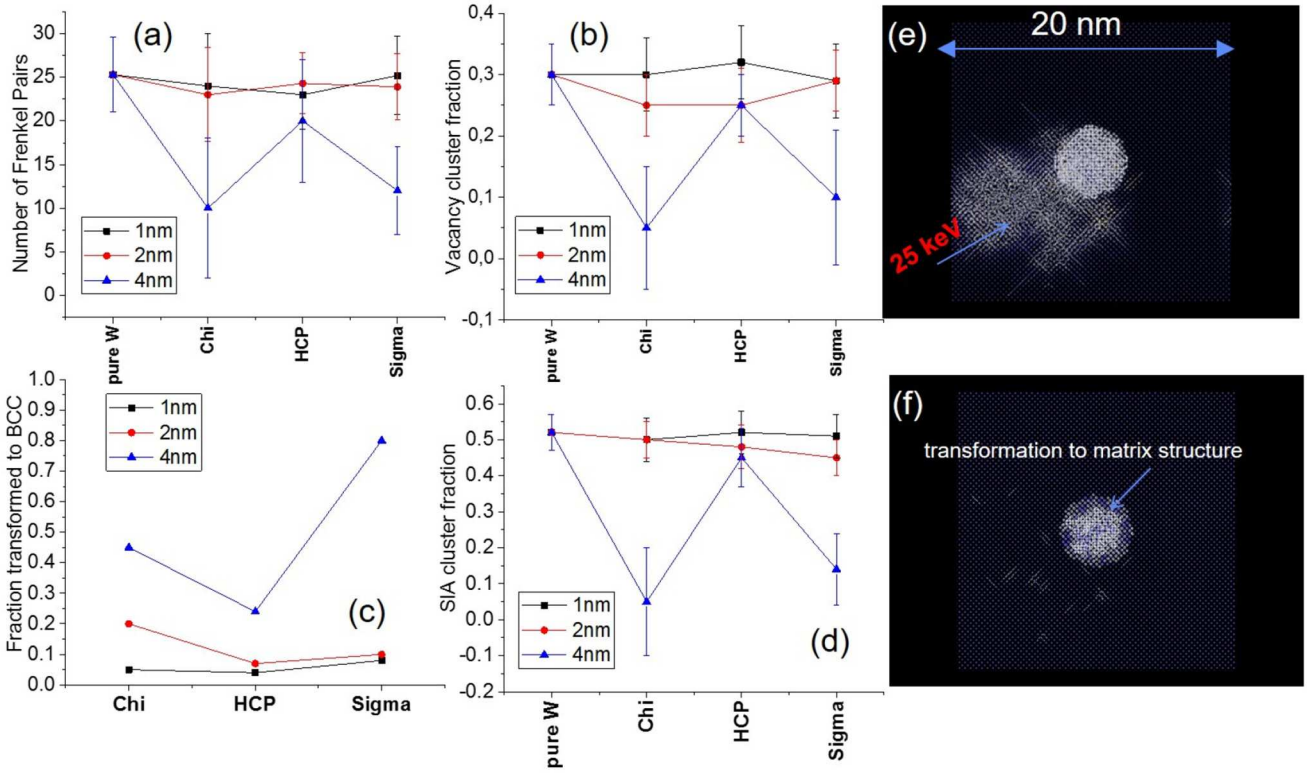

Fig. 37. Information on the primary damage state ((a) number of Frenkel pairs; (b) fraction of clustered vacancies; (c) fraction of atoms forming the precipitate, which transformed to bcc; (d) fraction of clustered SIAs) obtained in tungsten subjected to 25 keV at 873 K. Panel (e) shows the non-bcc atoms (basically defects) at the peak of collisional stage and Panel (f) after cascade cooling. The case corresponds to a 4 nm σ phase precipitate at 873 K. By comparing (e) with (f) one can see that a part of the precipitate has transformed to become coherent with the matrix.

The next batch of the results highlights the study relevant for the RPV steels. According to the current understanding, one important component of the hardening induced by neutrons in RPV steels is due to the formation of Ni-Cu-Mn solute clusters [131], which are bound together thanks to the presence of vacancies and SIAs generally these defects are called solute rich clusters (SRC). Two types were studied here: vacancy-rich SRC, and $a_0\langle 100\rangle$ loop decorated by the Ni-Cu-Mn solutes (*i.e.*, SIA-rich SRC). The decoration of the loops and vacancy clusters by the solutes were obtained from Metropolis Monte Carlo simulations in the relevant temperature range, using the same methodology as in our earlier works [132,133,117]. MD simulations of the cascades revealed that the number of surviving defects is not modified by the pre-existing solute rich clusters. The fraction of clustered point defects is, however, sensitive to the presence of alloying elements and pre-existing dislocation loops. The fraction of clustered SIAs and vacancies for different initial microstructures is reported in fig. 36. In particular, it can be seen that the SIA clustering is influenced primarily by the presence of Ni and Mn, while the vacancy clustering is sensitive to the presence of Cu atoms and so-called RPV composition. This sensitivity is explained by the existence of the strong binding between the respective solutes and point defects. The cascade-induced shock wave induces partial dissolution, short-range migration and subsequent coarsening of the decorated loops, which occurs in a similar way as in pure Fe with pre-existing loops.

Finally, the last subsection describes the results obtained for the simulation of cascades in tungsten containing Re precipitates. Re precipitates of size 1, 2 and 4 nm with σ, χ and hcp structures were created inside pure bcc W and relaxed to obtain global zero pressure in the crystal. Cascades were performed at 873 K with a 25 keV PKA energy. Ten cascades for each case were simulated. It was found that depending on the size of the precipitate there can be a non-negligible impact on the primary damage state. Namely, the effect was clearly pronounced for 4 nm precipitates. Irrespective of the initial precipitate structure, the total number of point defects produced was reduced (see fig. 37(a)). The same concerned the fraction of clustered vacancies and SIAs (see figs. 37(b) and (d)). Structural analysis at the post-collision stage has shown that the cascade-induced local phase transformation making part of the precipitate coherent with the matrix. This transformation basically "consumed" point defects created by the cascade, resulting in the reduction of the total number of point defects. For small precipitates, such transformation was not observed (see fig. 37(c)), as the fraction of the transformed precipitate and the primary damage state features remain the same as in pure W within the statistical error.

5.1.3 Summary of results

To summarize, the simulation of primary damages in Fe, Cu, α- and β-Zr directly revealed the effect of lattice symmetry on the morphology of the formed defects. The approximate invariance of cluster size distributions with respect to the cascade damage energy was observed.

It is possible to single out several statements regarding the impact of the pre-exiting defects typical for FM steels, RPV steels and tungsten. In the case of the studied Cr α' particles, Ni-Mn-Cu solute-rich clusters and dislocation loops, the main features of the primary damage state (*i.e.*, number of survived defects and clustered fraction of point defects) are not affected by the pre-existing defects. In the case of tungsten containing non-coherent Re precipitates, the total number of cascade-produced defects is reduced due to the local phase transformation converting a fraction of the precipitate into a coherent phase with the W matrix. The reported above apparent impact of the precipitates on the primary damage state is proven by statistical analysis of results.

5.2 Displacement cross-sections obtained using molecular dynamics

To use the results of MD modeling and measured data [134–136] for calculation of radiation damage rate advanced atomic displacement cross-sections were obtained for materials from beryllium to bismuth.

The number of stable defects produced by irradiation was calculated using a less rigorous method than discussed above, which, however, makes it possible to obtain the number of defects in the entire energy range of interest. The idea of the method is to "cut off" the BCA modeling at a certain energy of the moving ion T_{crit} and calculate the number of defects formed at energies below T_{crit} using the results of MD simulation. The energy T_{crit} is usually equal to 30–60 keV [137,138].

Reference [139] shows examples of such calculations for Fe+Fe and O+Fe interactions. BCA calculations were performed using the IOTA code [82] and the SRIM code [17]. In one set of calculations the number of stable defects at ion energies below T_{crit} were estimated, according to Stoller and Greenwood [80,140], in another set calculated with the arc-dpa formula [83,68] with Nordlund parameters. A brief explanation of SRIM calculations applying results of MD modeling can be found in ref. [82]. Experimental points and the systematics curve were derived from measurements in ref. [141]. Figures demonstrate a reasonable agreement between simulations and results of measurements.

The arc-dpa approach, the BCA model implemented in IOTA code [82], nuclear models, and recoil energy distributions from evaluated data libraries were applied for the calculation of atomic displacement cross-sections for various materials.

Calculations were performed for neutron and proton irradiation using the arc-dpa model at primary nucleon energies up to 10 GeV. Results are discussed in refs. [139,142].

The parameters E_d, b_{arc}, and c_{arc} [83,68] obtained by Nordlund were applied for Fe, Ni, Cu, Pd, Ag, W, Pt, and Au. For other materials the parameters were estimated using a semi-empirical systematic approach [137]. The approach [137] utilizes the correlations between minimum, averaged, and effective threshold displacement energies and a number of quantities such as melting temperature, material density, cohesive energy, and others.

As an illustration, figs. 38 and 39 show the E_d and c_{arc} parameters evaluated using experimental data and systematics in ref. [137]. The b_{arc} parameter for all materials, except those mentioned above, was taken -0.82 [143].

Obtained E_d, b_{arc}, and c_{arc} values [137] and Nordlund data were employed for the calculation of atomic displacement cross-sections for elements from beryllium to uranium. A local version of the NJOY (KIT) code with implemented arc-dpa equations was applied for calculations.

The data obtained on the basis of JEFF-3.3, ENDF/B-VIII, and JENDL-4.0 at neutron energies below 20 MeV were extended up to 200 MeV using the data prepared with TENDL-2017.

The displacement cross-sections in ENDF-6 format were processed using the NJOY code and recorded in the ACE format. The data in both formats, obtained using JEFF-3.3, ENDF/B-VIII, JENDL-4.0, and TENDL-2017 data are distributed as a part of DXS (KIT) library [144].

5.3 Methodology for irradiation simulation inter-comparisons

A new methodology to determine the primary displacement damage was explored in this paper, within the framework of the material testing for nuclear fusion development program, which uses a combination of computational techniques as shown previously. The main objective was to improve the methodology earlier used for inter-comparison of irradiation experiments, *i.e.* using a more realistic technique than using the NRT model [1], in order to be able to design equivalent nuclear fusion experiments.

This methodology determines the primary displacement damage dose rate induced by neutrons, coupling codes of neutron transport calculations (MCNP code), nuclear data processing (NJOY code) and a combination of binary collision approximation (BCA) and MD (BCAMD methodology [85]), fig. 40. Several previous works were published

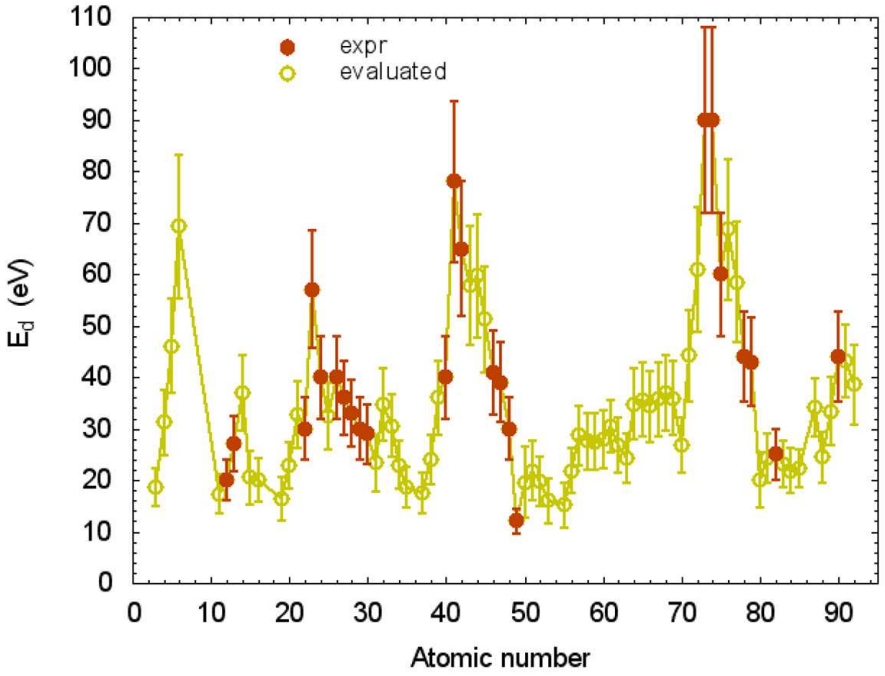

Fig. 38. The average threshold energy E_d values evaluated for different materials.

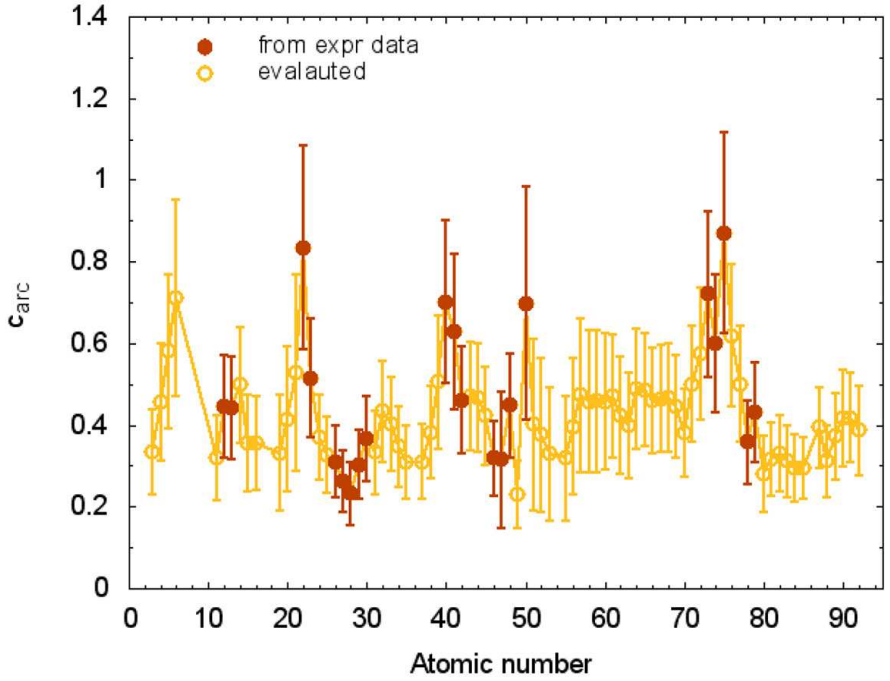

Fig. 39. The c_{arc} values evaluated for different materials.

using a similar methodology, but considering pure BCA (MARLOWE code [18,145]) in order to compare different irradiation experiments [146–149].

On the one hand, the PKA spectrum is obtained integrating the neutron spectrum, by means of MCNP5 v1.6 code [150], with recoils matrix, through the module GROUPR of NJOY2016 code [45], and considering the nuclear data libraries FENDL 3.1b [151]. On the other hand, to determine the defects generated by high-energy PKAs induced by fusion neutrons in an efficient and accurate way, a hybrid method BCAMD-CIEMAT was recently developed [85]. This methodology consists on coupling BCA (MARLOWE code [18,145]) with MD calculations (LAMMPS code [152]).

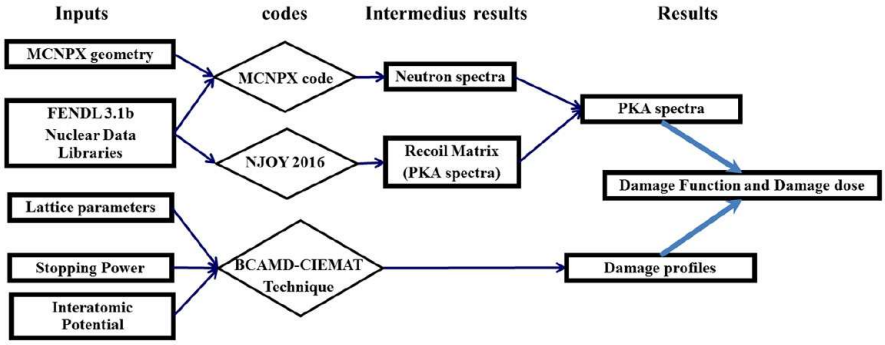

Fig. 40. Methodology block diagram.

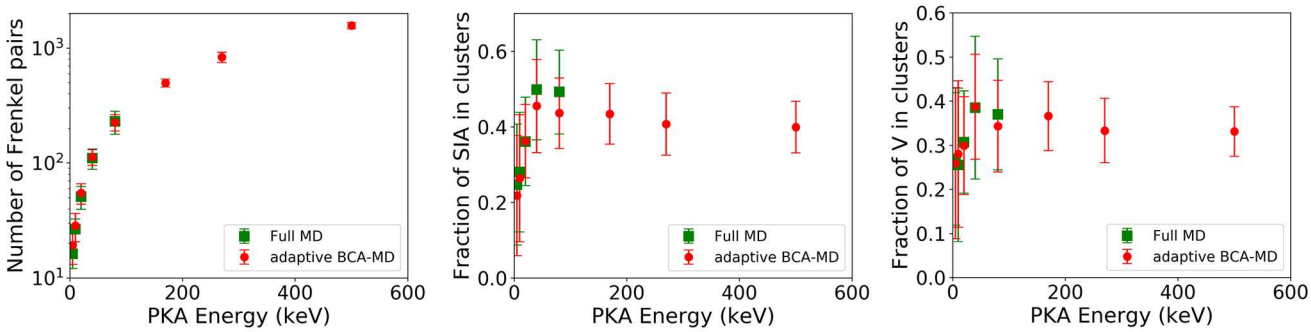

Fig. 41. Calculations developed so far up to 0.5 MeV PKA energy show the number of FPs, fraction of self-interstitials atoms (SIA), then vacancies in clusters as a function of PKA energy.

Finally, integrating the PKA spectrum with damage profile, the displacement damage function and damage dose are obtained, fig. 40.

Indeed, though MD allows accounting for complex processes during cascades such as the emission of phonons, the agglomeration and the recombination of defects, it becomes computationally prohibitive when the PKA energy is high (> 100 keV) as the number of atoms in the system increases drastically to contain the cascade. Therefore, BCA is preferred to simulate collision cascade for high energies as it only follows the trajectory of displaced atoms, and is thus, much cheaper from a computational point of view. However, when the kinetic energy of atoms falls below a critical value, the BCA breaks down. In addition, it does not take into account any interatomic potential to account for the interaction of defects during last stages of the cascade. Hence, it fails at predicting correctly the final state of the damage.

In the BCAMD method, the ballistic phase is simulated with the BCA. During the BCA simulation, atoms in motion are stopped when their kinetic energy falls below a threshold energy fixed in advance (~ 250 eV). Then, the information obtained with the BCA is transferred to a MD cell, which simulate the last stages of the cascade [85].

The BCAMD technique was validated against full MD calculations for PKA energies from 5 keV up to 80 keV [85] in Fe. It reproduces very well the number of Frenkel pairs, the fraction of Self-Interstitials Atoms (SIA) and Vacancies (V) in clusters as well as their size distribution, as can be seen in fig. 41. The acceleration of MD calculations achieved with the BCAMD is considerable and increases with the PKA energy. For a PKA energy of 80 keV, an acceleration factor higher than 30 was measured. After validation, the BCAMD method was used to simulate collision cascades in Fe for PKA energies up to 0.5 MeV, which is prohibitive with full MD calculations. In fact 60000 cores of the HECToR supercomputer [153] were necessary during 24 h to simulate cascades with a PKA energy of 0.5 MeV in Fe. With the BCAMD method, a computational effort of 96 min using only 2880 cores of the HPC Marconi [154] was necessary to simulate each cascade. This corresponds to a speedup factor of 312 with respect to full MD calculations [85]. Results obtained with the BCAMD are reported in fig. 41.

The results obtained with the BCAMD-CIEMAT are in very good agreement with other MD data found in the literature and with the general trend defined by the fit obtained by the OECD [85]. These results are represented together with the OECD data in fig. 31.

Then, this BCAMD technique was coupled with the methodology designed to determine the damage function induced by neutrons, fig. 40, with the aim to integrate the PKA spectra with the damage profile. Once the damage profile of number of Frenkel pairs, vacancies in clusters and SIA in clusters *versus* PKA energy is obtained using the BCAMD methodology, they are integrated with the PKA spectra induced by the different neutron sources with the

Table 5. Displacement damage using both calculations methodologies, BCAMD-CIEMAT and NRT model, for all neutron source assessed. The fraction of V and SIA in clusters are also shown.

Facilities	Neutron flux [n/cm^{2}s]	Damage dose rate [DPA_{BCAMD}/fpy]	Damage dose rate [DPA_{NRT}/fpy]	Fraction of V in clusters [VCPA/DPA_{BCAMD}]	Fraction of SIA in clusters [ICPA/DPA_{BCAMD}]
DONES Highest	3.91E+14	7.1	14.6	0.35	0.41
DONES Lowest	9.34E+13	1.6	3.3	0.35	0.40
FW DCLL	7.24E+14	6.1	11.2	0.35	0.39
FW WCLL	5.42E+14	5.9	12.2	0.35	0.40
FW HCPB	4.50E+14	5.2	8.9	0.35	0.40
BR2-D60	1.51E+13	0.2	0.4	0.37	0.42
BOR60	2.27E+15	12.5	28.3	0.37	0.37
EBRII	3.31E+15	20.2	44.9	0.37	0.38
HFIR	5.10E+15	13.6	30.2	0.37	0.40
PWR-HBR2	2.70E+11	0.001	0.002	0.37	0.39

aim to determine the displacement damage function (eq. (31)) and damage dose rate (eq. (32)) following the next equations:

$$W = \frac{1}{D/t} \int^{T} \sigma_{PKA}(T') N_d(T') \mathrm{d}T', \tag{31}$$

where $\sigma_{PKA}(T)$ is the PKA spectrum, $N_d(T)$ is the number of Frenkel pairs *versus* PKA energy [T], and D/t is the rate of damage created by the atomic displacement,

$$dpa = t\phi_{total} \int_{T_o}^{T_{MAX}} \sigma_{PKA}(T) N_d(T) \mathrm{d}T, \tag{32}$$

where σ_{Total} is the total neutron fluence rate and "t" is the exposition time. This dpa concept calculated using the damage profile obtained using BCAMD methodology is going to be named in the rest of the document as DPA_{BCAMD}.

Using eq. (32), two additional concepts of dpa are proposed in this document, beside of the conventional concept based on the number of Frenkel pairs, the one obtained with the number of vacancies in clusters and the one obtained using the number of interstitial in cluster. The aim of these new dpa concepts is to give more information to the comparison of the irradiation experiments. They are going to be named Vacancies in Clusters Per Atoms ($VCPA_{BCAMD}$) and Interstitials in Clusters Per Atoms ($ICPA_{BCAMD}$). Then, this new methodology allows adding two more magnitudes which give valuable important information about how the primary displacement damage is produced in the bulk of the materials.

5.3.1 Results: Comparison of different neutron sources

The displacement damage dose rate [DPA_{BCAMD}/fpy] in iron induced by different neutron spectra including several concepts of future fusion power plants, fission reactors and HFTM-DONES are calculated in order to compare different irradiation experiments. In addition, the magnitudes $VCPA_{BCAMD}$ and $ICPA_{BCAMD}$ have been represented as a function of the dpa_{BCAMD}/fpy in order to assess the ratio of vacancies or interstitials in clusters to displacement damage dose rate.

The number of Frenkel pair obtained using both methodologies, BCAMD and NRT are represented in table 5, for the several kinds of neutron sources analyzed. In addition, the fraction of vacancies and Interstitial in clusters is also shown in this table. The neutron spectra assessed are shown in fig. 42. For IFMIF-DONES [155–157] have been selected two spectra correspond to the sample containers of High Flux Test Module (HFTM) [158] in both the most (HFTM Highest flux) and less (HFTM Lowest flux) irradiated positions. As examples of the different concepts of DEMO under study, neutron spectra taken from the First Wall (FW) of the DEMO concepts DCLL [159,160], WCLL [161] and HCPB [162,163] are used for this analysis. And finally, as examples of fission reactors, the neutron spectra of the facilities BR2 [164], HFIR [30] BOR60 [165], EBRII [166] and an example of PWR-HBR2 [167] fission reactor are selected for this work.

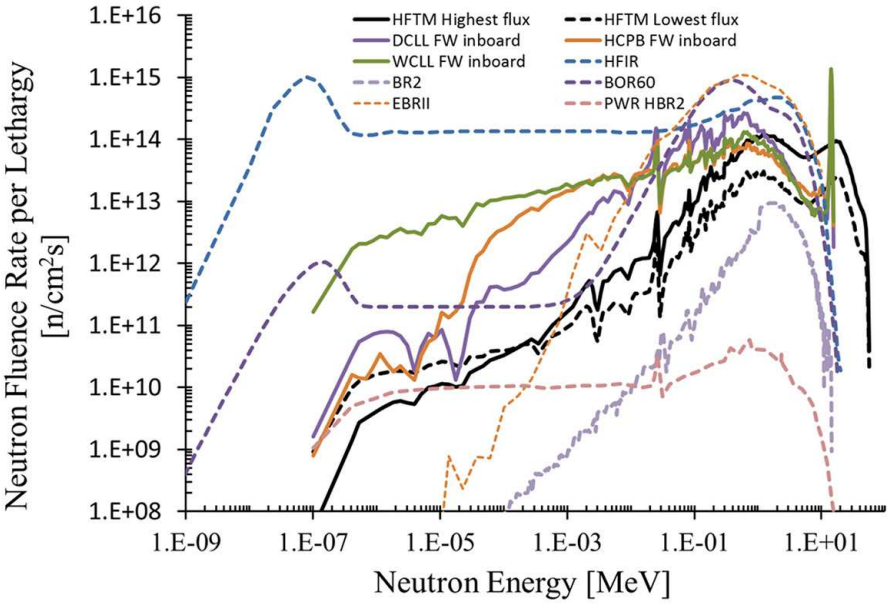

Fig. 42. Neutron spectra of the neutron sources evaluated for this work.

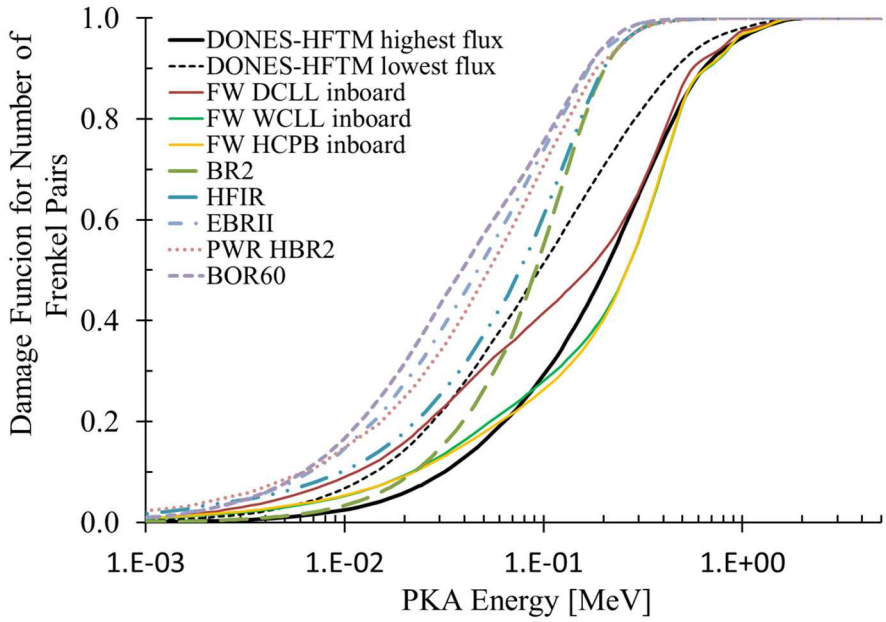

Fig. 43. Damage function for the different neutron sources assessed.

In addition, the damage functions calculated using the BCAMD technique to obtain the damage profile is presented in fig. 43, for the neutron source evaluated. It is clearly observed that the median energy of the PKA for fission is lower than the one expected for nuclear fusion reactor and DONES facility.

The vacancies and interstitial per atoms in clusters [$VCPA_{BCAMD}$ and $ICPA_{BCAMD}$] to displacement damage dose [DPA_{BCAMD}] ratio are also shown in table 5. It is clearly observed that the vacancies in clusters per atoms to displacement damage ratio [VCPA/DPA_{BCAMD}] points are similar for all facilities studied, 0.35 for fusion and DONES facilities and 0.37 for fission reactors. The same trend is observed for interstitials in cluster per atoms to displacement damage dose ratio [ICPA/DPA_{BCAMD}] which has similar values for all the installations studied, about 0.40. Therefore, the main conclusion of the comparison of the values of primary damage dose and clustering obtained using this methodology is that the primary displacement damage and clustering are produced in a very similar way for all neutron spectra evaluated. This is a very important conclusion for damage comparison (at initial stages) of different experiments.

Table 6. He and H ratios calculated using the dpa for both concepts analyzed, BCAMD and NRT.

Facilities	He ratio [He appm/DPA_{BCAMD}]	H ratio [H appm/DPA_{BCAMD}]	He ratio [He appm/DPA_{NRT}]	H ratio [H appm/DPA_{NRT}]
DONES Highest	27.1	110.6	13.1	53.6
DONES Lowest	29.4	118.8	14.3	57.9
FW DCLL	16.6	71.1	9.0	38.6
FW WCLL	24.5	172.5	11.8	83.5
FW HCPB	20.3	86.5	12.0	50.9
BR2-D60	1.0	12.0	0.5	5.6
BOR60	0.7	6.5	0.3	2.9
EBRII	0.7	6.8	0.3	3.1
HFIR	0.78	11.57	0.35	5.21
PWR-HBR2	0.8	8.97	0.38	4.25

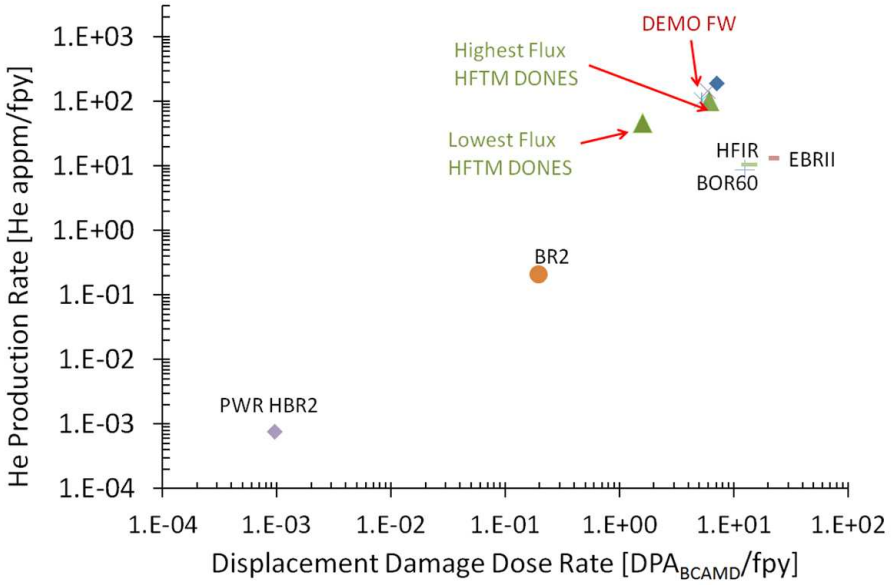

Fig. 44. He production rate [He appm/fpy] *versus* displacement damage rate [DPA_{BCAMD}/fpy].

However, if the He and H production to displacement damage ratios (He and H ratios) are obtained, it is clearly observed that the trend is different. The calculations of the He and H production was performed with the MCNP5 V1.6 and using the same nuclear data library used for the PKA spectra calculations, *i.e.* the nuclear data library FENDL 3.1b [151]. In table 6, the He and H production to damage dose ratios calculated using both kinds of dpa concepts analyzed in this section, BCAMD and NRT, are shown for all neutron sources analyzed. The He production rate [He appm/fpy] *versus* damage dose rate obtained for the different kind of neutron sources analyzed using the DPA_{BCAMD} concept is shown fig. 44. It is clearly observed that, as expected, the different neutron sources present very different He ratios [He appm/dpa]. In addition, the same behaviour is observed for H ratio [H appm/dpa], table 6. Therefore, although the clustering induced for the different neutron spectra assessed is similar, the differences found in the He and H ratios will cause different evolution of damage [168] with time.

5.3.2 Discussion of inter-comparison

In order to determine the displacement dose induced by neutrons in materials using a much more realistic methodology than using the NRT model [1] a methodology to determine the displacement damage dose rate has been developed coupling codes of neutron transport calculations, nuclear data processing and a combination of binary collision approximation and molecular dynamics (BCAMD [85]).

This methodology is able to determine not only the primary displacement damage dose rate induced by the different neutron sources but also the produced clustering, which was not possible with the methodologies used previously. Therefore, this new method adds useful information to the comparison of different irradiation experiments, which could be very useful in order to try to design equivalent irradiation experiments for example for material nuclear fusion technology development.

This methodology has confirmed that, although the clustering produced by the different neutrons sources are similar, the He and H production is very different, because it depends strongly on the neutron energy. Hence, the evolution of defects will be very probably different. In order to design equivalent irradiation experiments, it is important not only to reproduce the displacement damage dose and clustering but also the He and H ratios, as it is possible to observe in a lot of experiments [168,169].

6 Conclusions

The simulation of neutron-induced radiation damage in materials is complicated by competing displacement events and nuclear-reaction effects. Fortunately, in the structural materials used in existing fission applications the dominant driver seems to be displacement damage from elastic events, as opposed to non-elastic, which generally only slowly (in time) results in lasting changes to materials due to the high rate of recombination. This explains why the defect production cross-section metric based on damage energy, which leads to the displacement per atom (dpa) measure, has been successful in correlating radiation effects in those (iron-based) materials under different irradiations environments —thermal, mixed or fast, neutrons and ions— allowing the results to be sensibly compared.

However, there is little basis and no experimental evidence that the others effects, mostly occurring in the fast regime or ion accelerator environments where non-elastic events dominate, can still be considered as secondary or negligible. It is clear that the earlier nuclear damage databases did not cater for those considerations. In some non-iron-based structural materials transmutation due to thermal neutron (n,γ) and/or (n,α) and (n,p) reactions can be significant, and in all materials where the non-elastic events have a significant impact (above a few hundreds keV incident neutron energy) there can be non-negligible secondary events or consequences. The simple correlation between defect productions and recoil damage energy is then invalid because the recoil atom is not of the same element, nucleon away; the emitted charged particle is in the MeV energy range; most event scattering law are highly anisotropic; the target is a compound, non-metallic, etc. Transmutation changes the composition of materials with time, and this can significantly modify the carefully crafted original material engineering properties. Consequently, the characterization of radiation damage in materials must take into account transmutation as well as displacement damage metrics from non-elastic events to properly predict the evolution of radiation damage in materials in the different technologies: space, fusion, accelerator, novel fission, etc. In those cases the PKAs of the often radioactive transmuted elements, energy/angle-dependent multiple emitted particles, gas production, break-up and decay-emission events need to be also considered to properly and physically simulate the time-dependent changes in material properties under challenging irradiation conditions.

Progress in data provision at the nuclear scale, assuming that the general purpose nuclear data file are fit to the tasks (of sufficient completeness to capture all relevant processes particularly at high energy), is a step forward in the proper understanding of material defect metrics induced by radiation but this is very small step with regard to the seamless integration of the models across the length (nm - μm - mm - m) and time (ps - μs - ms - s) scales into one coherent modelling framework.

Fundamentally, the above leads to the conclusion that a simple integral measure such as dpa (NRT, arc, or other) is not sufficient, even though it may be a good first order estimate, to fully capture the damage metrics from complex irradiation —more substantial methodologies and algorithms from the nuclear-reaction space (as described in this paper, and allowing uncertainty quantification and propagation) to the molecular-material ones must be included in complete plant and material modelling. At the same time, the historical correlative benefits of integral measures must be acknowledged and their continued inclusion as a metric —if only as a cross-comparison to historical data and work— necessitates the continued development and improvement of metrics relevant to material evolution under irradiation and defect production cross-section. However, in this latter case, the improvements must accept the limitation and not deviate too significantly from the comparative and correlative benefits of the NRT-dpa original, as stated by its founders.

This work was partially funded under the auspices of the International Atomic Energy Agency coordinated research project F44003 2013-2018 [48] and each authors institute and government. J.-Ch. Sublet and M. Gilbert acknowledge funding by the RCUK Energy Programme (grant number EP/P012450/1).

7 Glossary

BCA:	binary bollision approximation
CANDU:	CANada Deuterium Uranium
DPA/dpa:	displacement per atom
DPCS:	defect production cross-section
DONES:	DEMO oriented neutron source
DCLL:	dual-cooled liquid lithium lead breeder DEMO
ENDF:	evaluated nuclear data file
FP:	Frenkel pair
FW:	first wall
GEM:	generalized evaporation model
HFIR:	high flux isotope reactor
HCPB:	helium-cooled pebble-bed breeder DEMO
IFMIF:	international fusion materials irradiation facility
IAEA:	International Atomic Energy Agency
KERMA:	kinetic energy release in material
LSS:	Lindhard-Scharff-Schiott
MD:	molecular dynamics
NRT:	Norgett-Robinson-Torrens
PDF:	probability density function
PKA:	primary knock on atoms
RPV:	reactor pressure vessel
PWR:	pressurized water reactor
SIA:	self-interstitial atom
SRC:	solute-rich clusters
WCLL:	water-cooled liquid lithium lead breeder DEMO
ZBL:	Ziegler-Biersack-Littmark
appm:	atomic parts per million
bcc:	body-centered cubic lattice
fcc:	face-centered cubic lattice

References

1. M.J. Norgett, M.T. Robinson, I.M. Torrens, Nucl. Eng. Des. **33**, 50 (1975).
2. G.R. Odette, D.R. Doiron, Nucl. Tech. **29**, 346 (1976).
3. D. Simeone, J.M. Costantini, L. Luneville, L. Desgranges, P. Trocellier, P. Garcia, J. Mater. Res. **30**, 1495 (2015).
4. G.J. Dienes, G.H. Veneyard, *Radiation Effects in Solids* (Interscience, New York, 1957).
5. N. Bohr, J. Lindhard, Mat. Fys. Medd. Dan. Vid. Setsk. **18**, 1495 (1948).
6. J. Lindhard, M. Scharff, H.E. Schiøtt, Mat. Fys. Medd. Dan. Vid. Selsk **33**, l (1963).
7. D. Simeone, L. Luneville, Y. Serruys, Phys. Rev. E **82**, 011122 (2010).
8. D. Simeone, L. Luneville, J.P. Both, EPL **83**, 56002 (2008).
9. L. Luneville, D. Simeone, W. Weber, J. Nucl. Mater. **415**, 55 (2011).
10. L. Luneville, K. Mallick, V. Pontikis, D. Simeone, Phys. Rev. E **94**, 0521262 (2016).
11. L. Luneville, D. Simeone, C. Jouanne, J. Nucl. Mater. **353**, 89 (2006).
12. P. Sigmund, *Radiation Damage Processes in Materials* (Dupuy, Leiden, 1975).
13. J. Lindhard, V. Nielsen, M. Scharff, Mat. Fys. Medd. Dan. Vid. Setsk. **36**, 89 (1968).
14. G.H. Kinchin, R.S. Pease, Rep. Prog. Phys. **18**, 1 (1955).
15. Don M. Parkin, C. Alton Coulter, J. Nucl. Mater. **101**, 261 (1981).
16. D. Simeone, O. Hablot, V. Micalet, P. Bellon, Y. Serruys, J. Nucl. Mater. **246**, 206 (1997).

17. J.F. Ziegler, M.D. Ziegler, J.P. Biersack, Nucl. Instrum. Methods Phys. Res. B **268**, 1818 (2010) http://srim.org/.
18. M.T. Robinson, J. Nucl. Mater. **216**, 1 (1994).
19. G. Demange, E. Antoshchenkova, M. Hayoun, L. Luneville, D. Simeone, J. Nucl. Mater. **486**, 26 (2017).
20. M.T. Robinson, *The Energy Dependence of Neutron Damage in Solid*, in *ICE Virtual Library - Nuclear fusion reactors* (1970) pp. 364–378.
21. D.J. Bacon, A.F. Calder, F. Gao, V.G. Kapinos, S.J. Wooding, Nucl. Instrum. Methods Phys. Res. B **102**, 37 (1995).
22. F. Gao, D.J. Bacon, L.M. Howe, C.B. So, J. Nucl. Mater. **294**, 288 (2001).
23. C.P. Flynn, R.S. Averback, Phys. Rev. B, Rapid Commun. **38**, 7118 (1988).
24. A. Akkerman, J. Barak, IEEE Trans. Nucl. Sci. **53**, 3667 (2006).
25. M. Griffiths, AECL Nucl. Rev. **2**, 1 (2013).
26. L. Greenwood, J. Nucl. Mater. **115**, 137 (1983).
27. L. Luneville, J.-Ch. Sublet, D. Simeone, J. Nucl. Mater. **505**, 262 (2018).
28. T. Khromyleva, I. Bondarenko, A. Gurbich, V. Ketlerov, V. Khryachkov, P. Prusachenko, Nucl. Sci. Eng. **191**, 282 (2018).
29. L.R. Greenwood, B.M. Oliver, J. ASTM Int. **3**, 1 (2006).
30. L.R. Greenwood, R.K. Smither, *SPECTER: Neutron Damage Calculations for Materials Irradiations* (1985) ANL/FPP/TM-197.
31. F.A. Garner *et al.*, J. Nucl. Mater. **122**, 356 (2006).
32. L.R. Greenwood, F.A. Garner, B.M. Oliver, M.L. Grossbeck, W.G. Wolfer, J. ASTM Int. **1**, 1 (2004).
33. H. Liu, M.A. Abdou, L.R. Greenwood, Fus. Eng. Des. **88**, 2860 (2013).
34. L.R. Greenwood, D.G. Graczyk, D.W. Kneff, J. Nucl. Mater. **1335**, 155 (1988).
35. L.R. Greenwood, J. Nucl. Mater. **141–143**, 654 (1986).
36. F.A. Garner, Compreh. Nucl. Mater. **4**, 33 (2012).
37. A.J. Koning, Eur. Phys. J. A **51**, 184 (2015).
38. A.J. Koning, D. Rochman, Nucl. Data Sheets **113**, 2841 (2012).
39. A.J. Koning *et al.*, *TALYS-1.9, User Manual* (Nuclear Research and Consultancy Group NRG, 2017) http://www.talys.eu/download-talys/.
40. A.J. Koning, D. Rochman, J.-Ch. Sublet, N. Dzysiuk, M. Fleming, S. van der Marck, Nucl. Data Sheets **155**, 1 (2019) *Special Issue on Nuclear Reaction Data*.
41. P. Helgesson, H. Sjöstrand, D. Rochman, Nucl. Data Sheets **145**, 1 (2017).
42. R.E. Stoller, G.R. Odette, J. Nucl. Mater. **186**, 203 (1992).
43. R.E. MacFarlane, A.C. Kahler, Nucl. Data Sheets **111**, 2739 (2010).
44. R.E. MacFarlane, D.W. Muir, R.M. Boicourt, A.C. Kahler, J.L. Conlin, W. Haeck, *The NJOY nuclear data processing system, version 2016* (Los Alamos National Laboratory LA-UR-17-20093, 2016) https://github.com/njoy/NJOY2016-manual.
45. *NJOY2016 Nuclear Data Processing System* (2016) https://njoy.github.io/NJOY2016/.
46. J.-Ch. Sublet, J.W. Eastwood, J.G. Morgan, M.R. Gilbert, M. Fleming, W. Arter, Nucl. Data Sheets **139**, 77 (2017) https://fispact.ukaea.uk/.
47. L.R. Greenwood, R.K. Smither, *Displacement Damage Calculations with ENDF/B-V*, in *Proceedings of the Advisory Group Meeting on Nuclear Data for Radiation Damage Assessment and Reactor Safety Aspects, Vienna, Austria* (IAEA, 1981).
48. J.-Ch. Sublet *et al.*, *IAEA Primary Radiation Damage Cross-Sections CRP files* (2018) https://www-nds.iaea.org/CRPdpa/.
49. M.R. Gilbert, J. Marian, J.-Ch. Sublet, J. Nucl. Mater. **467**, 121 (2015).
50. M.R. Gilbert, J.-Ch. Sublet, Nucl. Mater. Energy **9**, 576 (2016).
51. M.R. Gilbert, *SPECTRA-PKA* (2018) code available to download from github at https://github.com/fispact/SPECTRA-PKA.
52. M.R. Gilbert, J.-Ch. Sublet, J. Nucl. Mater. **504**, 01 (2018).
53. A.J. Koning, D. Rochman, *TENDL-2017* (2018) available from https://tendl.web.psi.ch/tendl_2017/tendl2017.html.
54. D.A. Brown *et al.*, Nucl. Data Sheets **148**, 1 (2018) *Special Issue on Nuclear Reaction Data*.
55. A. Trkov, M. Herman, D.A. Brown (Editors), *ENDF-6 Formats Manual, Data Formats and Procedures for the Evaluated Nuclear Data File ENDF/B-VI. ENDF/B-VII and ENDF/B-VIII*, CSEWG Document ENDF-102 BNL-203218 (2018).
56. T. Sato, Y. Iwamoto, S. Hashimoto, T. Ogawa, T. Furuta, S. Abe, T. Kai, Pi-En Tsai, N. Matsuda, H. Iwase, N. Shigyo, L. Sihver, K. Niita, J. Nucl. Sci. Technol. **55**, 684 (2018).
57. Y. Iwamoto, T. Sato, S. Hashimoto, T. Ogawa, T. Furuta, S. Abe, T. Kai, N. Matsuda, R. Hosoyamada, K. Niita, J. Nucl. Sci. Technol. **54**, 617 (2017).
58. K. Niita, Y. Iwamoto, T. Sato, H. Iwase, N. Matsuda, Y. Sakamoto, H. Nakashima, *A new treatment of radiation behaviour beyond one-body observables*, in *Proceedings of International Conference on Nuclear Data for Science and Technology 2007, Nice, France, April 22-27, 2007* (EDP Sciences, 2007).
59. T. Ogawa, T. Sato, S. Hashimoto, K. Niita, Nucl. Instrum. Methods A **763**, 575 (2014).
60. Y. Iwamoto, K. Niita, T. Sawai, R.M. Ronningen, T. Baumann, Nucl. Instrum. Methods B **274**, 57 (2012).
61. S. Furihata, Nucl. Instrum. Methods B **171**, 251 (2000).
62. T. Ogawa, S. Hashimoto, T. Sato, K. Niita, Nucl. Instrum. Methods B **325**, 35 (2014).
63. K. Shibata, O. Iwamoto, T. Nakagawa, N. Iwamoto, A. Ichihara, S. Kunieda, K. Furutaka, T. Oshawa, T. Murata, H. Matsunobu, A. Zukeran, S. Kamada, J. Katakura, J. Nucl. Sci. Technol. **48**, 1 (2011).

64. M.B. Chadwick, P. Obložinský, M.W. Herman *et al.*, Nucl. Data Sheets **112**, 2887 (2011).
65. Y. Iwamoto, T. Ogawa, Nucl. Instrum. Methods B **396**, 26 (2017).
66. Y. Iwamoto, H. Iwamoto, M. Harada, K. Niita, J. Nucl. Sci. Technol. **51**, 98 (2014).
67. P. Griffin, D. Rochman, A. Koning, EPJ Web of Conferences **146**, 02008 (2017).
68. R.E. Stoller *et al.*, *Primary Radiation Damage Cross-Sections, Summary Report of the Second Research Coordination Meeting*, Technical Report INDC(NDS)-0691 (IAEA, 2015) `https://www-nds.iaea.org/publications/indc/indc-nds-0691/`.
69. N. Otsuka *et al.*, Nucl. Data Sheets **120**, 272 (2014).
70. A.J. Koning, D. Rochman, Ann. Nucl. Energy **35**, 2024 (2008).
71. E. Bauge, P. Dossantos-Uzarralde, J. Korean Physical Society **59**, 1218 (2011).
72. E. Bauge, M. Dupuis, S. Hilaire, S. Péru, A.J. Koning, D. Rochman, S. Goriely, Nucl. Data Sheets **118**, 32 (2014).
73. D. Rochman, E. Bauge, A. Vasiliev, H. Ferroukhi, EPJ Nucl. Sci. Technol. **3**, 14 (2017).
74. D. Rochman, E. Bauge, A. Vasiliev, H. Ferroukhi, G. Perret, EPJ Nucl. Sci. Technol. **4**, 7 (2018).
75. D.C. Larson, D.M. Hetrick, N.M. Larson, C.Y. Fu, S.J. Epperson, *Evaluation of* ^{28,29,30}*Si for ENDF/B-VI*, Technical Report ORNL-TM-11825 (ORNL, 1991).
76. W.E. Kinney, J.W. McConnell, *High resolution neutron scattering experiments at ORELA*, in *Proceedings of International Conference of Neutron Interaction with Nuclei Lowell, MA, USA*, Vol. **2** (1976) p. 1319.
77. F.G. Perey, T.A. Love, W.E. Kinney, *A test of neutron total cross-section evaluations from 0.2 to 20*MeV *for C, O, Al, Si, Ca, Fe, and Si02*, Technical Report ORNL-4823 (ORNL, 1972).
78. S.P. Simakov, A.J. Koning, A.Yu. Konobeyev, EPJ Web of Conferences **146**, 02012 (2017).
79. S.P. Simakov, U. Fischer, A.J. Koning, A.Yu. Konobeyev, D.A. Rochman, Nucl. Mater. Energy **15**, 244 (2018).
80. R.E. Stoller, L.R. Greenwood, J. Nucl. Mater. **271-272**, 57 (1999).
81. S.P. Simakov, A.Yu. Konobeyev, U. Fischer, V. Heinzel, J. Nucl. Mater. **386**, 52 (2009).
82. A.Yu. Konobeyev, U. Fischer, Yu.A. Korovin, S.P. Simakov, *IOTA-2017: a code for the simulation of ion transport in materials* (2017) KIT Scientific Working Papers 63 `https://publikationen.bibliothek.kit.edu/1000077011`.
83. K. Nordlund, A.E. Sand, F. Granberg, S.J. Zinkle, R. Stoller, R.S. Averback, T. Suzudo, L. Malerba, F. Banhart, W.J. Weber, F. Willaime, S. Dudarev, D. Simeone, *Primary Radiation Damage in Materials*, Report NEA/NSC/DOC(2015)9 (2015).
84. Kai Nordlund, Steven J. Zinkle, Andrea Sand, Fredric Granberg, Robert S. Averback, R.E. Stoller, Tomoaki Suzudo, Lorenzo Malerba, Florian Banhart, William Weber, Francois Willaime, Sergei Dudarev, D. Simeone, Nat. Commun. **9**, 1 (2018).
85. C.J. Ortiz, J. Comb. Mat. Sci. **154**, 325 (2018).
86. R.E. Stoller, Compreh. Nucl. Mater. **1**, 293 (2012).
87. K. Nordlund, J. Wallenius, L. Malerbar, Nucl. Instrum. Methods B **246**, 32 (2005).
88. C.S. Becquart P. Olsson, C. Domain, Mat. Res. Lett. **4**, 219 (2016).
89. Subcommittee E10.05 on Nuclear Radiation Metrology, *ASTM standard E693-17: Standard Practice for Characterizing Neutron Exposures in Iron and Low Alloy Steels in Terms of Displacements Per Atom (DPA)* (ASTM International, 2012).
90. J.A. Horak, T.M. Blewitt, J. Nucl. Mater. **49**, 161 (1973).
91. S. Takamura, T. Arubat, J. Nucl. Mater. **136**, 159 (1985).
92. G. Wallner, M.S. Anand, L.R. Greenwood *et al.*, J. Nucl. Mater. **152**, 146 (1988).
93. A. Trkov, R. Capote, Phys. Proc. **64**, 48 (2015).
94. A.F. Calder, D.J. Bacon, A.V. Barashev, Yu.N. Osetsky, Philos. Mag. **90**, 863 (2010).
95. M. Samaras, P.M. Derlet, H. Van Swygenhoven, M. Victoria, Phys. Rev. Lett. **88**, 125505 (2002).
96. Mai Ghaly, R.S. Averback, Phys. Rev. Lett. **72**, 364 (1994).
97. Mai Ghaly, Kai Nordlund, R.S. Averback, Philos. Mag. A **79**, 795 (1999).
98. N.P. Lazarev, V.I. Dubinko, Radiat. Effects Defects Solids **158**, 803 (2003).
99. N.P. Lazarev, A.S. Bakai, J. Supercrit. Fluids **82**, 22 (2013).
100. M. Eldrup, B.N. Singh, S.J. Zinkle, T.S. Byun, K. Farrell, J. Nucl. Mater. **307-311**, 912 (2002).
101. G.R. Odette, G.E. Lucas, JOM **53**, 18 (2001).
102. E. Meslin, M. Lambrecht, M. Hernández-Mayoral, F. Bergner, L. Malerba, P. Pareige, B. Radiguet, A. Barbu, D. Gómez-Briceño, A. Ulbricht, A. Almazouzi, J. Nucl. Mater. **406**, 73 (2010).
103. A. Kuramoto, T. Toyama, Y. Nagai, K. Inoue, Y. Nozawa, M. Hasegawa, M. Valo, Acta Mater. **61**, 5236 (2013).
104. Wei-Ying Chen, Yinbin Miao, Yaqiao Wu, Carolyn A. Tomchik, Kun Mo, Jian Gan, Maria A. Okuniewski, Stuart A. Maloy, James F. Stubbins, J. Nucl. Mater. **462**, 242 (2015).
105. Takaaki Koyanagi, N.A.P. Kiran Kumar, Taehyun Hwang, Lauren M. Garrison, Xunxiang Hu, Lance L. Snead, Yutai Katoh, J. Nucl. Mater. **490**, 66 (2017).
106. M. Fukuda, T. Tanno, S. Nogami, A. Hasegawa, Mater. Trans. **53**, 2145 (2012).
107. S.J. Zinkle, B.N. Singh, J. Nucl. Mater. **351**, 269 (2006).
108. F.A. Garner, M.B. Toloczko, B.H. Sencer, J. Nucl. Mater. **276**, 123 (2000).
109. M.B. Toloczko, F.A. Garner, V.N. Voyevodin, V.V. Bryk, O.V. Borodin, V.V. Mel'nychenko, A.S. Kalchenko, J. Nucl. Mater. **453**, 323 (2014).
110. G.J. Ackland, M.I. Mendelev, D.J. Srolovitz, S. Han, A.V. Barashev, J. Phys.: Condens. Matter **16**, S2629 (2004).
111. Y. Mishin, M.J. Mehl, D.A. Papaconstantopoulos, A.F. Voter, J.D. Kress, Phys. Rev. B **63**, 224106 (2001).
112. M.I. Mendelev, G.J. Ackland, Philos. Mag. Lett. **87**, 349 (2007).

113. P. Olsson, J. Wallenius, C. Domain, K. Nordlund, L. Malerba, Phys. Rev. B **72**, 214119 (2005).
114. G. Bonny, R.C. Pasianot, D. Terentyev, L. Malerba, Philos. Mag. **91**, 1724 (2011).
115. G. Bonny, R.C. Pasianot, L. Malerba, Model. Simul. Mater. Sci. Eng. **17**, 025010 (2009).
116. G. Bonny, R.C. Pasianot, N. Castin, L. Malerba, Philos. Mag. **89**, 3531 (2009).
117. G. Bonny, D. Terentyev, A. Bakaev, E.E. Zhurkin, M. Hou, D. Van Neck, L. Malerba, J. Nucl. Mater. **442**, 282 (2013).
118. G. Bonny, A. Bakaev, D. Terentyev, Yu.A. Mastrikov, J. Appl. Phys. **121**, 165107 (2017).
119. J.F. Ziegler, U. Littmark, J.P. Biersack, *The Stopping and Range of Ions in Solids* (Pergamon, 1985).
120. C. Bjorkas, K. Nordlund, Nucl. Instrum. Methods Phys. Res. B **259**, 853 (2007).
121. D. Terentyev, A. Zinovev, G. Bonny, J. Nucl. Mater. **475**, 132 (2016).
122. A.E. Sand, S.L. Dudarev, K. Nordlund, EPL **103**, 46003 (2013).
123. K. Nordlund, Comput. Mater. Sci. **3**, 448 (1995).
124. R.E. Voskoboinikov, Y.N. Osetsky, D.J. Bacon, J. Nucl. Mater. **377**, 385 (2008).
125. F. Gao, D.J. Bacon, A.V. Barashev, H.L. Heinisch, MRS Proc. **540**, 703 (1998).
126. S.I. Golubov, A.V. Barashev, R.E. Stoller, Compreh. Nucl. Mater. **1**, 357 (2012).
127. C.H. Woo, B.N. Singh, Philos. Mag. A **65**, 889 (1992).
128. B.D. Wirth, G.R. Odette, D. Maroudas, G.E. Lucas, J. Nucl. Mater. **244**, 185 (1997).
129. K. Vörtler, C. Björkas, D. Terentyev, L. Malerba, K. Nordlund, J. Nucl. Mater. **382**, 24 (2008).
130. M. Tikhonchev, V. Svetukhin, E. Gaganidze, J. Nucl. Mater. **442**, S618 (2013).
131. T. Toyama, A. Kuramoto, Y. Nagai, K. Inoue, Y. Nozawa, Y. Shimizu, Y. Matsukawa, M. Hasegawa, M. Valo, J. Nucl. Mater. **449**, 207 (2014).
132. G. Bonny, D. Terentyev, E.E. Zhurkin, L. Malerba, J. Nucl. Mater. **452**, 486 (2014).
133. D. Terentyev, X. He, G. Bonny, A. Bakaev, E. Zhurkin, L. Malerba, J. Nucl. Mater. **457**, 173 (2015).
134. P. Jung, J. Nucl. Mater. **117**, 70 (1983).
135. P. Jung, *Production of atomic defects in metals*, in *Landolt-Boernstein, Croup III: Crystal and Solid State Physics* (Springer-Verlag, Berlin, 1991).
136. C.H.M. Broeders, A.Yu. Konobeyev, J. Nucl. Mater. **328**, 197 (2004).
137. A.Yu. Konobeyev, U. Fischer, C.H.M. Broeders, L. Zanini, *Improved displacement cross-sections for structural materials irradiated with intermediate and high energy protons*, in *Proceedings of AccApp'07, Pocatello, Idaho* (2007).
138. A.Yu. Konobeyev, U. Fischer, L. Zanini, *Advanced evaluations of displacement and gas production cross-sections for chromium, iron, and nickel up to 3*GeV *incident particle energy*, in *Proceedings of AccApp'11, Knoxville* (2011).
139. A.Yu. Konobeyev, U. Fischer, S.P. Simakov, Nucl. Instrum. Methods Phys. Res. B **431**, 55 (2018).
140. R.E. Stoller, J. Nucl. Mater. **276**, 22 (2000).
141. A. Dunlop, D. Lesueur, P. Legrand, H. Dammak, J. Dural, Nucl. Instrum. Methods Phys. Res. B **90**, 330 (1994).
142. A.Yu. Konobeyev, U. Fischer, S.P. Simakov, Nucl. Eng. Technol. **51**, 170 (2019).
143. A.Yu. Konobeyev, U. Fischer, L. Zanini, *Neutron displacement cross-sections for materials from Be to U calculated using the arc-dpa concept*, in *Proceedings of AccApp'17, Quebec* (2017).
144. A.Yu. Konobeyev, U. Fischer, P.E. Pereslavtsev, S.P. Simakov, S. Akca, *DXS files*, `https://www-nds.iaea.org/public/download-endf/DXS/` (2017).
145. Mark T. Robinson, Phys. Rev. B **40**, 10717 (1989).
146. F. Mota, C.J. Ortiz, R. Vila, N. Casal, A. García, A. Ibarra, J. Nucl. Mater. **442**, S699 (2013).
147. F. Mota, R. Vila, C. Ortiz, A. Garcia, N. Casal, A. Ibarra, D. Rapisarda, V. Queral, Fus. Eng. Des. **86**, 2425 (2011) *Proceedings of the 26th Symposium of Fusion Technology (SOFT-26).*
148. P.V. Vladimirov, Yu.D. Lizunov, Radiat. Effects Defects Solids **139**, 109 (1996).
149. Pavel Vladimirov, Serge Bouffard, C. R. Phys. **9**, 303 (2008).
150. *MCNP5 Monte Carlo N-particle code developed by Los Alamos National Laboratory* (2015) `https://laws.lanl.gov/vhosts/mcnp.lanl.gov/mcnp5.shtml`.
151. *FENDL 3.1b: Fusion evaluated nuclear data library v 3.1b, released on 1 july 2016* (2016) `https://www-nds.iaea.org/fendl/`.
152. *LAMMPS Molecular Dynamics Simulator* (2015) `http://lammps.sandia.gov/`.
153. *HECToR: UK National Supercomputing Service* (2018) `http://www.hector.ac.uk`.
154. *MARCONI Eurofusion HPC* (2018) `http://www.hpc.cineca.it/hardware/marconi`.
155. J. Knaster, the IFMIF/EVEDA Integrated Project Team, Nucl. Fus. **57**, 102016 (2017).
156. F. Mota, Á. Ibarra, Á. García, J. Molla, Nucl. Fus. **55**, 123024 (2015).
157. A. Ibarra, R. Heidinger, P. Barabaschi, F. Mota, A. Mosnier, P. Cara, F.S. Nitti, Fusion Sci. Technol. **66**, 252 (2014).
158. F. Arbeiter, A. Abou-Sena, Y. Chen, B. Dolensky, T. Heupel, C. Klein, N. Scheel, G. Schlindwein, Fusion Eng. Des. **86**, 607 (2011) *Proceedings of the 26th Symposium of Fusion Technology (SOFT-26).*
159. Iole Palermo, Iván Fernández, David Rapisarda, Angel Ibarra, Fus. Eng. Des. **109-111**, 13 (2016) *Proceedings of the 12th International Symposium on Fusion Nuclear Technology-12 (ISFNT-12).*
160. Iván Fernández-Berceruelo, David Rapisarda, Iole Palermo, Luis Maqueda, David Alonso, Tomas Melichar, Otakar Frýbort, Ladislav Vála, Ángel Ibarra, Fus. Eng. Des. **124**, 822 (2017) *Proceedings of the 29th Symposium on Fusion Technology (SOFT-29) Prague, Czech Republic, September 5-9, 2016.*
161. F. Moro, A. Del Nevo, D. Flammini, E. Martelli, R. Mozzillo, S. Noce, R. Villari, Fus. Eng. Des. **136**, 1260 (2018).
162. P. Lu, P. Pereslavtsev, F. Hernandez, U. Fischer, Fus. Eng. Des. **125**, 18 (2017).

163. P. Pereslavtsev, U. Fischer, F. Hernandez, L. Lu, Fus. Eng. Des. **124**, 910 (2017) *Proceedings of the 29th Symposium on Fusion Technology (SOFT-29) Prague, Czech Republic, September 5-9, 2016.*
164. E. Sikik, *BR2 spectrum*, private communication (2015) BR2/RCE/ES/2015/10 BR2 Neutron Spectra Position: hote plane.
165. V.D. Sevastianov *et al.*, *Kharakteristiki polei neitronov, Handbook Mendeleevo, VNIIFTRI* (2014) `http://www.gsssd-rosatom.mephi.ru/DB-nspectra/fission/550/598.php`.
166. L.R. Greenwood, *Neutron source characterization for fusion materials studies, position of the neutron spectrum: near core center* (1981) Second Topical Meeting on Fusion Reactor, CONF-810831–101.
167. I. Remec, F. Kam, *Position of the neutron spectra: Channel 5, midplane* (1997) NUREG/CR-6453 ORNL/TM-13204.
168. G.R. Odette, P.J. Maziasz, J.A. Spitznagel, J. Nucl. Mater. **104**, 1289 (1981).
169. M.E. Sawan, Fus. Eng. Des. **87**, 551 (2012) *Tenth International Symposium on Fusion Nuclear Technology (ISFNT-10).*